TECHNISCHE UNIVERSITÄT MÜNCHEN

Fakultät Wissenschaftszentrum Weihenstephan für Ernährung, Landnutzung und Umwelt

Professur für Ökoklimatologie

Tracing atmospheric carbon dioxide: pollution sources and air-mass transport influencing high Alpine areas in Central Europe

Homa Ghasemifard

Vollständiger Abdruck der von der Fakultät Wissenshaftszentrum Weihenstephan für Ernährung, Landnutzung und Umwelt der Technischen Universität München zur Erlangung des akademischen Grades eines

Doktors der Naturwissenschaften (Dr. rer. nat.)

genehmigten Dissertation.

Vorsitzende:

Prof. Dr. Anja Rammig

Prüfer der Dissertation:

1. Prof. Dr. Annette Menzel
2. Prof. Dr.-Ing. Jia Chen

Die Dissertation wurde am 27.01.2020 bei der Technischen Universität München eingereicht und durch die Fakultät Wissenschaftszentrum Weihenstephan für Ernährung, Landnutzung und Umwelt am 08.06.2020 angenommen.

In loving memory of my father Habib

Acknowledgements

I would like to express my sincere gratitude to my supervisor Prof. Dr. Annette Menzel for the continuous support of my Ph.D. study, for her motivation and immense knowledge. Her guidance helped me in all the time of research and writing of this dissertation. I would like to thank my second supervisor, Dr. Jia Chen, for her trust. When I was lost in this journey, she suddenly became a light that brightened my way and motivated me not to give up and to continue. I could not have imagined having better advisors for my Ph.D. study.

I would like to thank the following people for helping me with this project: Dr. Rehm, Mr. Couret, and UFS staff for being my support in the laboratories at Schneefernerhaus when devices refused to follow my orders; Dr. Hachinger, for helping me kindly on running big calculations at LRZ supercomputer; Dr. Ries, the kindest man in this journey that always encourage my soul; Dr. Schunk, my first officemate, for his kind heart and always having my back and helping me in many ways; Dr. Wofsy and Dr. Vogel enlightening me during a hard time of dealing with data.

I would like to thank my fellow doctoral students for working together in a great environment and for friendship and all the fun we have had in the last six years, especially to Ye Yuan who never said no to my question "do you have time?" without him I could not make it. And to my brother Wael Ghada, when I was scared of going through the writing process but he was there to motivate me. I would particularly like to thank the talented artist in our group Alissa Luepke for kindly drawing the carbon cycle figure.

I am grateful to my best friends, Bita, Nassim, Siavash, Basel, Alireza, Zahra, Hadi, and Anna, who have provided me with moral and emotional support along the way.

Last but not the least, I would like to thank my family: my mamani Akram, my brother Mohamadreza and sisters Hadis and Hale, my brother-in-law Alireza that always believed in me and wanted the best for me, and my sweetest niece Vianna who has brought remarkable love and happiness to my life. Mamani, you were the greatest motivation in this journey, you prayed for me and encouraged me to stay strong. I would also like to express my gratitude to my in-laws for their support and encouragement.

Finally, and above all, I cannot begin to express my unfailing gratitude and love to my husband, Ali who was next to me from the moment I applied for this Ph.D. position and has supported me throughout this process and has constantly encouraged me when the tasks seemed arduous and insurmountable.

Abstract

Anthropogenic emissions of greenhouse gases are the main cause of the increase in global mean temperature (IPCC, 2014). In the context of climate change, an improved quantitative understanding of the geographical distribution of sources and sinks of atmospheric greenhouse gas carbon dioxide (CO_2) is greatly needed. The Global Atmospheric Watch (GAW) Programme monitors the atmospheric mixing ratios of CO_2 over the globe at different stations. Their measured data sets are therefore compatible and thus can be used to obtain regional estimates of total carbon fluxes. This dissertation not only adds additional measurement series to the existing measurement network of atmospheric CO_2 but, for the first time, presents the stable carbon isotope composition ($\delta^{13}C$) recorded at the GAW Global station Environmental Research Station Schneefernerhaus (UFS, 2650 m a.s.l.) in Germany. Due to the site elevation and being far away from immediate sources and sinks, measurements are representative of larger spatial areas. However, UFS can occasionally be affected by large variations of local or regional anthropogenic emissions if air masses of the planetary boundary layer are lifted and mixed with the free troposphere via processes, such as foehn flows, which can significantly disturb the interpretation of measurements. Therefore, the aim of this Ph.D. work is first to detect when UFS has been influenced by pollution events and later to characterize potential sources.

The atmospheric CO_2 and its $\delta^{13}C$ were continuously measured for a two-and-a-half-year period. The measurements were performed with a cavity ring-down spectrometer (Picarro G1101-i), which was not upgraded to account for spectral interferences caused by methane (CH_4) and water vapor. The recalculation of $\delta^{13}C$ and correction of CO_2 were performed using parallel measurements of CO_2, CH_4, and water vapor. Thereafter, pollution events were detected and investigated quantitatively using the Keeling plot method, ratios of atmospheric measurements [e.g. carbon monoxide (CO) versus CO_2; CH_4 versus CO_2], and atmospheric backward trajectory model (i.e., HYSPLIT).

In order to detect pollution events via continuous measurements of CO_2 and $\delta^{13}C$, the moving Keeling plot method based on the UFS specifications were adopted and detected 14 pollution events in the period may 2012 to November 2014. Seven events were presented in a publication and one event in this dissertation. The Keeling method showed that sources of pollution events were either coal or wood combustion which potentially originated from domestic heating or contributions from natural gas and gasoline. The latter results together with CO/CO_2 and CH_4/CO_2 emission ratios suggested that the anthropogenic emissions can be related to road transport and traffic. Based on the trajectory model and the Potential Source Contribution Function, it could be shown that the source regions with elevated CO_2 concentrations during pollution

events as well as the entire measurement period were located in West and East Germany, where coal mining and heavy industry are present.

Zusammenfassung

Anthropogene Treibhausgasemissionen sind die Hauptursache für den Anstieg der globalen Durchschnittstemperatur (IPCC, 2014). Im Zusammenhang mit dem Klimawandel ist ein verbessertes quantitatives Verständnis der geografischen Verteilung der Quellen und der Senken des atmosphärischen Treibhausgases Kohlendioxid (CO_2) dringend erforderlich. Das Global Atmospheric Watch (GAW)-Programm überwacht die weltweite CO_2-Konzentration an verschiedenen Stationen. Diese Messdaten sind untereinander kompatibel und können daher zur regionalen Abschätzung der Gesamtkohlenstoffflüsse verwendet werden. Diese Dissertation erweitert nicht nur das bestehende Netz an Beobachtungsstationen des atmosphärischen CO_2 um zusätzliche Messreihen, sondern präsentiert erstmals das an der deutschen GAW Beobachtungsstation Umweltforschungsstation Schneefernerhaus (UFS, 2650 m ü. NN) aufgezeichnete stabile Kohlenstoffisotop ($\delta^{13}C$). Aufgrund der Höhenlage der UFS und seiner Entfernung zu unmittelbaren CO_2-Quellen und -Senken sind die Messungen meist für größere Gebiete repräsentativ. Die UFS wird jedoch weiterhin durch große Schwankungen der lokalen oder regionalen anthropogenen Emissionen beeinflusst, wenn Luftmassen der planetaren Grenzschicht angehoben und über Prozesse, wie sie z.B. bei Föhn vorkommen können, mit der freien Troposphäre vermischt werden, was die Interpretation der Messungen erheblich erschweren kann. Ziel dieser Doktorarbeit ist es daher, zunächst festzustellen, wann die UFS durch Schadstoffereignisse beeinflusst wurde und anschließend potenzielle Quellen (und ihre Herkunftsregionen) zu charakterisieren.

Das atmosphärische CO_2 und sein $\delta^{13}C$ wurden über einen Zeitraum von zweieinhalb Jahren kontinuierlich gemessen. Für die Messung wurde ein Hohlraumresonanz-Spektrometer (cavity ring-down spectrometer, Picarro G1101-i) verwendet, das nicht für spektrale Interferenzen durch Methan (CH_4) und Wasserdampf nachgerüstet wurde. Die Neuberechnung von $\delta^{13}C$ und die Korrektur von CO_2 wurden deshalb mittels parallelen Messungen von CO_2, CH_4 und Wasserdampf durchgeführt. Anschließend wurden Schadstoffereignisse erfasst und quantitativ mit dem Keeling-Plot-Verfahren, Verhältnissen von atmosphärischen Messungen [z. B. Kohlenmonoxid (CO) zu CO_2; CH_4 zu CO_2] und atmosphärischen Rückwärtstrajektorien (d.h. HYSPLIT) untersucht.

Um die Schadstoffereignisse in den kontinuierlichen Messungen von CO_2 und $\delta^{13}C$ zu identifizieren, wurde das Keeling-Plot-Verfahren basierend auf den Spezifikationen der UFS angewendet, es erkannte 14 Schadstoffereignisse. Sieben dieser Ereignisse wurden in einer Publikation und ein Ereignis in dieser Dissertation vorgestellt. Das Keeling-Verfahren zeigte, dass die Quellen der Schadstoffereignisse entweder von Kohle- oder Holzverfeuerung, wahrscheinlich aus Haushaltsheizungen oder zum Teil von Erdgas- und Benzinverbrennungen stammen. Letztere Ergebnisse zusammen mit den CO/CO_2-

und CH_4/CO_2-Emissionsverhältnissen lassen darauf schließen, dass die anthropogenen Emissionen mit dem Straßentransport und dem Verkehr zusammenhängen können. Auf der Basis von Rückwärtstrajektorien und der Potential Source Contribution Function konnte gezeigt werden, dass die Quellenregionen für Episoden mit erhöhten CO_2-Konzentrationen während der gesamten Messdauer in West- und Ostdeutschland liegen, in denen sich Kohlebergbau und Schwerindustrie befinden.

Contents

1 Introduction

Humans have been burning coal, oil, and gas for 250 years. The exploitation of fossil fuels has led to economic growth and technological progress (e.g., industrial revolution), while causing threatening changes to the climate system. When burning fossil fuels, the most important (in terms of contribution to the greenhouse effect) anthropogenic long-lived greenhouse gas, carbon dioxide (CO_2), is released into the atmosphere, and the emissions have been increasing exponentially over the last centuries. In a very short time span in Earth's history, humans have increased the CO_2 concentration in the atmosphere by around 46% and it accounted for approximately 81% of the increase in radiative forcing from 1990 to 2017 (WMO, 2018). The consequence of past and ongoing emissions is an increase in the Earth's tropospeheric temperature by 1 °C (likely between 0.8 °C and 1.2 °C) above pre-industrial levels in 2017, rising by 0.2 °C (likely between 0.1 °C and 0.3 °C) per decade (IPCC, 2018). In the next 100 years, the atmospheric CO_2 concentration will likely double and the Earth will probably heat up by three to four degrees if humankind does not achieve neutrality in CO_2 and other heat-trapping gases (IPCC, 2014). The global effects such as rising sea levels and shifting vegetation zones have been observed, and if climate change continues at such unprecedented speed, it could lead to heavy economic losses, social upheaval, and migration of people across the world.

We are facing a global challenge and all countries, specially those with high past and current emissions, are responsible for reducing CO_2 emissions. In December 2015 in Paris, the twenty-first session of the Conference of the Parties (COP 21) at the UN climate change conference represented a breakthrough in international climate policy, where, 195 nations committed to protect the climate and to reduce emissions. The goal of the "Paris agreement" was to limit the rise in the global average temperature to well below 2°C above pre-industrial levels. Accordingly, the emission budget is limited to releasing less than half of the amount of CO_2 that has already been released into the atmosphere (United Framework Convention on Climate Change UNFCCC, 2015).

In December 2018, the Intergovernmental Panel on Climate Change (IPCC) published the "Special Report on Global Warming of 1.5 °C", showing that the difference between 1.5 °C and 2 °C is critical to the lives of millions of people and to ecosystems (IPCC, 2018). According to this report, the 1.5 °C scenario requires halving emissions by ~2030, net-zero by ~2050, and negative thereafter (Figure 1.1).

By assessing atmospheric CO_2 sources and sinks, this dissertation contributes to the present state of carbon research which requires a fundamental understanding of the global carbon cycle and atmospheric response to changes in elevated carbon concentration in reservoirs.
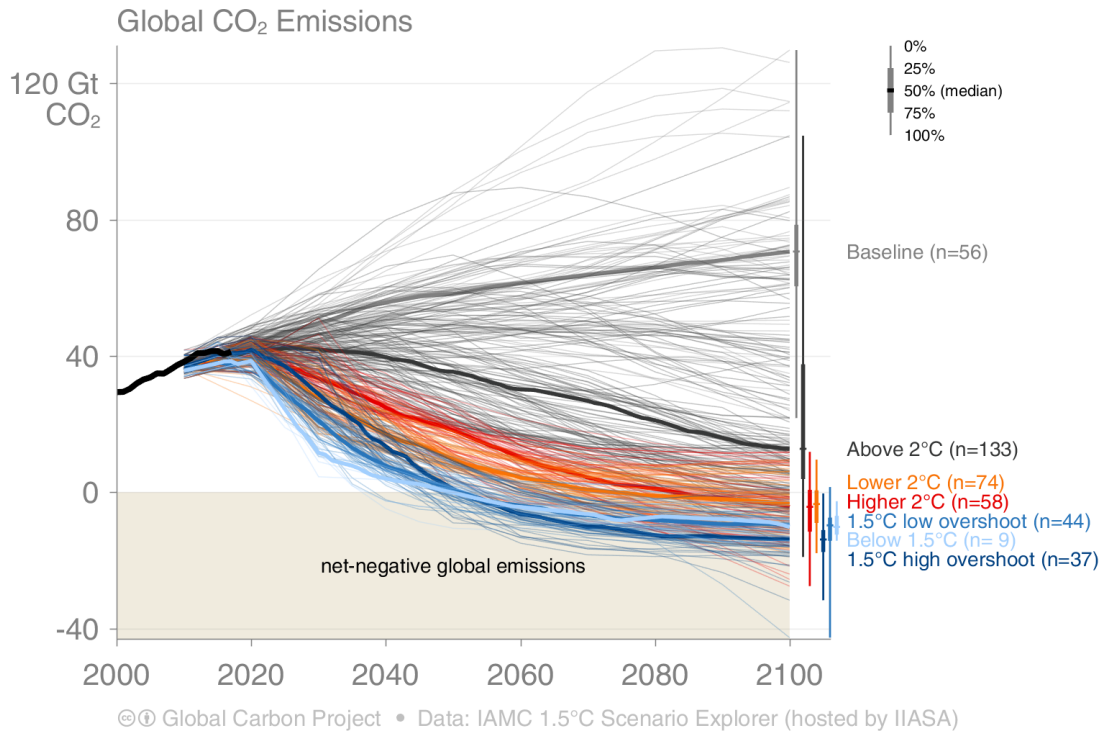
Global CO$_2$ Emissions

Figure 1.1: The IPCC "Special Report on Global Warming of 1.5 °C" presented new scenarios: 1.5 °C scenarios require halving emissions by ∼2030, net-zero by ∼2050, and negative thereafter [figure is taken from: Global Carbon Project/Carbon Budget `https://www.globalcarbonproject.org/carbonbudget/`; (Friedlingstein et al., 2019)].

1.1 Global Carbon Cycle

Throughout Earth's history, carbon has cycled naturally between the atmosphere, the hydrosphere (ocean), the terrestrial biosphere, and the lithosphere (sediments and rocks) and this continuous cycle regulates the amount of carbon dioxide in the atmosphere. Since our measurements range from hourly to several years, this section focused on exchange between atmosphere, terrestrial ecosystem, and fossil fuels. In equilibrium, the atmospheric GHG mixing ratios and the planetary boundary layer (PBL) height are constant and fluxes into and out of the atmosphere are in balance (Seinfeld and Pandis, 2016). However, CO$_2$ emissions of fossil fuels, as well as land-use change, disrupt this equilibrium.

The ocean is the largest carbon reservoir containing approximately 38000 gigatons of carbon (GtC = 10^{15} g of carbon) followed by the terrestrial biosphere with ∼2750 GtC out of which about 3/4 resides in soils and 1/4 is stored in the living biomass (see Figure 1.2) [numbers in this paragraph are based on the global carbon budget 2018 (Le Quéré et al., 2018)]. In comparison, the atmosphere is the smallest pool containing about
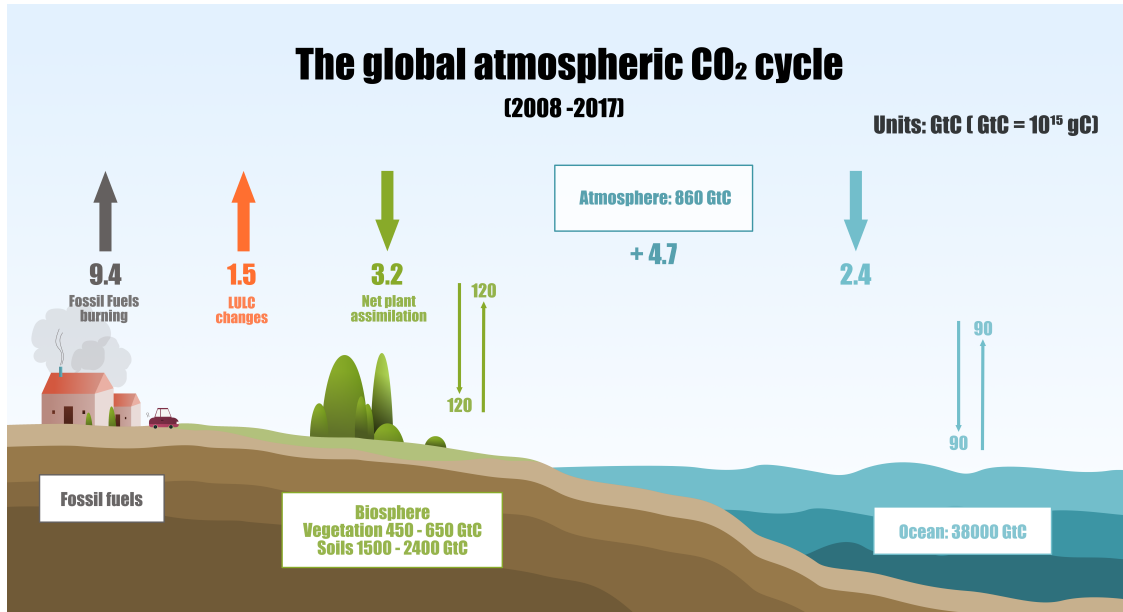
Figure 1.2: Schematic representation of the global carbon cycle averaged globally over the decade 2008–2017, showing the reservoirs (in GtC) and fluxes (GtC yr^{-1}). Flux and inventory numbers are taken from the global carbon budget 2018 (Le Quéré et al., 2018).

860 GtC in present times. Though being the smallest pool, the atmosphere acts as a link between other carbon reservoirs and plays the most important role, especially in the context of climate change. Each year approximately 90 GtC is exchanged between the atmosphere and the ocean, and another 120 GtC between the atmosphere and the terrestrial ecosystem (photosynthesis and respiration). In the last decade, the annual fossil fuels burned amount to about 9.4 ± 0.5 GtC yr^{-1} (uncertainties are reported as $\pm 1\sigma$) and about 1.5 ± 0.7 GtC yr^{-1} due to land use and land cover change (LULC). Approximately half of this amount (4.7 ± 0.02 GtC yr^{-1}) contributes to an increase in atmospheric CO_2 and the other half, 3.2 ± 0.8 GtC yr^{-1} and 2.4 ± 0.5 GtC yr^{-1}, is sequestered in the oceans and the terrestrial system, respectively. However, the imperfect data, errors in each estimate, and not included small terms result in a carbon budget imbalance of 0.5 GtC yr^{-1}. Hence, if the components of the CO_2 budget are (1) the CO_2 emissions from fossil fuel combustion (E_{FF}; GtC yr^{-1}), (2) the CO_2 emissions resulting from human activities leading to land-use change (E_{LULC}; GtC yr^{-1}), (3) the growth rate of atmospheric CO_2 (G_{ATM}; GtC yr^{-1}), the uptake of CO_2 by (4) ocean (S_{OCEAN}; GtC yr^{-1}) and (5) terrestrial biosphere (S_{BIO}; GtC yr^{-1}), and budget imbalance (B_{IM}), the global emissions and their partitioning among the atmosphere, ocean, and land are:

$$E_{FF} + E_{LULC} = G_{ATM} + S_{OCEAN} + S_{BIO} + B_{IM} \qquad (1.1)$$

1.2 Atmospheric variability of carbon dioxide

Most of the carbon in the atmosphere is in the form of CO_2 together with small amounts of carbon monoxide (CO), methane (CH_4) and other hydrocarbons [e.g. ethane (C_2H_6), butane (C_4H_{10}), and propane (C_3H_8)].

Charles David Keeling from the Scripps Institution of Oceanography initiated long-term observations of the atmospheric CO_2 mixing ratios at the Mauna Loa observatory in Hawaii at 19°N in 1958 (Keeling, 1983). The daily record has continued to the present day, almost without any interruptions (Figure 1.3). The CO_2 mixing ratio has reached an average of 408.52 $\pm$ 0.12 parts per million (ppm) in 2018 with a growth rate of 2.86 $\pm$ 0.11 ppm yr^{-1} (Tans and Keeling, 2019). The increase in CO_2 is unequivocally caused by the consumption of fossil fuels in transportation, building heating and cooling, manufacturing of cement as well as land-use changes, i.e., deforestation (Houghton, 2003) and biomass burning (Andreae and Merlet, 2001).

Atmospheric CO_2 concentrations exhibit not only an increasing trend, but also a clear seasonal pattern in the monthly averages. This discovery, now known as the Keeling curve, was reported by Keeling two years after starting the measurements (Keeling, 1960). He observed that the CO_2 levels drop during spring and summer when plants consume atmospheric CO_2 for growth and reproduction (photosynthesis) and rise in autumn and winter when plants and leaves die off, the dominant process being the exhalation of CO_2 into the atmosphere due to the decomposition (respiration). Soon after, researchers began to measure CO_2 levels at many sites at a variety of latitudes in both hemispheres (Nakazawa et al., 1997; Conway et al., 1994). They confirmed the long-term upward trend and provided sufficient information to explain the alteration between seasonal variations in different sites through latitudinal variations. As the cycle is primarily regulated by the seasonal uptake and release of CO_2 by the terrestrial ecosystem, regions with more plants experience larger fluctuations (e.g. boreal forest zone, 55°N to 65°N) than those with fewer plants (e.g. the South Pole, where there is hardly any seasonal variability) (Forster et al., 2007).

Much of what is known about the carbon cycle has been obtained through global atmospheric and isotopic ratio measurements. More specifically, the stable isotopes play an important role in understanding the ways in which ecosystems respond to climatic conditions. The ratio of carbon-13 to carbon-12 ($^{13}C/^{12}C$) isotopes can be used, given the right condition, as a tracer to distinguish between the biospheric, oceanic, and anthropogenic contributions to atmospheric CO_2 mixing ratios (Eq. 1.1).

1.3 The isotopologues of CO_2

Carbon dioxide naturally consists of more than just one isotopologue since different isotopes exist in nature, e.g. $^{12}C(CO_2)$ ($=^{12}C^{16}O^{16}O$) , $^{13}C(CO_2)$ ($=^{13}C^{16}O^{16}O$) and $^{18}O(CO_2)$ ($=^{12}C^{18}O^{16}O$). The stable isotope ^{12}C contains six neutrons and six protons and 98.4% of all CO_2 isotopologues are $^{12}C(CO_2)$. The stable isotope ^{13}C with an
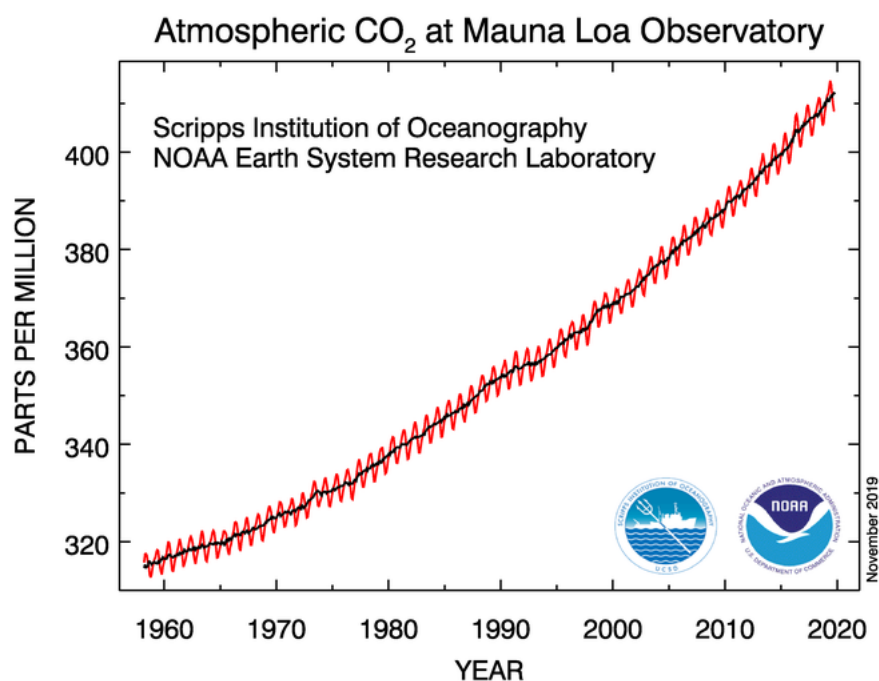
Atmospheric CO_2 at Mauna Loa Observatory

Figure 1.3: The monthly mean atmospheric CO_2 mixing ratio (red curve) expressed as parts per million and the long-term trend (black curve) at the Mauna Loa observatory, Hawaii, United States. The oldest and longest record of direct measured CO_2. A pronounced seasonal cycle is also evident at Mauna Loa, with a maximum in winter and minimum in summer [figure is taken from: NOAA/ESRL `https://www.esrl.noaa.gov/gmd/` and updated every month].

additional neutron constitutes almost 1.1% of all isotopologues CO_2 [$^{13}C(CO_2)$]. A small fraction of natural carbon exists as the radioactive isotope ^{14}C with a half-life of 5715 years and 10^{-10}% of CO_2 isotopologues are $^{14}C(CO_2)$ (Greenwood and Earnshaw, 2016). Different masses of isotopologues cause fractionation, thus the ratio of the isotopologues is dependent on the underlying chemical and physical processes. In the following, the focus will be on stable isotope ratio $^{13}C/^{12}C$. The deviation of the ratio of ^{13}C to ^{12}C isotopes from a calibration standard [Vienna Pee Dee Belemnite carbonate (VPDB)] is customarily stated by notation $\delta^{13}C$, defined as

$$\delta^{13}C = [\frac{(^{13}C/^{12}C)_{\text{sample}}}{(^{13}C/^{12}C)_{\text{standard}}} - 1] * 1000 \tag{1.2}$$

Variations in isotopic ratios are in the parts per thousand range and, thus, are reported as permil variations (‰).

1.4 Isotopic fractionations in CO_2 reservoirs

Chemical properties of all isotopes of an element are identical since their electronic structures are the same. Nevertheless, small differences in chemical behavior occur due to the frequencies of atomic and molecular vibrations which can be described by quantum theory. The energy of a molecule consists of several components: translational, rotational, vibrational, electronic, and nuclear spin. The last two components play no role in isotopic fractionations and are negligible. Among the first three lead to differences in chemical behavior, vibration is the most important in isotopic fractionation. Quantum theory allows only discrete energy to be occupied and these permissible energy levels depend on mass, thereby suggesting that the energy will be different for different isotopes. The vibrational energy level of a bond involving heavier isotopes will be stronger than that of lighter isotopes which are more readily broken and participate in a given chemical reaction. The above fractionation is a result of equilibrium effects. However, isotope fractionation can also originate from kinetic effects that are associated with fast processes, such as evaporation and diffusion.

Terrestrial biosphere

Photosynthesis of terrestrial biomass is the most important process in contributing to isotopic fractionation. Photosynthetic fractionation of carbon isotopes involves several steps and is primarily kinetic. CO_2 diffuses through plant's stomata and the average $\delta^{13}C$ is correlated with stomatal conductance (Park and Epstein, 1960) which discriminates against the heavier ^{13}C by 4.4‰ (Farquhar et al., 1989). After diffusion, there is a divergence in the chemical pathways. Most species ($\sim$95% of all plant biomass) including trees and some of the major crops such as rice and barley use an enzyme called ribulose bisphosphate carboxylase oxygenase (RuBisCO) to catalyze a reaction. In this carboxylation reaction called the Calvin cycle, ribulose bisphosphate reacts with one molecule of CO_2 to produce two molecules of 3-phosphoglyceric acid, a compound containing three carbon atoms. This reaction contributes to an isotopic fractionation of 27‰ (Farquhar et al., 1989). Such plants are called C3 plants and the overall isotopic fractionation ranges between -20 to -37‰ (Kohn, 2010). The other photosynthetic pathway is the Hatch-Slack cycle of C4 plants comprising grasses in the tropical latitudes, as well as crops at the mid-latitudes such as maize and sugarcane. C4 plants use phosphoenol pyruvate carboxylase (PEP) to initially fix the carbon and form oxaloacetate, in which a much smaller fractionation of about 2 to 2.5‰ occurs, consequently the overall $\delta^{13}C$ value in C4 plants is -12 to -16‰ (Cerling et al., 1998). The plants using the Crassulacean Acid Metabolism are known as CAM plants and generally use the C4 pathway but can use the C3 pathway under certain conditions. The $\delta^{13}C$ value of CAM plant is between those of C3 and C4 plants (O'Leary, 1988). Respiration contributes only weakly to isotopic fractionation and therefore respiratory fluxes have a similar photosynthetic signal to the plants (Ghashghaie and Badeck, 2014).

Oceans

In the atmospheric-ocean system, most of the CO$_2$ is dissolved in the oceans (>98%) and the diffusion of CO$_2$ across the atmosphere-ocean interface fractionates the ^{13}C/^{12}C ratio to about 1/10 of the degree of terrestrial photosynthesis ~1‰) (Mook, 2000; Mook et al., 1974).

Fossil fuels

The ^{13}C signature of CO$_2$ emissions of fossil fuels has also characterized depleted ^{13}C since fossil fuels are originally derived from plants. The isotopic signatures depend on the ^{13}C signature of the fuel type, the origin, and the formation conditions of the fuel. The typical δ^{13}C signature for different combustions is -27 to -24‰ for coal, -44 to -37‰ for natural gas, and -32 to -26‰ for gasoline (Pataki et al., 2007). As a consequence of the increasing anthropogenic flux of fossil fuel CO$_2$ into the atmosphere, the ^{13}C content of atmospheric CO$_2$ has decreased over time.
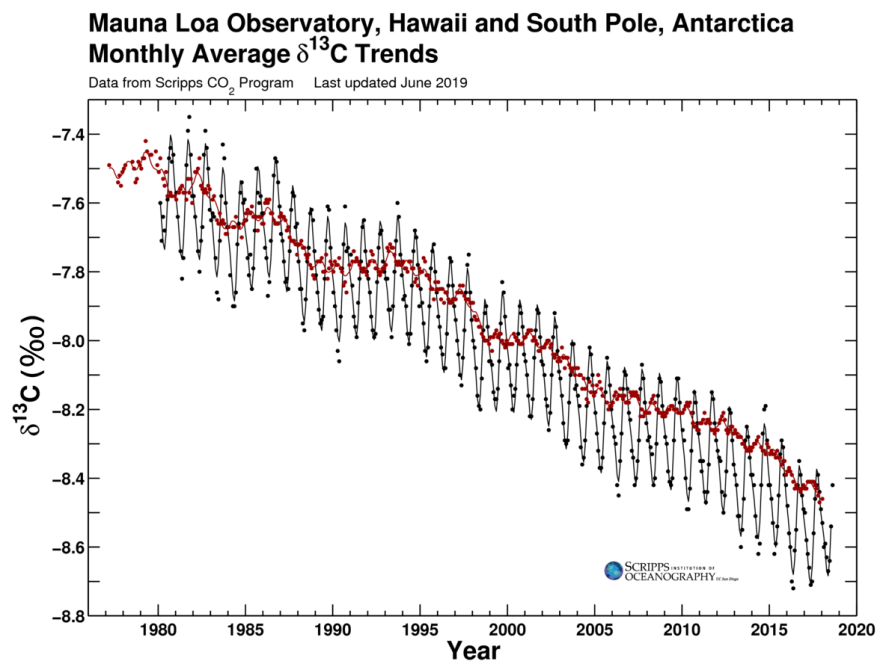

Figure 1.4: Monthly average atmospheric stable carbon isotope composition of CO$_2$ (δ^{13}C) at Mauna Loa (black dots) and at South Pole (red dots) [figure is taken from: Scripps CO$_2$ Program `https://scrippsco2.ucsd.edu/` and updated every month].

Atmosphere

Figure 1.4 illustrates the relative proportion of ^{13}C in the atmosphere, showing a negative correlation with the increase of the atmospheric CO$_2$ concentration (see Figure 1.3). Before the industrial revolution, atmospheric δ^{13}C was about -6.5‰; today

the value is around -8.5‰. δ^{13}C at Mauna Loa has decreased by 0.03‰ yr^{-1} over 16 years from 1994 to 2009 [data source: (GLOBALVIEW-CO2C13, 2009)]. The seasonal cycle of δ^{13}C shows a pattern opposite to that of CO_2. More specifically, δ^{13}C increases in summer and decreases in winter. This opposite seasonal variation can be explained using the same justification as with the CO_2 pattern [i.e., photosynthesis and respiration (Ghashghaie and Badeck, 2014)].

The atmospheric ^{13}C/^{12}C isotope ratio changes during the exchange of CO_2 between reservoirs. Accordingly, the relative proportion of the atmospheric isotopes can alter depending on what CO_2 source or sink has been emitting into or sequestering from the atmosphere. This information can be used to separate individual CO_2 flux components in order to understand ecosystem behavior in response to climatic conditions (Ciais et al., 2005). Neglecting the imbalance budget, the isotopic mass balance can be derived similarly to atmospheric CO_2 mass balance (Eq.1.1),

$$\delta_{FF}E_{FF} + \delta_{LULC}E_{LULC} = \delta_{ATM}G_{ATM} + \delta_{OCEAN}S_{OCEAN} + \delta_{BIO}S_{BIO} \qquad (1.3)$$

where δ represents δ^{13}C of each CO_2 component. This equation together with Eq. 1.1 are used as principles of the Keeling plot (Keeling, 1958, 1960), a very well-known method to distinguish between global carbon fluxes, e.g. terrestrial biosphere and oceans (Ciais et al., 1995a; Mook et al., 1983; Miller and Tans, 2003; Alden et al., 2010) or identifying signatures of fuel types (Pataki et al., 2003; Newman et al., 2015).

2 Aims and outlines

In order to assess atmospheric CO_2 sources and sinks, its concentration is continuously monitored with high temporal resolution. The Global Atmospheric Watch (GAW) programme of the World Meteorological Organization (WMO) is a worldwide network focusing on the role of atmospheric chemistry in global change. GAW includes global and regional measurement sites, especially several high-alpine observatories, such as Mount Cimone, Italy (Ciattaglia, 1983), Sonnblick, Austria (Kaiser et al., 2007), Jungfraujoch (JFJ), Switzerland (Sturm et al., 2005), and Zugspitze, Germany (Yuan et al., 2018). These continental mountain stations located at high elevations are far from immediate sources, thus, record the background atmospheric levels and sample well-mixed air masses of the free troposphere. Nevertheless, high mountain sites can be influenced by local and regional anthropogenic emissions on time scales of hours and days, when air masses of the planetary boundary layer are lifted and mixed with free troposphere air masses via meteorological processes (i.e., thermally induced flow systems and foehn flows). This issue at alpine mountain sites has been addressed in several studies using in-situ measurements as well as statistical trajectory models: Apadula (2003) showed that a short-lived episode of increase in CO_2 concentration was recorded at three sites (Plateau Rosa and Monte Cimone in Italy, and Zugspitze in Germany) with a delay of 12 to 18 hours using backward trajectory and cluster analysis; Uglietti et al. (2011) investigated the transport of CO_2 and O_2 towards JFJ when the CO_2 mixing ratio was the highest using the backward Lagrangian Particle Dispersion Model (LPDM) simulations; Tuzson et al. (2011) characterized four pollution events recorded at JFJ when high concentrations of CO_2 and CO, and depleted $\delta^{13}C(CO_2)$ were recorded; Ferrarese et al. (2015) investigated two high CO_2 concentration events at four high-altitude European stations using backward trajectories.

This dissertation assesses 2.5-year measurements of atmospheric CO_2 and $\delta^{13}C$ recorded at the Environmental Research Station Schneefernerhaus (UFS), Zugspitze, Germany. This work identified and investigated events with high CO_2 concentration and characterized anthropogenic sources. Measured data were analyzed both quantitatively, to determine the source signatures of pollution events, and with model data to detect the potential source origins. It is the first time that continuous atmospheric $\delta^{13}C$ has been recorded at this site and presented in a study, thus, the values obtained are characteristic for the region, and can be incorporated into the emission inventories.

In order to achieve these objectives, in the first paper (Sect. 4.1), "Atmospheric CO_2 and $\delta^{13}C$ Measurements from 2012 to 2014 at the Environmental Research Station Schneefernerhaus, Germany: Technical Corrections, Temporal Variations and Trajectory Clustering" (Ghasemifard et al., 2019a), the data were evaluated through comprehensive

tests in which specific corrections and selections were described and implemented. Seasonal and diurnal variabilities of δ^{13}C together with the CO_2 mixing ratio were presented in detail and compared with similar measurements at JFJ. Backward trajectory together with air mass cluster analysis were used to identify the potential CO_2 sources and sinks in winter and summer, respectively.

In the second paper, (Sect. 4.2) "Pollution Events at the High-Altitude Mountain Site Zugspitze-Schneefernerhaus (2670 m a.s.l.), Germany" (Ghasemifard et al., 2019b), five months of the data were studied in more detail. Throughout this period, sudden and pronounced increases in the tropospheric CO_2 were closely correlated with variations in measured CH_4, CO mixing ratios and δ^{13}C. The high precision and resolution allowed the application of the Keeling plot method for source signature identification. For further investigation of CO_2 sources, CO and CH_4 mixing ratios were used as proxies for fossil fuel CO_2. The spatial origin of these CO_2 emission sources was then determined by backward trajectory analysis and potential source contribution functions.

The studies contribute to the following main questions:

1. How to detect pollution events at mountain site Schneefernerhaus?
2. How to characterize high atmospheric CO_2 pollution episodes at this site?
3. Where are the potential source and sink regions of CO_2?

3 Material and Methods

An overview of the methods used in the publications together with the measurement device description will be given here, starting with Cavity Ring-Down Spectroscopy (CRDS), characterizing anthropogenic CO_2 sources, backward trajectory, and software used. The CRDS part includes the principle of the CRDS technique (Sect. 3.1.1) and spectroscopic interferences (Sect. 3.1.2). The characterizing anthropogenic CO_2 sources introduces three methods in order to identify anthropogenic sources of the CO_2 mixing ratio including $\delta^{13}CO_2$ (Sect. 3.2.1), CO/CO_2 emission ratio (Sect. 3.2.2), and CH_4/CO_2 emission ratio (Sect. 3.2.3). The backward trajectory part cover information on the HYSPLIT model (Sect. 3.3.1), the Potential Source Contribution Function (Sect. 3.3.2), cluster analysis (Sect. 3.3.3), and platforms (Sect. 3.3.4). Finally, the software used for the previously introduced methods will be presented (Sect. 3.4).

3.1 Cavity Ring-Down Spectroscopy

In this study, the CO_2 mixing ratio and $\delta^{13}CO_2$ stable isotope abundance were measured using a Picarro G1101-i analyzer that employs cavity ring-down technology. Since the analyzer was not upgraded to account for two specific spectral interferences (methane and water vapor), comprehensive evaluation and validation were employed and described in the first paper. In this section, design flaws resulted in measurement malfunctions are explained in detail and for this purpose, the principle of the measurement device technology must be described as well.

3.1.1 Principle of CRDS technique

Cavity ring-down spectroscopy (CRDS), a direct optical absorption measurement technique, was first introduced in 1988 by O'Keefe and Deacon (1998). To understand the theory of CRDS, basic knowledge of absorption spectroscopy is required and presented below. The absorption of a sample gas is related to the attenuation of the light intensity which is expressed by the Beer Lambert's law of optical absorption

$$I(t, \lambda) = I_0 e^{-\alpha(\lambda)L} \tag{3.1}$$

where I_0 and I are the incident and transmitted intensities of a light beam through a sample of path length L, respectively. The absorption coefficient $\alpha(\lambda)$ quantifies the magnitude of the absorption per unit length and is expressed as the product of the absorption cross-section σ [cm^2] and the molecular number density N [cm^{-3}] of

the absorbing sample $\alpha(\lambda) \equiv N\sigma(\lambda)$. Absorption occurs only at wavelengths that correspond to the transition energy between two quantum mechanical energy levels of the absorber gas. At wavelengths in the infrared region, absorption results from changes in vibrational and rotational energy states of a molecule, and as mentioned in the introduction, these energy states depend on the masses, configurations, and binding energies of the atoms in the molecule. The absorption spectra of different gases (e.g. CH_4, H_2O, and CO) thus differ for each, and as the energy states of a molecule depend on the atomic mass, isotopic variants of the same molecule can also be distinguished (e.g. $^{13}CO_2$ and $^{12}CO_2$). However, for weak absorptions (i.e. $ln(I/I_0) < 10^{-6}$) in gas measurements, the changes of light intensity passing through the sample is very small compared to the initial intensity; therefore, it is difficult to achieve an adequate signal-to-noise ratio to distinguish between I and I_0. The cavity ring-down method virtually eliminates this problem, since the principle of the CRDS is based on the measurement of a rate rather than the magnitude of intensity change. In this approach, the sensitivity measurement of a small absorption coefficient is also improved with a very long absorption path length. In a CRDS analyzer, the beam of a particular frequency laser enters a cavity consisting of a set of highly reflective mirrors aligned such that the laser beam forms a closed path on every round trip. When the laser is on, the cavity fills with circulating laser light until the photodetector signal reaches a threshold level; at this point, which is reached in less than 100 ns, the continuous wave laser into the cavity is abruptly switched off. The laser beam within the cavity bounces from mirror to mirror (over 20000 times and 10 km), and because the mirrors have less than 100% reflectivity, the light intensity leaks and decays exponentially to zero. The amount of time taken for this exponential decay is called ring-down time. When the cavity is evacuated, the ring-down time $\tau_0(\lambda)$ is solely dependent on the mirror reflectivity (R) at the path length (L)

$$\tau_0(\lambda) = \frac{L}{c(1-R)} \tag{3.2}$$

where c is the speed of light. If a gas sample is then introduced into the cavity, the absorption according to Beer Lambert's law will increase (Figure 3.1) and the ring-down time $\tau(\lambda)$

$$\tau(\lambda) = \frac{L}{c(1-R+\alpha(\lambda)L)} \tag{3.3}$$

will decrease and subsequently subtracting the ring-down times will yield

$$\alpha(\lambda) = \frac{1}{c}\left(\frac{1}{\tau(\lambda)} - \frac{1}{\tau_0(\lambda)}\right) \tag{3.4}$$

Once the absorption spectrum $\alpha(\lambda)$ of the sample has been measured (i.e., the height of an absorption peak), the sample concentration can be computed using the absorption cross-section and line shape parameters (Wahl et al., 2006).
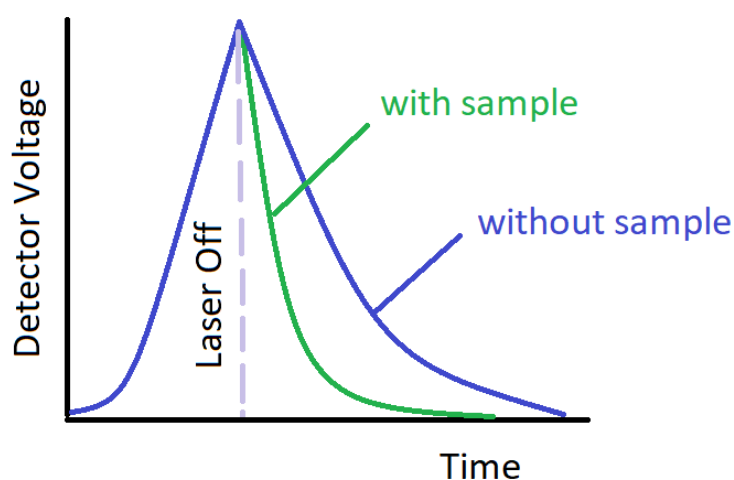
Figure 3.1: Schematic ring-down signals with (green curve) and without (blue curve) absorbing medium.

3.1.2 Spectroscopic interferences

In Picarro G1101-i, the stable isotope abundance is computed by measuring the two spectral absorption lines of $^{12}CO_2$ and $^{13}CO_2$, where the ratio of their peak heights is a measure of the ratio of the concentration of each of the two isotopologues, and the summation of the two respective concentrations is the absolute CO_2 concentration. Concentration measurements that are determined through light absorption can be affected by water vapor in the sample air in two ways. First through dilution of the sample air, which linearly depends on the water vapor concentration, and second by spectroscopic effects which directly modify the absorption spectrum (Rella, 2012).

Dilution: The dilution effect is the change of CO_2 and CH_4 mixing ratios due to the variability in humidity in such a way that the additional water vapor will decrease relative concentration of other gases. In contrast, a humid air mass that becomes drier (i.e., through condensation) will result in an inverse effect, increasing the mixing ratios of the other gases. In Picarro G1101-i, since $^{12}CO_2$ and $^{13}CO_2$ are equally affected, dilution may only alter the CO_2 concentration.

Spectral broadening: The Lorentzian broadening of the absorption spectral lines are affected by the presence or lack of water vapor since it is a major absorber of the infrared light. The effect on the two spectral lines ($^{12}CO_2$ and $^{13}CO_2$) is not necessarily the same, leading to an error in the reported isotope ratio as a function of water vapor concentration, but being independent of the carbon dioxide concentration.

Direct spectral interference: Direct interferences are caused by absorption spectral lines of water vapor that are in the vicinity of either $^{12}CO_2$ or $^{13}CO_2$ absorption spectral lines and cause offsets of both isotopologues and thus affect concentrations and the reported isotope ratio. In addition to water vapor direct interference, there is a significant

absorption by CH_4 in the frequency region where CO_2 isotopologues are measured. The presence of CH_4 causes a shift in the $\delta^{13}C$ toward a more 13-rich value, meaning the $^{13}CO_2$ peak appears to be stronger than it would be in the absence of CH_4 (Hoffnagle, 2013).

3.2 Characterizing anthropogenic CO_2 sources

In order to assist studies of the carbon cycle and to quantitatively determine carbon fluxes, the atmospheric CO_2 mixing ratio is monitored at various measurement sites. In top-down approaches, these CO_2 measurements are used to derive total CO_2 emissions; however, observations of atmospheric CO_2 mixing ratios alone are not sufficient to provide information on the contribution of biogenic and anthropogenic sources of CO_2 in the atmosphere. Several methods have been employed to address this topic and the Keeling plot method is one of the most reliable methods to identify source contributions (Ciais et al., 1995b). Furthermore, CO mixing ratios are often used as a proxy for anthropogenic CO_2 contributions (Vogel et al., 2010) and the strong correlation between CH_4 and CO_2 reveals that two gases share a common source (Hansen et al., 1989). The above will be explained further in the following sections, and these methods will be elaborated in more detail in chapter 4 (in the second paper). As an example one pollution event that was recorded at UFS in January 2014 (not published) is characterized using these three methods and visualized in Figure 3.2. Note that since the reason for a decrease in CO_2 concentration would be due to either a sink of CO_2 or a breakdown of the boundary layer inversion potentially associated with a change of catchment area of the measurement, in order to minimize these effects, only the front shoulder of the signal (shaded area in upper panels in Figure 3.2) is selected for the calculation.

3.2.1 $\delta^{13}CO_2$

Since different CO_2 reservoirs exhibit different isotopic compositions, the relative proportion of the isotopes in an air mass carries information on its origin. Therefore, the stable isotopic composition of CO_2 can potentially be a tracer to distinguish between different contributors to atmospheric CO_2. In this approach the Keeling plot (Keeling, 1958, 1960) is used to determine the mean isotopic source signature δ_S, based on the mass balance equations (Eq. 1.1 and 1.3), assuming that the total measured atmospheric CO_2 consists of added CO_2 from sources to the background concentration. The mean source signature is the mean of the isotopic signatures of all sources. In this study, the Keeling plot was applied only to the pronounced short-term variations in the CO_2 mixing ratio; thus, it was likely that only one source contributed to CO_2 variability. Solving the mass balance equations of CO_2 and $\delta^{13}C$ yields

$$\delta_{ATM} = \frac{1}{C_{ATM}} * constant + \delta_S \qquad (3.5)$$

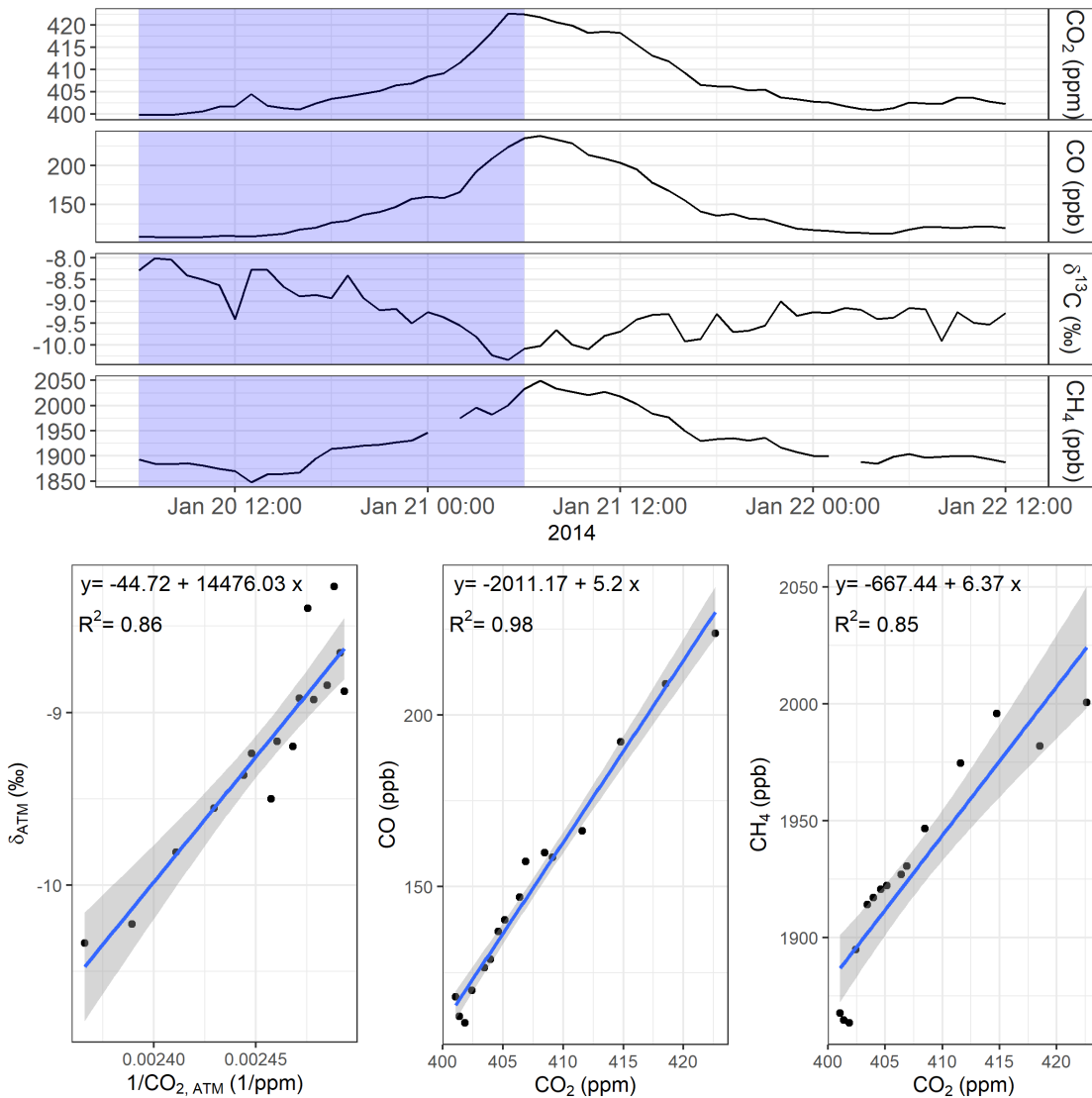In this equation, source signature δ_S is computed using CO_2 and $\delta^{13}C$ measurements

Figure 3.2: Example of a pollution event at UFS. Upper panels: temporal variation of the mixing ratios of CO$_2$, CO, and CH$_4$ as well as δ^{13}C (the shaded area is the selected period for further regression calculation). Lower panels: the Keeling plot (left); the intercept of the regression corresponds to the source isotopic signature. Linear regressions of hourly mean mixing ratios of CO$_2$ and CO (middle), and of CO$_2$ and CH$_4$ (right); the slope of the regressions corresponds to emission ratios. The shaded area is 95% confidence intervals of the regression line.

(C_{ATM} and δ_{ATM}). Source signature of the presented example determined following Eq. 3.5 is -44.72 $\pm$ 3.77‰ (see Figure 3.2).

3.2.2 CO/CO$_2$

The sources of atmospheric CO are both natural and anthropogenic. However, in Europe, approximately 70% of CO sources are anthropogenic since CO is often co-emitted during incomplete combustion (Pfister et al., 2004). Therefore, CO has often been used as a tracer for fossil fuel CO$_2$ emissions in order to distinguish the biospheric and the fossil fuel components (Lopez et al., 2013). The mean ratio of atmospheric CO to CO$_2$ (CO/CO$_2$) depends on the combustion and burning efficiency, and on the fuel type, and it can range from 17.5 ppb/ppm for industrial sources to 4.1 ppb/ppm for vehicular traffic. Nevertheless, in Europe improvements in combustion efficiency due to regulations under the pressure of pollution reduction policies may lead to a significant reduction in CO emissions and in consequence in CO/CO$_2$ ratios (Popa et al., 2014). CO/CO$_2$ emission ratio of the example is 5.20 ± 0.21 ppb/ppm (see Figure 3.2).

3.2.3 CH$_4$/CO$_2$

CH$_4$ is a key component in atmospheric chemistry and, after CO$_2$ and water vapor, is the most important greenhouse gas, as it is responsible for about 20% of the anthropogenic radiative forcing (Forster et al., 2007). Its short atmospheric lifetime of $\sim$9 years makes it a good candidate for greenhouse gas emission reduction measures. CH$_4$ in Europe mainly comes from anthropogenic sources; therefore, the CH$_4$ to CO$_2$ emission ratio (CH$_4$/CO$_2$) is utilized as an indication of various types of anthropogenic sources (Conway et al., 1994). CH$_4$/CO$_2$ emission ratio of the example is 6.37 ± 0.73 ppb/ppm (see Figure 3.2).

3.3 Backward trajectories

Air mass backward trajectory analysis is a commonly applied tool to identify source-receptor relationships and examine the long-range transport and its effect on the observed composition. Back trajectories are used for many purposes e.g. to detect the sources of air masses in air quality research (Ghasemifard et al., 2020; Camalier et al., 2007; Stein et al., 2007; Jung et al., 2010) or in palynology (Šikoparija et al., 2013; Makra et al., 2010; Hernández-Ceballos et al., 2014) by estimating the paths of air parcels arriving at the region of interest. They are often used to filter air mass origins, allowing for refined trend analyses, and also in cluster analyses (Lee et al., 1998; Gardner and Dorling, 2000; Prevedouros et al., 2004). Back trajectories are modeled e.g. by the FLEXTRA model that was developed at the Institute of Meteorology and Geophysics in Vienna by Stohl et al. (1995), by the UK universities' Global Atmospheric Modelling Programme (UGAMP) trajectory model that has been used in many field campaigns (Cape et al., 2000; Methven et al., 2006), and by the Hybrid Single-Particle Lagrangian Integrated Trajectory (HYSPLIT) model (Draxler and Rolph, 2003). Fleming et al. (2012) have presented a comprehensive overview of the existing approaches and Gebhart et al. (2005) have carried out a thorough comparison of various trajectory models and

meteorological parameters. In this dissertation, the trajectory calculation function is taken from the HYSPLIT model. Therefore, in the following sections, the focus would be on introducing this model and visualizing some of its features, the methods used to detect the air mass origin and emission source, as well as cluster analysis. Platform and software products that enable use of HYSPLIT calculation and data analysis are also introduced.

3.3.1 HYSPLIT model

The HYSPLIT model, developed by The National Oceanic and Atmospheric Administration (NOAA) Air Resources Laboratory (ARL), is one of the most extensively used models for atmospheric transport and dispersion calculations in the atmospheric sciences community (Stein et al., 2015). The model calculation method is a hybrid of the Lagrangian approach and the Eulerian methodology (Stohl, 1996; Draxler and Hess, 1998). It uses a moving reference frame for the advection and diffusion calculations of the trajectories' movement (Lagrangian framework) and a fixed three-dimensional grid to compute concentrations of air pollutant. Many upgrades in the computation of dispersion and transport have been implemented in HYSPLIT over the last 20 years and the most recent update, v.4.2.0, was revised in September 2019. Nevertheless, the basis for the trajectory calculations remains the same. In the computation of a single particle trajectory, it is assumed that a particle is passively moved with the wind. Therefore, the meteorological fields are directly incorporated into the advection algorithm, which is computed at time step $(t + \Delta t)$ from the average of three-dimensional velocity vectors (V), interpolated in time and space, for the initial position $P(t)$ and the first-guess position $P'(t + \Delta t)$,

$$P'(t + \Delta t) = P(t) + V(P, t)\Delta t \tag{3.6}$$

and the final position is

$$P(t + \Delta t) = P(t) + 0.5[V(P, t) + V(P', t + \Delta t)]\Delta t \tag{3.7}$$

[Model features, updates, and further information can be found on the HYSPLIT website `https://www.ready.noaa.gov/HYSPLIT.php`.] In this study, the simulations of back trajectories were processed on the Compute Cloud of the Leibniz Supercomputing Centre (LRZ), Garching, Germany. The underlying meteorological model was obtained from the Global Forecast System (GFS) and was driven by 3-h forecast weather data at a 0.5° resolution. Backward trajectories ending at the receptor (measurement) site were calculated hourly for 96 hours for the entire measurement period (May 2012 to November 2014). While setting up the model configurations, the operator specifies the meteorological variables that should be exported along with trajectories data. Depending on the type of study, these variables could be ambient temperature, precipitation, mixing depth, relative and specific humidity, water vapor mixing ratio, solar radiation, and terrain height. Of all these, mixing depth was the most interesting and relevant variable

for our study. Mixing depth is in fact the planetary boundary layer (PBL) height, and diurnal changes in the PBL height cause variations in atmospheric measurements at the site, which has been used as a filter for the air masses from free troposphere or air masses influenced by PBL (see Sect. 4.1).

In order to analyze the association between trajectories and the atmospheric concentrations of various gases arriving at the measurement site, a multitude of methods to perform trajectory classifications have been devised. In general, there are two methodological approaches. In the first, in order to link the atmospheric composition and air mass origin, trajectories are analyzed focusing on the exceedance levels and detecting the main designated air mass sectors; the commonly-used functions is Potential Source Contribution Function (PSCF). The second is to cluster the trajectories using multivariate statistical techniques and analyzing the concentration at the measurement site to examine the differences among clusters. The principle behind PSCF and cluster analyses is explained in the following section.

3.3.2 Potential Source Contribution Function (PSCF)

The probability of an air mass arriving at the receptor site is calculated with a probability function for grid cells that are superimposed over specific regions of interest (Ashbaugh et al., 1985). The PSCF, a conditional probability, describes the spatial distribution of probable source locations derived by trajectories arriving at the measurement site. A trajectory endpoint lies on a grid cell of latitude-longitude coordinates, (i,j). Next, the PSCF value is defined as the probability that an air parcel passing through the ijth grid cell has a high concentration (e.g. >95th percentile) at the time of arrival:

$$PSCF = \frac{m_{ij}}{n_{ij}} \tag{3.8}$$

where n_{ij} is the total number of air masses with endpoints that fall in the ijth cell, and m_{ij} is the number of segment trajectory endpoints in the ijth cell that arrives at the measurement site at a time when a measured concentration is greater than an arbitrary criterion value. In PSCF analysis, small values of n_{ij} can produce high PSCF values with high uncertainties and in order to minimize this artifact, an empirical weight function $W(n_{ij})$ is applied:

$$W(n_{ij}) = \begin{cases} 0.75 & n < N < 2n \\ 0.50 & \frac{n}{2} < N < n \\ 0.15 & N < \frac{n}{2} \end{cases} \tag{3.9}$$

where N is the number of the end point per cell and n is the average of N of all cells. PSCF function was used to detect the spatial and geographical regions with an influence on the measured CO_2 and $\delta^{13}C$. As an example, a PSCF map explicitly for air masses causing extremely high CO_2 concentrations in January 2014 (presented in Sect. 3.2)

is shown in Figure 3.3 and depict that the air masses can be traced back to the high emission regions in the German Ruhr area.
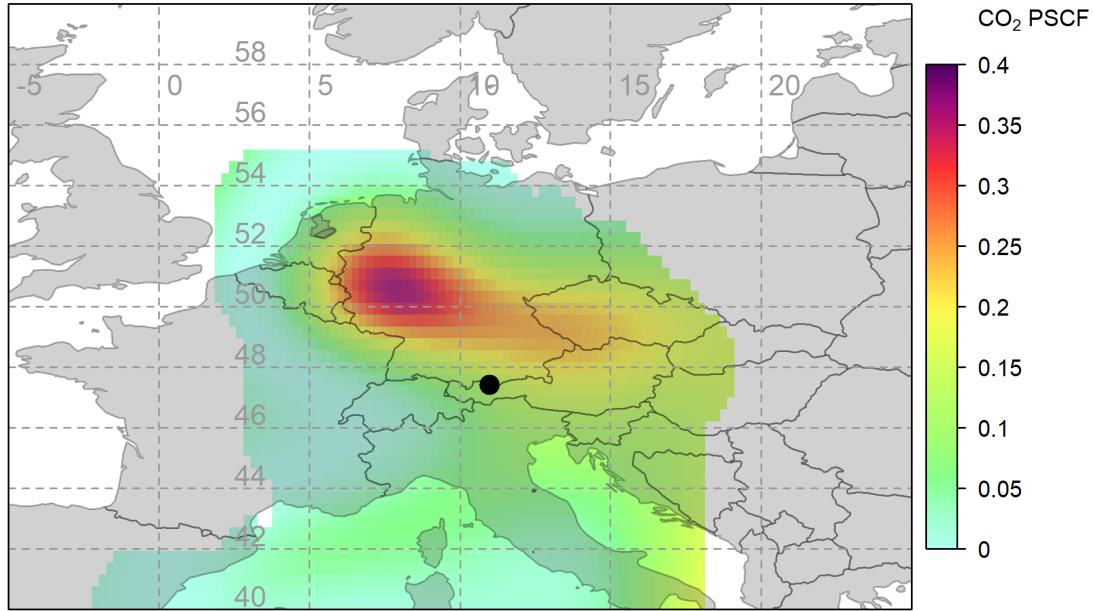

Figure 3.3: Potential source contribution function (PSCF) plot of CO_2 mixing ratio measured at UFS (January 20-22, 2014) and attributed to a pollution event.

3.3.3 Cluster analysis

A cluster analysis, which assigns trajectories into representative special groups, maximizes the homogeneity of elements within the clusters and the heterogeneity among the clusters. The trajectory clustering technique is a common method for combining gas measurements and air mass transport pathways at a receptor site to post-process data according to cluster origin. In order to perform cluster analysis different algorithms (Brankova et al., 1998; Dorling et al., 1992; Sirois and Bottenheim, 1995) can be applied. They differ in how the distance matrix is calculated in order to determine the similarity or differences of back trajectories. Euclidean distance, the simplest calculation, defines the distance between two trajectories using the latitude (X) and longitude (Y) locations as variables. The distance is given by

$$d_{12} = \sqrt{\sum_{i=1}^{n}((X_1(i) - X_2(i))^2 + (Y_1(i) - Y_2(i))^2)} \tag{3.10}$$

where n is the number of back trajectory points (e.g., 96 hours in this study), X_1, Y_1 and X_2, Y_2 are the coordinates of back trajectories 1 and 2, respectively. The disadvantage of

using this algorithm is that when two backward trajectories follow the same path but one has a higher speed, they may be classified into two different clusters. Therefore, if the purpose is to determine from which direction the air masses reach the site, angle distance is a better parameter (Sirois and Bottenheim, 1995). The angle distance matrix is a measure of similarity of two back trajectory points in terms of their angle from the origin. The angle distance is defined as

$$d_{12} = \frac{1}{n} \sum_{i=1}^{n} \cos^{-1}(0.5 \frac{A_i + B_i + C_i}{\sqrt{A_i B_i}})$$ (3.11)

where

$$A_i = (X_1(i) - X_0)^2 + (Y_1(i) - Y_0)^2$$ (3.12)

$$B_i = (X_2(i) - X_0)^2 + (Y_2(i) - Y_0)^2$$ (3.13)

$$C_i = (X_2(i) - X_1(i))^2 + (Y_2(i) - Y_1(i))^2$$ (3.14)

The variables X_0 and Y_0 define the coordinates of the location (backward trajectory origin point) and d_{12} is the mean angle between the two backward trajectories.

In this work, 2.5-year trajectories were grouped in five clusters to each cluster represents at least 10% of the trajectories. Further, each cluster was filtered and split into two classes depending on the trajectories and mixing layer heights. When trajectories all time steps travel above the mixing layer height are in FT (free troposphere) class otherwise PBL influenced. Summer had the most PBL influenced air masses (21.3%) and winter had the lowest (10.3%). Spring and autumn air masses had contact with the PBL in 14.6% and 12.6%, respectively.

3.3.4 Openair, R package

A back trajectory calculation is time-consuming, particularly when several sites are studied for multiple year. In addition, assessing back trajectory data can be complicated. In order to overcome some of these issues and to extend the possibilities for data analysis, several platforms (web- and pc-based), as well as software packages, are available. READY (Real-time Environmental Applications and Display sYstem), a web-based system developed by ARL (`http://ready.arl.noaa.gov/`), allows users to run the HYSPLIT transport and dispersion model interactively on the NOAA ARL web server. The HYSPLIT can also be installed on a PC (LINUX, Windows, and Mac) and run using script or a graphical user interface. A geographic information system (GIS) based software application called TrajStat was developed for spatial data management, visualization, and analyses (Wang et al., 2009). It is windows-based and freely available at `http://www.arl.noaa.gov/ready/hysplit4.html` and uses various trajectory statistical analysis methods (i.e., Clustering and PSCF) to identify potential sources from long-term air pollution measurement data. Openair is an R package developed for the purpose of analyzing air quality data and provides several functions to assess and analyze pre-calculated back trajectories (Carslaw and Ropkins, 2012). Pre-calculated back trajectories

use the HYSPLIT trajectory model for specific locations and stored as .RData objects. Nevertheless, users can run HYSPLIT in other software, yet analyze the calculated trajectories with Openair functions. This package is extensively used in the publications that form a part of this dissertation.

3.4 Software used

For data analysis and statistical parts, the R programming language was used together with the following packages:

- IDPmisc (Locher et al., 2012)

- pspline (Ramsay et al., 1997)

- Openair (Carslaw and Ropkins, 2012)

- ggplot2 (Wickham, 2011)

4 Publications: summaries and contributions

The two following published manuscripts, in internationally recognized, peer-reviewed journals, provide the basis for this dissertation:

(i) Homa Ghasemifard, Ye Yuan, Marvin Luepke, Christian Schunk, Jia Chen, Ludwig Ries, Michael Leuchner, and Annette Menzel. "Atmospheric CO_2 and $\delta^{13}C$ measurements from 2012 to 2014 at the environmental research station Schneefernerhaus, Germany: Technical Corrections, Temporal Variations and Trajectory Clustering" Aerosol Air Quality Research 19 (2019): 657-670. `DOI:10.4209/aaqr.2018.01.0010`

(ii) Homa Ghasemifard, Felix R. Vogel, Ye Yuan, Marvin Luepke, Jia Chen, Ludwig Ries, Michael Leuchner, Christian Schunk, Sanam Noreen Vardag, and Annette Menzel. "Pollution Events at the High-Altitude Mountain Site Zugspitze-Schneefernerhaus (2670 m asl), Germany." Atmosphere 10, no. 6 (2019): 330. `DOI:10.3390/atmos10060330`

In the following, a summary of the publications along with details on the particular contributions are given. In the contribution, author's names are abbreviated with their initials, for example, Homa Ghasemifard as HG, except for Michael Leuchner, his abbreviation is MLe.

The entire articles can be found in Appendix.

4.1 Technical corrections, temporal variations and trajectory clustering

Homa Ghasemifard, Ye Yuan, Marvin Luepke, Christian Schunk, Jia Chen, Ludwig Ries, Michael Leuchner, and Annette Menzel. "Atmospheric CO_2 and $\delta^{13}C$ measurements from 2012 to 2014 at the environmental research station Schneefernerhaus, Germany: Technical Corrections, Temporal Variations and Trajectory Clustering" Aerosol Air Quality Research 19 (2019): 657-670. `DOI:10.4209/aaqr.2018.01.0010`

Summary

This study presents continuous atmospheric CO_2 and $\delta^{13}C$ measurements by wavelength-scanned cavity ring down spectroscopy (Picarro G1101-i) at the high-mountain station Schneefernerhaus, Germany. $\delta^{13}C$ values were post-corrected for methane and water spectral interferences using accompanying measurements of CH_4 and H_2O, and CO_2 in dried air, respectively. The best precision of $\pm0.2‰$ for $\delta^{13}C$ and of ±4 ppb for CO_2 was obtained with an integration time of about 1 hour for $\delta^{13}C$ and 2 hours for CO_2. The seasonality of CO_2 and $\delta^{13}C$ was studied by fitting background curves for a complete 2-year period. Peak-to-peak amplitudes of the averaged seasonal cycle were 15.5 ± 0.15 ppm for CO_2 and $1.97 \pm 0.53‰$ for $\delta^{13}C$, respectively. Based on the HYSPLIT Model, air masses were classified into five clusters, with westerly and northeasterly flows being the most and the least frequent, respectively. In the wintertime, northwest and northeast clusters had a higher median level for ΔCO_2 and a lower medial level for $\Delta\delta^{13}C$ (the difference between observed and background concentrations), likely caused by anthropogenic emissions. In the summertime, air masses from the northwest had the lowest ΔCO_2 and the highest $\Delta\delta^{13}C$. Potential source contribution functions (PSCFs) were used to identify the potential source and sink areas. In winter, source areas for high CO_2 mixing ratios ($>75^{th}$ percentile) were mainly located in northwestern Europe. In summer, areas with high $\delta^{13}C$ ratios ($>75^{th}$ percentile), indicating a carbon sink, were observed in the air from Eastern and Central Poland.

Contributions

HG, JC, and AM conceptualized the research idea. All authors contributed to the corrections and selections of measured data. CS and MLe recorded the data (CO_2 and $\delta^{13}C$) and maintained the measurement device, and LR provided CO_2 data measured by UBA. HG performed the data processing with support from YY and ML. HG visualized the backward trajectories with support from ML. HG analyzed the data and wrote the manuscript. All authors contributed to the interpretation of results and editing of the manuscript.

4.2 Real–time observation of pollution events

Summary

Within the CO_2 time series measured at the Environmental Research Station Schneefernerhaus (UFS), Germany, as part of the Global Atmospheric Watch (GAW) program, pollution episodes are traced back to local and regional emissions, identified by $\delta^{13}C(CO_2)$ as well as ratios of CO and CH_4 to CO_2 mixing ratios. Seven episodes of sudden enhancements in the tropospheric CO_2 mixing ratio are identified in the measurements of mixing/isotopic ratios during five winter months from October 2012 to February 2013. The short-term CO_2 variations are closely correlated with changes in CO and CH_4 mixing ratios, achieving mean values of 6.0 ± 0.2 ppb/ppm for CO/CO_2 and 6.0 ± 0.1 ppb/ppm for CH_4/CO_2. The estimated isotopic signature of CO_2 sources (δ_s) ranges between -35% and -24%, with higher values indicating contributions from coal combustion or wood burning, and lower values being the result of natural gas or gasoline. Moving Keeling plots with site-specific data selection criteria are applied to detect these pollution events. Furthermore, the HYSPLIT trajectory model is utilized to identify the trajectories during periods with CO_2 peak events. Short trajectories are found covering Western and Central Europe, while clean air masses flow from the Atlantic Ocean and the Arctic Ocean.

Contributions

HG, FRV, JC, LR, and AM conceptualized the research idea. CS and MLe recorded the data (CO_2 and $\delta^{13}C$) and maintained the measurement device, and LR provided CH_4 and CO data. HG performed the data processing with support from SNV, YY, and FRV. HG visualized the backward trajectories with support from ML. All authors contributed to the interpretation of results and editing of the manuscript.

5 Discussion

5.1 Analyzer and corrections

The CRDS analyzer in this study was acquired long before any of the literature on its problems and dependencies had been published, and the measurement also started before the CH_4 interference had been found. The assumption was that the analyzer could be used as described by the manufacturer. Thus, the number of corrections was only known at the end of the measurements and given that the analyzer itself was no longer operational, the best alternative to do was to perform all available post-processing corrections and selections on the data recorded. Several studies from Picarro and other groups have evaluated, compared, and validated the measurements recorded by the non-upgraded and upgraded G1101-i analyzers. Nevertheless, in the following, some discussion on the performance of this device and justifications for the corrections are presented.

5.1.1 Precision of measurement

The stability and precision of the measurement device were assessed using Allan deviation/variance analysis and compared to studies with a similar measurement device. In order to conduct the Allan variance analysis measuring a stable gas source for 24 hours is common practice [cf. Pang et al. (2016); Wen et al. (2013)]. The best precision of the instrument was obtained as 4 ppb for CO_2 and 0.2‰ for $\delta^{13}C$ and the precision at an integration time of 30 minutes was obtained as 5-6 ppb for CO_2 and 0.4‰ for $\delta^{13}C$. The precision is slightly better than the specification provided by the manufacturer: 50 ppbv for CO_2 at one minute average and 0.3‰ for $\delta^{13}C$ at five minutes average (Picarro G1110-i datasheet, 2008).

5.1.2 Calibration

Measurements of CO_2 and $\delta^{13}C$ were calibrated with two-point high and low concentrations [i.e., gain and offset method (Wen et al., 2013)] by two working standard gases and each was measured every 7 days for one hour. The frequency and duration of calibrations were based on recommendations by the manufacturer/importer, since none of the technical papers (Vogel et al., 2013; Nara et al., 2012; Pang et al., 2016; Wen et al., 2013) had been published at the time of setup and operation. From a number of tests carried out it was found that a 10 min or even 30 min calibration time (as reported in the literature above) would not be sufficient to account for short-term variability. Thus

calibrations of one hour for each standard gas, which at the time seemed to match the recommended calibration interval regarding the measurement to calibration time ratio, were performed. Regarding the results of the Allan deviation and literature that has become available since, short-term variabilities might be hidden in the time frame of longer than one-hour averaging. Furthermore, it is recommended in order to minimize the risk of fractionation between the gas components in the gas cylinders, to storage them horizontally (WMO 2009). Since two standard gas cylinders were kept vertically, in order to confirm the quality of the calibration and the stability of the standards, at the end of the analyzer operation, both standard gases were reanalyzed at the laboratory of the Max Planck Institute for Biogeochemistry (MPI-BGC), Jena, Germany. The measured δ^{13}C values agreed well with the values from the manufacture and were within the given range of GAW data quality objectives (±0.01‰). Based on the available calibration data, several temporal calibration strategies were attempted, including the use of linear interpolation and the smoothing spline. Deviations of the corrected data using the spline-interpolation of calibration coefficients turned out lower (0.0 ± 0.44‰ and 0.0 ± 0.32‰) than the linear interpolation (0.05 ± 0.75‰ and 0.03 ± 0.53‰); therefore, the smoothing spline was employed. Uncertainty of calibration based on the National Ecological Observatory Network calculation (Csavina et al., 2017) is estimated to be ±0.56 ppm for CO_2 and ±0.53‰ for δ^{13}C.

5.1.3 Post correction of CO_2

In order to correct the recorded CO_2 mixing ratio, the time variation of atmospheric CO_2 concentration measured by Picarro G1101-i and Picarro EnviroSense 3000i were compared in two separated phases, before and after pump replacement. The simple pump replacement itself does not seem a strong enough explanation for the observed shift in correlation; however, the timing of the pump replacement fits very well with the change in instrument behavior. Therefore, this time was used to separate the data. The physical explanation of this behavior can no longer be determined (e.g. there could have been some cavity contamination at the time of pump failure or replacement). This comparison between two CO_2 mixing ratios is valid because both instruments used the same inlet line and were also operated in the same air-conditioned laboratory. The only difference between the two devices was that the sample air of the G1101-i was not dried, whereas the EnviroSense 3000i's airstream was treated using a cooling trap technique in which the water vapor is removed at a temperature of -80 °C; rendering water vapor constant, very small and thus negligible. The result of this comparison in both phases suggested that the difference between the two measurements was systematic and became larger as the H_2O concentration increased (i.e., in the summertime) and was caused by the dilution effect as pointed out in Sect. 3.1.2. A similar comparison between the same Picarro G1101-i and Los Gatos DLT-100 was performed by Wen et al. (2013) for a few days, and the corresponding dilution effect was an underestimation of 0.1 ppm at 400 ppm of CO_2. The water dilution and broadening effect were supposed to be corrected by firmware embedded in the instrument, but Wen et al. (2013) reported that

the correction coefficients provided by the manufacturer were erroneous and resulted in a large correction on water vapor effect. Thanks to the parallel CO_2 measurement by the German Environment Agency (Umweltbundesamt, UBA), we were able to correct the dilution effect using the water vapor and CO_2 concentration but were unable to remove the smaller effect caused by spectral broadening and interference (Nara et al., 2012; Rella et al., 2013) which explain the very small differences between the two analyzers (Rella, 2012), 0.01 ± 0.42 ppm before and 0.02 ± 0.06 ppm after pump replacement. However, corrected CO_2 data is still in accordance with the GAW data quality objectives (±0.1 ppm) (WMO, 2016).

5.1.4 Post calculation of δ^{13}C

Carbon isotope ratios are calculated by measuring the relative concentrations of the two isotopologues of CO_2, which are the peak heights of $^{12}CO_2$ and $^{13}CO_2$. While Vogel et al. (2013) showed that there is no significant concentration dependence of δ^{13}C in the CO_2 range of 303–437 ppm for the G1101-i analyzer, both water vapor and methane have complicated spectra with the optical absorption in the frequency region of the CO_2 measurement. For the purpose of post-correcting, isotopic data was recomputed including two terms implementing the correction for water and methane interferences. The CH_4 concentration, reported by UBA using a Picarro EnviroSense 3000i, is added to all $^{13}CO_2$ entries, and water concentration, which is tabulated in data files, is added to the linear calculation of delta as an extra offset. According to Nara et al. (2012), the dependencies of δ^{13}C and CO_2 on the N_2/O_2 ratio and argon are negligible for natural variations in ambient air, but they may of significant influence for synthetic standard gases, which have been empirically described for the EnviroSense 3000i, G-1301 and G-2301 instruments (non-isotopic analyzers). However, no information was found regarding the N_2/O_2 ratio and argon influences or corrections for our analyzer [e.g. in Vogel et al. (2013); Pang et al. (2016); Wen et al. (2013)]. In fact, none of these publications even indicate whether they used synthetic or ambient air-based standards. A new isotopic CO_2 measurement device has been operating at UFS since May 2017, and the measurements (not yet published) are in a good agreement with recorded δ^{13}C regarding variability, diurnal cycle and amplitude.

5.2 Diurnal variations

The maximum concentrations of the CO_2 mixing ratio occur at 09–10 in the morning in most seasons. Similar results were also reported by Sturm et al. (2013) for the JFJ site. Further, Lan et al. (2020) reported diurnal cycles of CO_2 in Munich reaching maximums two to three hours earlier. The diurnal delay compared to urban studies might be related to the long distance to sinks and sources. The highest daily peak to peak amplitudes of CO_2 and δ^{13}C at UFS were measured in summer at 2.9 ppm and 0.4‰, whereas these values at JFJ were 2 ppm and 0.1‰, respectively. Differences in diurnal cycles are likely caused by elevation differences of the measurement sites; i.e. UFS is located at a lower

elevation (-930 m), closer to sinks and sources in the valley, and also because there are more tourist activities in the vicinity of UFS. In contrast, urban sites that are influenced more strongly by anthropogenic sources have very pronounced diurnal variabilities, e.g. more than 30 ppm in summer in Munich (Lan et al., 2020, 2019).

5.3 Isotopic source signatures

In order to routinely detect periods of local and regional pollution events in continuous measurements of CO_2 and $\delta^{13}C(CO_2)$ at the remote elevated station UFS, the moving Keeling plot method based on Vardag et al. (2016) was applied. In this method specific criteria regarding site characteristics are adjusted. In the 2.5 years of recorded data, 14 events with a strong increase ($>\sim$15 ppm) in the measured CO_2 concentration were detected (only seven events have been published), eight events in cold seasons (October–February) and six events in warm seasons (May–July). The determination of a source signature yields reasonable results only if the mean source mix and the background concentration remain constant, and also if sources and sinks do not occur simultaneously (Miller and Tans, 2003). In order to minimize the effect of the terrestrial biosphere (i.e., photosynthesis and respiration) in the interpretation of pollution signals, only cold season events were selected. Seven events (E1–E7) are presented in the second publication and the eighth event (E8) is presented in Sect. 3.2 as an unpublished event. Since data points were averaged hourly from the 10-second temporal resolution data, a single point measurement contains continuous information on the one-hour period. The isotopic source signatures can be categorized into two groups, (1) the most enriched signatures, -24.2‰ and -26.3‰ (E1 and E2), are in the range of wood burning or coal combustion; (2) E3–E7, with an average value of -29‰, are in the range of natural gas and gasoline combustion which agree well with isotope ratio measurements of tropospheric CO_2 at the high Alpine research station JFJ at an altitude of 3580 m a.s.l. Tuzson et al. (2011) detected pollution events in which pronounced variations of atmospheric CO_2 mixing ratio and $\delta^{13}C$ were recorded. The isotopic composition values of pollution sources ranged between -27‰ and -30‰. Low values (-28.3‰ to -29.7‰) suggest a contribution from gasoline combustion and the high value (-27.6‰) was consistent with a contribution from coal and wood burning. E8 (see Sect. 3.2) has the most depleted source signature, -44.72 ± 3.77‰, and is consistent with natural gas combustion. More characteristics of this event will be discussed in the following sections.

5.4 Emission ratios

Carbon dioxide, carbon monoxide, and methane have long atmospheric residence times and go through the same dispersion and long-range transport. The correlations between the concentration ratios (i.e., CO/CO_2 and CH_4/CO_2) are characteristic of the sources. High correlations ($R^2>90$) indicate a common source or a given combination of sources. The CO/CO_2 ratios varied between 3.5 and 8.0 ppb/ppm and the CH_4/CO_2 ratios

ranged from 4.7 to 7.4 ppb/ppm. Several studies have already reported CO/CO_2 and CH_4/CO_2 ratios in Europe and the average emission ratio at UFS falls in these range. However, the values are generally lower than measured ratios for traffic, and lower than the overall emission ratio reported for fossil fuel combustion at European sites. High CO/CO_2 values, such as 7.3 to 13.1 ppb/ppm at JFJ (Tuzson et al., 2011) might be due to contributions from biogenic sources since they uptake CO_2 and leave CO unaffected. Nevertheless, technological developments in vehicles resulting in lower CO emissions are partly responsible for the decrease in CO/CO_2 emission ratios (Popa et al., 2014). It is likely that the overall anthropogenic emissions of CO in Europe, and consequently CO/CO_2 emission ratios, continue to decrease due to the pressure of pollution reduction policies leading to cleaner technologies. The CO/CO_2 emission ratio of E8, 5.20 ± 0.21 ppb/ppm, was in the same range as other events. Similar to CO, a decrease in anthropogenic CH_4 emissions in Europe and Siberia led to lower ratios of CH_4/CO_2 between the years 1988 and 2005 (Worthy et al., 2009). Further, the CH_4/CO_2 emission ratios obtained in this study agreed well with the results, reflecting the local traffic and transport characteristics of the western European vehicle fleet.

5.5 Trajectories

Short-term fluctuations of CO_2 reflect the influence of regional gas emitters and/or absorbers. In this study, the trajectory model was used to identify the most relevant regions appearing as CO_2 sources or sinks with high spatial resolution. Trajectories are a representation of the path that air masses have covered from the receptor site backward in time, thereby providing a history of crossed source and sink regions.

5.5.1 Back trajectory clusters

The results of the 2.5-year backward trajectories were initially presented in cluster analysis, grouping the air masses in five clusters. The west flow was dominant (41.7%) followed by northwestern (19.5%) and southwestern (14.9%) flows. Merging hourly CO_2 and $\delta^{13}C(CO_2)$ measurements with respective clusters, in winter, air masses with high CO_2 concentrations and low $\delta^{13}C$ were from the northeast and northwest and in summer the highest $\delta^{13}C$ and lowest CO_2 concentrations were from the northeast. In a similar study at JFJ, four years of CO_2 and $\delta^{13}C$ measurements using a footprint clustering analysis in wintertime revealed that the two clusters representing air masses with high CO_2 concentrations mostly had contact over Northern and Eastern Europe (Sturm et al., 2013), which is in accordance with results of northwest and northeast clusters for the UFS.

5.5.2 Source and sink regions

Another outcome from the trajectory analyses was that the origin could be identified using Potential Source Contribution Functions (PSCF). In the first paper, two clusters

with high CO_2 concentrations ($>75^{th}$ percentile) in winter and one cluster with the highest $\delta^{13}C$ ratio ($>75^{th}$ percentile) in summer were selected to represent the origin of CO_2 sources and sinks. PSCF maps showed that the sources of the air masses from the northwest cluster are Northwestern Europe, including regions of the Netherlands and the German Ruhr area, and sources for the northeast cluster are coal mining areas in Lusatia and Eastern Germany. In summer, the PSCF map revealed that potential sink origins are in Poland. In the second paper, PSCF was calculated for pollution events (E3–E7) and parts of Germany were included in all events as source regions. According to the European Environment Agency (EEA, 2012), Germany has the highest greenhouse gas emissions in Europe, which is typically associated with energy supply, energy use, and transportation. The PSCF map for E8, Figure 3.3, showed the high emission Ruhr area as the source region and partly overlapped with the detected sources in the northwest cluster in the first paper. E8 lasted for 16 hours and, except for two hours, the entire event trajectories' height touched the boundary layer and therefore carried information from the mixing layer.

6 Conclusion

The Environmental Research Station Schneefernerhaus (UFS) is part of GAW measurement network and provides concentrations of atmospheric constituents such as greenhouse gases, which can be used to obtain a regional estimate of total net greenhouse gases. Identifying the occurrence of disturbed air masses (i.e. influenced by regional pollution sources) as well as undisturbed free troposphere at UFS (and other mountainous sites) is vital for interpreting data from such measurement sites.

The results obtained in this dissertation yielded a better understanding of the measurement site UFS. δ^{13}C ratio is the first demonstration of long-term in-situ isotope measurements of CO_2 under free tropospheric conditions at UFS. Diurnal variations in CO_2 concentration and δ^{13}C ratio suggests that the site is occasionally influenced by free tropospheric and atmospheric boundary layer air masses as shown by other methods by Yuan et al. (2019) and Sigmund et al. (2019). Moving Keeling plot detected pollution events as well as their isotopic source signatures pointing to contributions from coal combustion and wood burning as well as from natural gas and gasoline. CO/CO_2 and CH_4/CO_2 emission ratios of different sources of pollution events revealed that fluctuations in atmospheric CO_2 mixing ratios were due to anthropogenic emissions related to road-transport and traffic.

Variabilities in concentrations depend on the origin of the air masses arriving at UFS. Regarding the clustering of trajectories, five air pathways with different origins and properties advecting air masses to UFS were identified. Polluted air masses originated primarily from coal mining area in Eastern Germany, industrial German Ruhr area, the Netherlands as well as from the local Alpine valleys.

Finally, post calculations and corrections of CO_2 and δ^{13}C would not have been feasible if there were no access to parallel measured CO_2, CH_4, and water vapor. Therefore, from the knowledge obtained, it is extremely important to add a reliable drying system to the sample inlet line when measuring atmospheric CO_2. In order to track the precision of such a measurement, it is also recommended repeating the Allan deviation plot (Chen et al., 2016), meaning to measure standard gases for 24 hours repeatedly throughout year.

References

Alden, C., Miller, J., and White, J. (2010). Can bottom-up ocean CO_2 fluxes be reconciled with atmospheric ^{13}C observations? *Tellus B: Chemical and Physical Meteorology*, 62(5):369–388.

Andreae, M. O. and Merlet, P. (2001). Emission of trace gases and aerosols from biomass burning. *Global Biogeochemical Cycles*, 15(4):955–966.

Apadula, F. (2003). Localization of source and sink regions of carbon dioxide through the method of the synoptic air trajectory statistics. *Atmospheric Environment*, 37(27):3757–3770.

Ashbaugh, L. L., Malm, W. C., and Sadeh, W. Z. (1985). A residence time probability analysis of sulfur concentrations at grand canyon national park. *Atmospheric Environment (1967)*, 19(8):1263–1270.

Brankova, E., Rao, S. T., Porter, and P.Steven (1998). A trajectory-clustering-correlation methodology for examining the long-range transport of air pollutants. *Atmospheric Environment*, 32(9):1525–1534.

Camalier, L., Cox, W., and Dolwick, P. (2007). The effects of meteorology on ozone in urban areas and their use in assessing ozone trends. *Atmospheric Environment*, 41(33):7127–7137.

Cape, J., Methven, J., and Hudson, L. (2000). The use of trajectory cluster analysis to interpret trace gas measurements at mace head, ireland. *Atmospheric Environment*, 34(22):3651–3663.

Carslaw, D. C. and Ropkins, K. (2012). Openair—an R package for air quality data analysis. *Environmental Modelling & Software*, 27:52–61.

Cerling, T. E., Ehleringer, J. R., and Harris, J. M. (1998). Carbon dioxide starvation, the development of C4 ecosystems, and mammalian evolution. *Philosophical transactions of the Royal Society of London. Series B, Biological sciences*, 353(1365):159–70; discussion 170–1.

Chen, J., Viatte, C., Hedelius, J. K., Jones, T., Franklin, J. E., Parker, H., Gottlieb, E. W., Wennberg, P. O., Dubey, M. K., and Wofsy, S. C. (2016). Differential column measurements using compact solar-tracking spectrometers. *Atmospheric Chemistry and Physics*, 16(13):8479–8498.

Ciais, P., Reichstein, M., Viovy, N., Granier, A., Ogée, J., Allard, V., Aubinet, M., Buchmann, N., Bernhofer, C., Carrara, A., Chevallier, F., Noblet, N. D., Friend, A. D., Friedlingstein, P., Grünwald, T., Heinesch, B., Keronen, P., Knohl, A., Krinner, G., Loustau, D., Manca, G., Matteucci, G., Miglietta, F., Ourcival, J. M., Papale, D., Pilegaard, K., Rambal, S., Seufert, G., Soussana, J. F., Sanz, M. J., Schulze, E. D., Vesala, T., and Valentini, R. (2005). Europe-wide reduction in primary productivity caused by the heat and drought in 2003. *Nature*, 437(7058):529–533.

Ciais, P., Tans, P. P., Trolier, M., White, J. W., and Francey, R. J. (1995a). A Large Northern Hemisphere Terrestrial CO_2 Sink Indicated by the $^{13}C/^{12}C$ Ratio of Atmospheric CO_2. *Science*, 269(5227):1098–1102.

Ciais, P., Tans, P. P., White, J. W., Trolier, M., Francey, R. J., Berry, J. A., Randall, D. R., Sellers, P. J., Collatz, J. G., and Schimel, D. S. (1995b). Partitioning of ocean and land uptake of CO_2 as inferred by $\delta^{13}C$ measurements from the NOAA Climate Monitoring and Diagnostics Laboratory Global Air Sampling Network. *Journal of Geophysical Research: Atmospheres*, 100(D3):5051–5070.

Ciattaglia, L. (1983). Interpretation of atmospheric CO_2 measurements at Mt. Cimone (Italy) related to wind data. *Journal of Geophysical Research: Oceans*, 88(C2):1331–1338.

Conway, T. J., Tans, P. P., Waterman, L. S., Thoning, K. W., Kitzis, D. R., Masarie, K. A., and Zhang, N. (1994). Evidence for interannual variability of the carbon cycle from the national oceanic and atmospheric administration/climate monitoring and diagnostics laboratory global air sampling network. *Journal of Geophysical Research: Atmospheres*, 99(D11):22831–22855.

Csavina, J., Roberti, J. A., Taylor, J. R., and Loescher, H. W. (2017). Traceable measurements and calibration: a primer on uncertainty analysis. *Ecosphere*, 8(2).

Dorling, S. R., Davies, T. D., and Pierce, C. E. (1992). Cluster analysis: A technique for estimating the synoptic meteorological controls on air and precipitation chemistry—results from eskdalemuir, south scotland. *Atmospheric Environment. Part A. General Topics*, 26(14):2583–2602.

Draxler, R. R. and Hess, G. (1998). An overview of the HYSPLIT 4 modelling system for trajectories. *Australian meteorological magazine*, 47(2):295–308.

Draxler, R. R. and Rolph, G. D. (2003). HYSPLIT (HYbrid Single-Particle Lagrangian Integrated Trajectory) Model, NOAA air Resources Laboratory: NOAA Air Resources Laboratory: Model access via NOAA ARL READY Webite http://ready.arl,noaa.gov/HYSPLIT.php.

EEA (2012). *Tracking progress towards Kyoto and 2020 targets*, volume no 6/2012 of *EEA report*. European Environment Agency, Copenhagen.

Farquhar, G. D., Ehleringer, J. R., and Hubick, K. T. (1989). Carbon isotope discrimination and photosynthesis. *Annual Review of Plant Physiology and Plant Molecular Biology*, 40(1):503–537.

Ferrarese, S., Apadula, F., Bertiglia, F., Cassardo, C., Ferrero, A., Fialdini, L., Francone, C., Heltai, D., Lanza, A., Longhetto, A., Manfrin, M., Richiardone, R., and Vannini, C. (2015). Inspection of high–concentration CO_2 events at the Plateau Rosa Alpine station. *Atmospheric Pollution Research*, 6(3):415–427.

Fleming, Z. L., Monks, P. S., and Manning, A. J. (2012). Review: Untangling the influence of air-mass history in interpreting observed atmospheric composition. *Atmospheric Research*, 104-105:1–39.

Forster, P., Ramaswamy, V., Artaxo, P., Berntsen, T., Betts, R., Fahey, D. W., Haywood, J., Lean, J., Lowe, D. C., Myhre, G., et al. (2007). Changes in atmospheric constituents and in radiative forcing. chapter 2. In *Climate Change 2007. The Physical Science Basis*.

Friedlingstein, P., Jones, M., O'sullivan, M., Andrew, R., Hauck, J., Peters, G., Peters, W., Pongratz, J., Sitch, S., Le Quéré, C., et al. (2019). Global carbon budget 2019. *Earth System Science Data*, 11(4):1783–1838.

Gardner, M. W. and Dorling, S. R. (2000). Meteorologically adjusted trends in uk daily maximum surface ozone concentrations. *Atmospheric Environment*, 34(2):171–176.

Gebhart, K. A., Schichtel, B. A., and Barna, M. G. (2005). Directional biases in back trajectories caused by model and input data. *Journal of the Air & Waste Management Association (1995)*, 55(11):1649–1662.

Ghasemifard, H., Ghada, W., Estrella, N., Lüpke, M., Oteros, J., Damialis, A., Traidl-Hoffmann, C., Buters, J., and Menzel, A. (2020). High post-season alnus pollen loads successfully identified as long-range transport of an alpine species. *Atmospheric Environment*, page 117453.

Ghasemifard, H., Vogel, F. R., Yuan, Y., Luepke, M., Chen, J., Ries, L., Leuchner, M., Schunk, C., Noreen Vardag, S., and Menzel, A. (2019a). Pollution Events at the High-Altitude Mountain Site Zugspitze-Schneefernerhaus (2670 m a.s.l.), Germany. *Atmosphere*, 10(6):330.

Ghasemifard, H., Yuan, Y., Luepke, M., Schunk, C., Chen, J., Ries, L., Leuchner, M., and Menzel, A. (2019b). Atmospheric CO_2 and $\delta^{13}C$ Measurements from 2012 to 2014 at the Environmental Research Station Schneefernerhaus, Germany: Technical Corrections, Temporal Variations and Trajectory Clustering. *Aerosol and Air Quality Research*, 19(3):657–670.

Ghashghaie, J. and Badeck, F. W. (2014). Opposite carbon isotope discrimination during dark respiration in leaves versus roots – a review. *New Phytologist*, 201(3):751–769.

GLOBALVIEW-CO2C13 (2009). Cooperative Atmospheric Data Integration Project - δ^{13}C of Carbon Dioxide. CD-ROM, NOAA ESRL, Boulder, Colorado: [Also available on Internet via anonymous FTP to aftp.cmdl.noaa.gov, Path: products/globalview/co2c13].

Greenwood, N. N. and Earnshaw, A. (2016). *Chemistry of the elements*. Elsevier-Butterworth Heinemann, Amsterdam, 2nd. ed., repr edition.

Hansen, A. D. A., Conway, T. J., Strele, L. P., Bodhaine, B. A., Thoning, K. W., Tans, P., and Novakov, T. (1989). Correlations among combustion effluent species at barrow, alaska: Aerosol black carbon, carbon dioxide, and methane. *Journal of Atmospheric Chemistry*, 9(1):283–299.

Hernández-Ceballos, M. A., Skjøth, C. A., García-Mozo, H., Bolívar, J. P., and Galán, C. (2014). Improvement in the accuracy of back trajectories using wrf to identify pollen sources in southern iberian peninsula. *International journal of biometeorology*, 58(10):2031–2043.

Hoffnagle, J. (2013). Relationship between spectroscopic measurements and delta values reported by the G1101-i isotopic carbon dioxide analyzers. *Picarro, Inc.*

Houghton, R. A. (2003). Revised estimates of the annual net flux of carbon to the atmosphere from changes in land use and land management 1850–2000. *Tellus B*, 55(2):378–390.

IPCC (2014). *Climate Change 2014: Synthesis Report. Contribution of Working Groups I, II and III to the Fifth Assessment Report of the Intergovernmental Panel on Climate Change, edition = [Core Writing Team, R.K. Pachauri and L.A. Meyer (eds.)]*. IPCC, Geneva, Switzerland.

IPCC (2018). *Global Warming of 1.5° C: An IPCC Special Report on the Impacts of Global Warming of 1.5° C Above Pre-industrial Levels and Related Global Greenhouse Gas Emission Pathways, in the Context of Strengthening the Global Response to the Threat of Climate Change, Sustainable Development, and Efforts to Eradicate Poverty*. in press, [Masson-Delmotte, V., P. Zhai, H.-O. Pörtner, D. Roberts, J. Skea, P.R. Shukla, A. Pirani, W. Moufouma-Okia, C. Péan, R. Pidcock, S. Connors, J.B.R. Matthews, Y. Chen, X. Zhou, M.I. Gomis, E. Lonnoy, T. Maycock, M. Tignor, and T. Waterfield (eds.)] edition.

Jung, J., Kim, Y. J., Lee, K. Y., Cayetano, M. G., Batmunkh, T., Koo, J.-H., and Kim, J. (2010). Spectral optical properties of long-range transport asian dust and pollution aerosols over northeast asia in 2007 and 2008. *Atmospheric Chemistry and Physics*, 10(12):5391–5408.

Kaiser, A., Scheifinger, H., Spangl, W., Weiss, A., Gilge, S., Fricke, W., Ries, L., Cemas, D., and Jesenovec, B. (2007). Transport of nitrogen oxides, carbon monoxide and ozone to the alpine global atmosphere watch stations jungfraujoch (switzerland), zugspitze and hohenpeissenberg (germany), sonnblick (austria) and mt. krvavec (slovenia). *Atmospheric Environment*, 41(40):9273–9287.

Keeling, C. D. (1958). The concentration and isotopic abundances of atmospheric carbon dioxide in rural areas. *Geochimica et Cosmochimica Acta*, 13(4):322–334.

Keeling, C. D. (1960). The concentration and isotopic abundances of carbon dioxide in the atmosphere. *Tellus*, 12(2):200–203.

Keeling, C. D. (1983). The global carbon cycle: What we know and could know from atmospheric, biospheric and oceanic observations. In *Proceedings: Carbon Dioxide Research Conference: Carbon Dioxide, Science and Consensus, CONF-820970. US Department of Energy, Washington, DC, pp. II*.

Kohn, M. J. (2010). Carbon isotope compositions of terrestrial C3 plants as indicators of (paleo)ecology and (paleo)climate. *Proceedings of the National Academy of Sciences*, 107(46):19691–19695.

Lan, L., Chen, J., Zhao, X., and Ghasemifard, H. (2019). VCSEL-Based atmospheric trace gas sensor using first harmonic detection. *IEEE Sensors Journal*, 19(13):4923–4931.

Lan, L., Ghasemifard, H., Yuan, Y., Hachinger, S., Zhao, X., Bhattacharjee, S., Bi, X., Bai, Y., Menzel, A., and Chen, J. (2020). Assessment of Urban CO_2 Measurement and Source Attribution in Munich Based on TDLAS-WMS and Trajectory Analysis. *Atmosphere*, 11(1):58.

Le Quéré, C., Andrew, R. M., Friedlingstein, P., Sitch, S., Hauck, J., Pongratz, J., Pickers, P. A., Korsbakken, J. I., Peters, G. P., Canadell, J. G., Arneth, A., Arora, V. K., Barbero, L., Bastos, A., Bopp, L., Chevallier, F., Chini, L. P., Ciais, P., Doney, S. C., Gkritzalis, T., Goll, D. S., Harris, I., Haverd, V., Hoffman, F. M., Hoppema, M., Houghton, R. A., Hurtt, G., Ilyina, T., Jain, A. K., Johannessen, T., Jones, C. D., Kato, E., Keeling, R. F., Goldewijk, K. K., Landschützer, P., Lefèvre, N., Lienert, S., Liu, Z., Lombardozzi, D., Metzl, N., Munro, D. R., Nabel, Julia E. M. S., Nakaoka, S.-i., Neill, C., Olsen, A., Ono, T., Patra, P., Peregon, A., Peters, W., Peylin, P., Pfeil, B., Pierrot, D., Poulter, B., Rehder, G., Resplandy, L., Robertson, E., Rocher, M., Rödenbeck, C., Schuster, U., Schwinger, J., Séférian, R., Skjelvan, I., Steinhoff, T., Sutton, A., Tans, P. P., Tian, H., Tilbrook, B., Tubiello, F. N., van der Laan-Luijkx, Ingrid T., van der Werf, Guido R., Viovy, N., Walker, A. P., Wiltshire, A. J., Wright, R., Zaehle, S., and Zheng, B. (2018). Global carbon budget 2018. *Oak Ridge National Lab. (ORNL), Oak Ridge, TN (United States)*, 10(4).

Lee, S., Akimoto, H., Nakane, H., Kurnosenko, S., and Kinjo, Y. (1998). Lower tropospheric ozone trend observed in 1989-1997 at okinawa, japan. *Geophysical Research Letters*, 25(10):1637–1640.

Locher, R., Ruckstuhl, A., et al. (2012). Idpmisc: Utilities of institute of data analyses and process design.

Lopez, M., Schmidt, M., Delmotte, M., Colomb, A., Gros, V., Janssen, C., Lehman, S. J., Mondelain, D., Perrussel, O., Ramonet, M., Xueref-Remy, I., and Bousquet, P. (2013). CO, NO_x and $^{13}CO_2$ as tracers for fossil fuel CO_2 : results from a pilot study in Paris during winter 2010. *Atmospheric Chemistry and Physics*, 13(15):7343–7358.

Makra, L., Sánta, T., Matyasovszky, I., Damialis, A., Karatzas, K., Bergmann, K.-C., and Vokou, D. (2010). Airborne pollen in three european cities: Detection of atmospheric circulation pathways by applying three-dimensional clustering of backward trajectories. *Journal of Geophysical Research: Atmospheres*, 115(D24):1.

Methven, J., Arnold, S. R., Stohl, A., Evans, M. J., Avery, M., Law, K., Lewis, A. C., Monks, P. S., Parrish, D. D., Reeves, C. E., Schlager, H., Atlas, E., Blake, D. R., Coe, H., Crosier, J., Flocke, F. M., Holloway, J. S., Hopkins, J. R., McQuaid, J., Purvis, R., Rappenglück, B., Singh, H. B., Watson, N. M., Whalley, L. K., and Williams, P. I. (2006). Establishing lagrangian connections between observations within air masses crossing the atlantic during the international consortium for atmospheric research on transport and transformation experiment. *Journal of Geophysical Research: Atmospheres*, 111(D23).

Miller, J. B. and Tans, P. P. (2003). Calculating isotopic fractionation from atmospheric measurements at various scales. *Tellus B*, 55(2):207–214.

Mook, W. G. (2000). *Environmental isotopes in the hydrological cycle: principles and applications*. Unesco.

Mook, W. G., Bommerson, J. C., and Staverman, W. H. (1974). Carbon isotope fractionation between dissolved bicarbonate and gaseous carbon dioxide. *Earth and Planetary Science Letters*, 22(2):169–176.

Mook, W. G., Koopmans, M., Carter, A. F., and Keeling, C. D. (1983). Seasonal, latitudinal, and secular variations in the abundance and isotopic ratios of atmospheric carbon dioxide: 1. results from land stations. *Journal of Geophysical Research: Oceans*, 88(C15):10915–10933.

Nakazawa, T., Morimoto, S., Aoki, S., and Tanaka, M. (1997). Temporal and spatial variations of the carbon isotopic ratio of atmospheric carbon dioxide in the western pacific region. *Journal of Geophysical Research: Atmospheres*, 102(D1):1271–1285.

Nara, H., Tanimoto, H., Tohjima, Y., Mukai, H., Nojiri, Y., Katsumata, K., and Rella, C. W. (2012). Effect of air composition (N_2, O_2, Ar, and H_2O) on CO_2 and CH_4 measurement by wavelength-scanned cavity ring-down spectroscopy: calibration and measurement strategy. *Atmospheric Measurement Techniques*, 5(11):2689–2701.

Newman, S., Xu, X., Gurney, K. R., Hsu, Y.-K., Li, K.-F., Jiang, X., Keeling, R., Feng, S., O&apos, Keefe, D., Patarasuk, R., Wong, K. W., Rao, P., Fischer, M. L., and Yung, Y. L. (2015). Toward consistency between bottom-up CO_2 emissions trends and top-down atmospheric measurements in the Los Angeles megacity. *Atmospheric Chemistry and Physics Discussions*, 15(20):29591–29638.

O'Keefe, A. and Deacon, D. A. G. (1998). Cavity ring–down optical spectrometer for absorption measurements using pulsed laser sources. *Review of Scientific Instruments*, 59(12):2544.

O'Leary, M. H. (1988). Carbon isotopes in photosynthesis. *BioScience*, 38(5):328–336.

Pang, J., Wen, X., Sun, X., and Huang, K. (2016). Intercomparison of two cavity ring-down spectroscopy analyzers for atmospheric $^{13}CO_2/^{12}CO_2$ measurement. *Atmospheric Measurement Techniques*, 9(8):3879–3891.

Park, R. and Epstein, S. (1960). Carbon isotope fractionation during photosynthesis. *California Inst. of Tech., Pasadena*, Vol: 21.

Pataki, D. E., Ehleringer, J. R., Flanagan, L. B., Yakir, D., Bowling, D. R., Still, C. J., Buchmann, N., Kaplan, J. O., and Berry, J. A. (2003). The application and interpretation of keeling plots in terrestrial carbon cycle research. *Global Biogeochemical Cycles*, 17(1).

Pataki, D. E., Xu, T., Luo, Y. Q., and Ehleringer, J. R. (2007). Inferring biogenic and anthropogenic carbon dioxide sources across an urban to rural gradient. *Oecologia*, 152(2):307–322.

Pfister, G., Pétron, G., Emmons, L. K., Gille, J. C., Edwards, D. P., Lamarque, J.-F., Attie, J.-L., Granier, C., and Novelli, P. C. (2004). Evaluation of CO simulations and the analysis of the CO budget for Europe. *Journal of Geophysical Research: Atmospheres*, 109(D19).

Picarro G1110-i datasheet (2008). Picarro G1110-i Isotopic CO_2 datasheet: Incredibly Simple Spectroscopy : Exceptionally Credible Data.

Popa, M. E., Vollmer, M. K., Jordan, A., Brand, W. A., Pathirana, S. L., and Rothe, M. (2014). Vehicle emissions of greenhouse gases and related tracers from a tunnel study: $CO:CO_2$, $N_2O:CO_2$, $CH_4:CO_2$, $O_2:CO_2$ ratios, and the stable isotopes ^{13}C and ^{18}O in CO_2 and CO. *Atmospheric Chemistry and Physics*, 14(4):2105.

Prevedouros, K., Brorström-Lundén, E., J. Halsall, C., Jones, K. C., Lee, R. G., and Sweetman, A. J. (2004). Seasonal and long-term trends in atmospheric pah concentrations: evidence and implications. *Environmental Pollution*, 128(1):17–27.

Ramsay, J., Heckman, N., and Silverman, B. (1997). Spline smoothing with model-based penalties. *Behavior Research Methods, Instruments, & Computers*, 29(1):99–106.

Rella, C. W. (2012). Accurate stable carbon isotope ratio measurements in humid gas streams using the Picarro $\delta^{13}CO_2$ G2101-i gas analyzer. *White Paper of Picarro Inc.*, pages 1–13.

Rella, C. W., Chen, H., Andrews, A. E., Filges, A., Gerbig, C., Hatakka, J., Karion, A., Miles, N. L., Richardson, S. J., Steinbacher, M., Sweeney, C., Wastine, B., and Zellweger,

C. (2013). High accuracy measurements of dry mole fractions of carbon dioxide and methane in humid air. *Atmospheric Measurement Techniques*, 6(3):837–860.

Seinfeld, J. H. and Pandis, S. N. (2016). *Atmospheric chemistry and physics: From air pollution to climate change*. Wiley, Hoboken (N.J.), 3 edition.

Sigmund, A., Freier, K., Rehm, T., Ries, L., Schunk, C., Menzel, A., and Thomas, C. K. (2019). Multivariate statistical air mass classification for the high-alpine observatory at the zugspitze mountain, germany. *Atmospheric Chemistry and Physics*, 19(19):12477–12494.

Šikoparija, B., Skjøth, C. A., Alm Kübler, K., Dahl, A., Sommer, J., Grewling, Ł., Radišić, P., and Smith, M. (2013). A mechanism for long distance transport of ambrosia pollen from the pannonian plain. *Agricultural and Forest Meteorology*, 180:112–117.

Sirois, A. and Bottenheim, J. W. (1995). Use of backward trajectories to interpret the 5-year record of PAN and O_3 ambient air concentrations at Kejimkujik National Park, Nova Scotia. *Journal of Geophysical Research*, 100(D2):2867.

Stein, A. F., Draxler, R. R., Rolph, G. D., Stunder, B. J. B., Cohen, M. D., and Ngan, F. (2015). NOAA's HYSPLIT Atmospheric Transport and Dispersion Modeling System. *Bulletin of the American Meteorological Society*, 96(12):2059–2077.

Stein, A. F., Isakov, V., Godowitch, J., and Draxler, R. R. (2007). A hybrid modeling approach to resolve pollutant concentrations in an urban area. *Atmospheric Environment*, 41(40):9410–9426.

Stohl, A. (1996). Trajectory statistics-a new method to establish source-receptor relationships of air pollutants and its application to the transport of particulate sulfate in europe. *Atmospheric Environment*, 30(4):579–587.

Stohl, A., Wotawa, G., Seibert, P., and Kromp-Kolb, H. (1995). Interpolation errors in wind fields as a function of spatial and temporal resolution and their impact on different types of kinematic trajectories. *Journal of Applied Meteorology*, 34(10):2149–2165.

Sturm, P., Leuenberger, M., and Schmidt, M. (2005). Atmospheric O_2, CO_2 and $\delta^{13}C$ observations from the remote sites Jungfraujoch, Switzerland, and Puy de Dôme, France. *Geophysical Research Letters*, 32(17).

Sturm, P., Tuzson, B., Henne, S., and Emmenegger, L. (2013). Tracking isotopic signatures of CO_2 at the high altitude site Jungfraujoch with laser spectroscopy: analytical improvements and representative results. *Atmospheric Measurement Techniques*, 6(7):1659–1671.

Tans and Keeling (2019). Pieter Tans, NOAA/ESRL (www.esrl.noaa.gov/gmd/ccgg/trends/) and Ralph Keeling, SIO (scrippsco2.ucsd.edu/).

Tuzson, B., Henne, S., Brunner, D., Steinbacher, M., Mohn, J., Buchmann, B., and Emmenegger, L. (2011). Continuous isotopic composition measurements of tropospheric CO_2 at Jungfraujoch (3580 m a.s.l.), Switzerland: real-time observation of regional pollution events. *Atmospheric Chemistry and Physics*, 11(4):1685–1696.

Uglietti, C., Leuenberger, M., and Brunner, D. (2011). European source and sink areas of CO_2 retrieved from Lagrangian transport model interpretation of combined O_2 and CO_2 measurements at the high alpine research station Jungfraujoch. *Atmospheric Chemistry and Physics*, 11(15):8017–8036.

United Framework Convention on Climate Change UNFCCC (2015). Historic Paris Agreement on Climate Change Press release, last access: 20.12.2019, https://unfccc.int/news/finale-cop21.

Vardag, S. N., Hammer, S., and Levin, I. (2016). Evaluation of 4 years of continuous $\delta^{13}C(CO_2)$ data using a moving Keeling plot method. *Biogeosciences*, 13(14):4237.

Vogel, F., Hamme, S., Steinhof, A., Kromer, B., and Levin, I. (2010). Implication of weekly and diurnal ^{14}C calibration on hourly estimates of CO-based fossil fuel CO_2 ata moderately polluted site in southwestern Germany. *Tellus B: Chemical and Physical Meteorology*, 62(5):512–520.

Vogel, F. R., Huang, L., Ernst, D., Giroux, L., Racki, S., and Worthy, D. E. J. (2013). Evaluation of a cavity ring-down spectrometer for in situ observations of $^{13}CO_2$. *Atmospheric Measurement Techniques*, 6(2):301–308.

Wahl, E. H., Fidric, B., Rella, C. W., Koulikov, S., Kharlamov, B., Tan, S., Kachanov, A. A., Richman, B. A., Crosson, E. R., Paldus, B. A., Kalaskar, S., and Bowling, D. R. (2006). Applications of cavity ring-down spectroscopy to high precision isotope ratio measurement of $^{13}C/^{12}C$ in carbon dioxide. *Isotopes in environmental and health studies*, 42(1):21–35.

Wang, Y. Q., Zhang, X. Y., and Draxler, R. R. (2009). Trajstat: Gis-based software that uses various trajectory statistical analysis methods to identify potential sources from long-term air pollution measurement data. *Environmental Modelling and Software*, 24(8):938–939.

Wen, X.-F., Meng, Y., Zhang, X.-Y., Sun, X.-M., and Lee, X. (2013). Evaluating calibration strategies for isotope ratio infrared spectroscopy for atmospheric $^{13}CO_2/^{12}CO_2$ measurement. *Atmospheric Measurement Techniques*, 6(6):1491–1501.

Wickham, H. (2011). ggplot2. *Wiley Interdisciplinary Reviews: Computational Statistics*, 3(2):180–185.

WMO (2016). *World Meteorological Organization; 18th session WMO/IAEA Meeting on Carbon Dioxide, Other Greenhouse Gases; Related Tracers Measurement Techniques, GAW*

Report, 229. 18th WMO: IAEA Meeting on Carbon Dioxide, Other Greenhouse Gases and Related Tracers Measurement Techniques (GGMT-2015). World Meteorological Organization (WMO), Geneva.

WMO (2018). *WMO Greenhouse Gas Bulletin (GHG Bulletin) - No. 14: The State of Greenhouse Gases in the Atmosphere Based on Global Observations through 2017*. World Meteorological Organization (WMO).

Worthy, D. E. J., Chan, E., Ishizawa, M., Chan, D., Poss, C., Dlugokencky, E. J., Maksyutov, S., and Levin, I. (2009). Decreasing anthropogenic methane emissions in europe and siberia inferred from continuous carbon dioxide and methane observations at alert, canada. *Journal of Geophysical Research*, 114(D10):419.

Yuan, Y., Ries, L., Petermeier, H., Steinbacher, M., Gómez-Peláez, A. J., Leuenberger, M. C., Schumacher, M., Trickl, T., Couret, C., Meinhardt, F., and Menzel, A. (2018). Adaptive selection of diurnal minimum variation: a statistical strategy to obtain representative atmospheric CO_2 data and its application to European elevated mountain stations. *Atmospheric Measurement Techniques*, 11(3):1501–1514.

Yuan, Y., Ries, L., Petermeier, H., Trickl, T., Leuchner, M., Couret, C., Sohmer, R., Meinhardt, F., and Menzel, A. (2019). On the diurnal, weekly, and seasonal cycles and annual trends in atmospheric CO_2 at Mount Zugspitze, Germany, during 1981–2016. *Atmospheric Chemistry and Physics*, 19(2):999–1012.

List of Figures

Acronyms

CO$_2$	carbon dioxide
δ^{13}**C**	carbon isotope ratio of CO$_2$
CO	carbon monoxide
CH$_4$	methane
GHG	greenhouse gas
PBL	Planetary boundary layer
WMO	World Meteorological Organization
GAW	Global Atmosphere Watch
NOAA	National Oceanic and Atmospheric Administration
IPCC	Intergovernmental Panel on Climate Change
HYSPLIT	Hybrid-Single Particle Lagrangian Integrated Trajectory
GDAS	Global Data Assimilation System
PSCF	Potential Source Contribution Function

Publication reprints

The next pages show reprints of the publications used in this thesis (see Sect. 4)
They can be found at page:

(i) 50
(ii) 64

No restrictions to reprint apply, since:

(i) Open access.
(ii) Open access.

Atmospheric CO_2 and $\delta^{13}C$ Measurements from 2012 to 2014 at the Environmental Research Station Schneefernerhaus, Germany: Technical Corrections, Temporal Variations and Trajectory Clustering

Homa Ghasemifard[1*], Ye Yuan[1], Marvin Luepke[1], Christian Schunk[1], Jia Chen[2,3], Ludwig Ries[4], Michael Leuchner[1†], Annette Menzel[1,3]

[1] *Professorship of Ecoclimatology, Technische Universität München, 85354 Freising, Germany*
[2] *Professorship of Environmental Sensing and Modeling, Technische Universität München, 80333 Munich, Germany*
[3] *Institute for Advanced Study, Technische Universität München, 85748 Garching, Germany*
[4] *German Environment Agency (UBA), 82475 Zugspitze, Germany*

ABSTRACT

This study presents continuous atmospheric CO_2 and $\delta^{13}C$ measurements by wavelength-scanned cavity ring down spectroscopy (Picarro G1101-i) at the high-mountain station Schneefernerhaus, Germany. $\delta^{13}C$ values were post-corrected for methane and water spectral interferences using accompanying measurements of CH_4 and H_2O, and CO_2 in dried air, respectively. The best precision of ±0.2‰ for $\delta^{13}C$ and of ±4 ppb for CO_2 was obtained with an integration time of about 1 hour for $\delta^{13}C$ and 2 hours for CO_2. The seasonality of CO_2 and $\delta^{13}C$ was studied by fitting background curves for a complete 2-year period. Peak-to-peak amplitudes of the averaged seasonal cycle were 15.5 ± 0.15 ppm for CO_2 and 1.97 ± 0.53‰ for $\delta^{13}C$, respectively. Based on the HYSPLIT Model, air masses were classified into five clusters, with westerly and northeasterly flows being the most and the least frequent, respectively. In the wintertime, northwest and northeast clusters had a higher median level for ΔCO_2 and a lower median level for $\Delta\delta^{13}C$ (the difference between observed and background concentrations), likely caused by anthropogenic emissions. In the summertime, air masses from the northwest had the lowest ΔCO_2 and the highest $\Delta\delta^{13}C$. Potential source contribution functions (PSCFs) were used to identify the potential source and sink areas. In winter, source areas for high CO_2 mixing ratios (> 75th percentile) were mainly located in northwestern Europe. In summer, areas with high $\delta^{13}C$ ratios (> 75th percentile), indicating a carbon sink, were observed in the air from Eastern and Central Poland.

Keywords: CO_2 mixing ratio; $\delta^{13}C$; Mountain station; Trajectory HYSPLIT; PSCF.

INTRODUCTION

The sources and sinks of atmospheric carbon dioxide (CO_2) play a critical role in governing global climate. Human activities, especially fossil fuel combustion, cement manufacturing and land use changes trigger anthropogenic emissions and thus contribute to a steady increase of the atmospheric CO_2 mixing ratio (IPCC, 2014; WMO, 2016; Xu *et al.*, 2017). Nearly half of the emitted CO_2 is taken up by both the terrestrial biosphere and absorption in the ocean reservoirs with a similar share each (Le Quéré *et al.*, 2016). The atmosphere and these two major sinks are linked via the balance between photosynthesis, respiration fluxes and CO_2 dissolving in ocean water (Ciais *et al.*, 2013). Considering the risk of the ocean sink to become saturated, the risk of the biosphere sink to turn into a source and of a consequential rapid increase in atmospheric CO_2 growth rates, it is crucial to monitor atmospheric CO_2 mixing ratio continuously with high temporal resolution in order to identify the source and sink contributions (Cramer *et al.*, 2001; IPCC, 2013).

The stable carbon isotope composition of CO_2 ($\delta^{13}C$) allows distinguishing the exchange of fossil carbon from the atmosphere and surface reservoir fluxes (Keeling *et al.*, 2011). During photosynthesis, most plants of the terrestrial biosphere prefer to take up the light isotopologue $^{12}CO_2$ and thus discriminate against $^{13}CO_2$ (~18‰) (Farquhar *et al.*, 1989). In contrast, during oceanic uptake of CO_2, there is almost no discrimination (~2‰) (Mook *et al.*, 1974). Since the discrimination by oceans is small, the carbon

---

[†] Now at Springer Nature B.V., Dordrecht, 3311 GX, Netherlands

[*] Corresponding author.
 Tel.: +49-89-28923358; Fax: +49-8161-714753
 E-mail address: homa.ghasemifard@wzw.tum.de

isotope signature ($\delta^{13}C$) can be applied to study the contribution of the biosphere on carbon cycles in the atmosphere (Keeling *et al.*, 1989; Miller *et al.*, 2003).

Atmospheric CO_2 and $\delta^{13}C$ have been studied on both regional and global scales at different sites with various techniques (Levin *et al.*, 1995; Tuzson *et al.*, 2011; Sturm *et al.*, 2013; Moore and Jacobson, 2015; Xia *et al.*, 2015; Pang *et al.*, 2016a). For instance, Xia *et al.* (2015) analyzed measurements of atmospheric CO_2 concentration and its stable isotope ratios ($\delta^{13}C$) at the regional background station Lin'an (LAN) in China to identify the isotopic signature of CO_2 sinks and sources. They concluded that during the winter season (Dec–Feb) coal combustion is the major CO_2 source due to domestic heating. The relatively high isotopic signature (~21.32‰) of sources and sinks during the vegetation season (Mar–Nov) was attributed to the significant contribution of biological activities at LAN. Sturm *et al.* (2013) presented continuous measurements of atmospheric CO_2 isotopes ($\delta^{13}C$ and $\delta^{18}O$) at the High Altitude Research Station Jungfraujoch (JFJ), Switzerland. Based on the high temporal resolution of their measurements (e.g., in comparison to flask samples), diurnal and hourly variations could be analyzed. They determined that diurnal cycles of atmospheric CO_2 and its isotopic compositions were small; however, the day-to-day variability depending on the origin of the air masses arriving at JFJ was larger. Based on this, the footprint clustering by the backward Lagrangian particle dispersion model FLEXPART revealed different CO_2, $\delta^{13}C$, and $\delta^{18}O$ values depending on the origin of air masses and surface residence time. Moore and Jacobson (2015) differentiated sources of atmospheric CO_2 by records of CO_2 concentration and carbon isotope composition ($\delta^{13}C$) at Evanston, an urban site north of Chicago, the third largest city in the United States.

Measurements of CO_2 mixing ratios in combination with stable CO_2 isotopes in the atmosphere at high altitude (background) sites may provide valuable information on carbon source and sink mechanisms (Zhou *et al.*, 2006; Sturm *et al.*, 2013; Yuan *et al.*, 2018). The variability of the atmospheric CO_2 mixing ratio and $\delta^{13}C$ is related to the history of air masses arriving at a measurement site, such as whether the air traveled through the free troposphere or has been influenced by the planetary boundary layer (PBL). Therefore, many atmospheric studies have applied trajectory statistical methods to identify the sources and their contribution to mixing ratios. Fleming *et al.* (2012) reviewed more than 150 studies dealing with back trajectories, cluster analyses and residence time. However, most of them applied air-mass history to identify transport pathways and potential sources but not sink contributions. It is well known that the effect of biospherical activity as well as strong influences of thermal convection (local transport processes from the boundary layer) may complicate the study of atmospheric CO_2 and $\delta^{13}C$ (Zellweger *et al.*, 2003; Sturm *et al.*, 2013).

In the present study, we (1) describe the specific corrections and selections of the data recorded by a non-upgraded G1101-i analyzer, (2) analyze the diurnal and seasonal patterns of atmospheric CO_2 mixing ratios and

$\delta^{13}C$ and (3) identify potential CO_2 source and sink locations with the help of backward trajectories and the potential source contribution function.

MATERIAL AND METHODS

Measurement Site

The Environmental Research Station Schneefernerhaus (UFS) is part of the Global Atmosphere Watch (GAW) Global Observatory Zugspitze/Hohenpeissenberg in Germany. It is located in the northern limestone Alps at the border of Germany and Austria (47°25′00″N, 10°58′46″E) about 90 km southwest of Munich. The UFS is situated at an altitude of 2650 m above sea level (a.s.l.) on the southern slope of Zugspitze mountain massif. It can receive representative free tropospheric air but is also influenced by polluted air masses from the planetary boundary layer (PBL), especially during the day and in summer (Zellweger *et al.*, 2003; Pandey Deolal *et al.*, 2014; Leuchner *et al.*, 2016). Due to its location on a southern slope, northerly winds are mostly blocked (see Fig. 1) while there is wind channeling of western and eastern winds by the west side of the mountain ridge and the Rein Valley, respectively (Gantner *et al.*, 2003; Risius *et al.*, 2015). Due to diverse and intensive human activities in the vicinity of the UFS, from skiing and hiking areas as well as associated tourist services, the GAW site is categorized as a "weakly influenced, constant deposition" site (Henne *et al.*, 2010; Ferrarese *et al.*, 2015). Further detailed information can be found in the UFS station information system (http://www.schneefernerhaus. de/en/home.html).

Instrumentation

A wavelength-scanned cavity ring down spectrometer (G1101-i, Picarro Inc. USA) was installed in the laboratory on the 4th floor of the UFS building. It was operated from May 2012 to November 2014 (except for a downtime period in May and June 2013 due to a pump defect and its subsequent replacement). CO_2 mixing ratios and $\delta^{13}C$ were measured at a rate of 0.1 Hz. The air inlet for the instrument was located on a terrace above the laboratory roof at an altitude of 2670 m a.s.l. The inlet cap was constantly heated to prevent ice formation. The inner part of the inlet tube was made of borosilicate glass and was constantly regulated to a low positive temperature of ca. 5°C to avoid water condensation. The inlet tube (length: 3.5 m) was connected to a common manifold (glass, 4.2 m in length, 8 cm inner diameter) that was used for all measuring devices and species at the GAW station (Zellweger *et al.*, 2011). A 2 m 1/8″ stainless steel pipe connected the instrument to the inlet line, via a VICI (Valco Instruments Company Inc.) rotary valve that switched between ambient air and standard gases.

Isotopic ratio measurements of $^{13}C/^{12}C$ are expressed in per mil (‰), defined by the following Eq. (1) as:

$$\delta^{13}C = \left(\frac{\left(^{13}C / ^{12}C \right)_{sample} - \left(^{13}C / ^{12}C \right)_{standard}}{\left(^{13}C / ^{12}C \right)_{standard}} \right) \times 1000 \qquad (1)$$
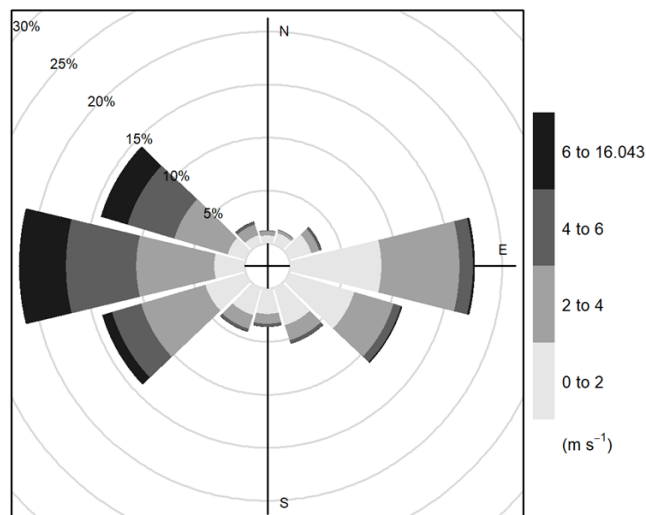
Fig. 1. Windrose at UFS, obtained from hourly wind data over the entire study period (May 2012–November 2014). Wind speed and direction are classified into colored segments; gray circles show the cumulated percentage of occurrence.

Isotopic values were given relative to the international standard VPDB-CO_2 (Vienna Pee Dee Belemnite) (Brand *et al.*, 2010). Measurements of CO_2 and $\delta^{13}C$ were calibrated using two working standard gases with high and low concentrations (DEUSTE Steininger GmbH) of the certified CO_2 mixing ratios and the isotopic compositions (Standard 1: 350.1 ± 0.50 ppm CO_2 mixing ratio and –3.28 ± 0.164‰ $\delta^{13}C$; Standard 2: 503.4 ± 0.50 ppm CO_2 mixing ratio and –20.03 ± 1.002‰ $\delta^{13}C$) in synthetic air. Each standard gas was fed into the analyzer for one hour every 7 days using an open-split configuration. After the data collection period, both gas standards were reanalyzed at the laboratory of the Max Planck Institute for Biogeochemistry (MPI-BGC), Jena, Germany, in order to confirm the quality of the calibration and the stability of the standards. The measured $\delta^{13}C$ values (Standard 1: –3.19 ± 0.009‰ $\delta^{13}C$; Standard 2: –20.26 ± 0.01‰ $\delta^{13}C$) agreed well with the original values within the given range of GAW data quality objectives (±0.01‰). The standard gases were also analyzed for other trace gas concentrations. Except for N_2O (Standard 1 and 2: 0.1 ppm) and CO (Standard 1: 6 ppb; Standard 2: 5.47 ppb), no other species (CH_4, H_2O, SF_6) could be detected.

The German Meteorological Service (Deutscher Wetterdienst, DWD) provided wind speed and wind direction data from the UFS in a one-minute time interval, and for this study, hourly averaged data are presented. In addition, we used CO_2 and CH_4 data measured with a Picarro Envirosense 3000i instrument to correct our measured data (see the section "Correction of CO_2"). This instrument, using cavity ring down spectroscopy, was operated by the German Environment Agency (Umweltbundesamt, UBA) connected to the same inlet as our Picarro G1101-i, therefore measured identical air sample, and was operated in the same air conditioned laboratory. For this device,

water vapor in the ambient air was removed by cold traps. Gas mixtures for working standards of this device were equally delivered by DEUSTE Steininger GmbH, Germany. The station standards for interconnection with the international standard reference were reported on WMO X-2007 scale for CO_2 and WMO X2004a scale for CH_4 by NOAA, Boulder, Colorado, USA. Calibration and quality assurance for these atmospheric compounds followed the standard operating procedures of UBA in accordance with GAW quality standards. Since CO_2 measurements from UBA are reported to the WMO World Data Centre for Greenhouse Gases, the respective CO_2 data in the section "Correction of CO_2" will be referred to as CO_2 data of Global Atmosphere Watch ($CO_{2,\ GAW}$).

Optimal Integration Time and Precision

The Allan variance method (Allan, 1966; Werle *et al.*, 1993; Chen *et al.*, 2016) was applied to determine the optimal integration time for the measurements and to determine the best precision, using Standard 1 (CO_2: 350.1 ± 0.50 ppm; $\delta^{13}C$: –3.28 ± 0.164‰; Fig. 2). For this purpose, a long-term measurement of 24 h duration in February 2014 was analyzed. When integrating less than the optimum integration time, the Allan deviation follows a slope of –1/2 in the double logarithmic scale, indicating that white noise is dominating. When integrating beyond the optimum integration time, the Allan deviation rises and follows a slope of 1/2, indicating an instrument drift.

The optimum integration time minimizing the Allan deviation was around 1 hour for CO_2 and around 2 hours for $\delta^{13}C$. The best achievable precision (1 sigma) was 4 ppb for CO_2 and 0.2‰ for $\delta^{13}C$, respectively (see Fig. 2). However, we used a shorter integration time of 30 minutes for the ambient measurements, which gave a precision of
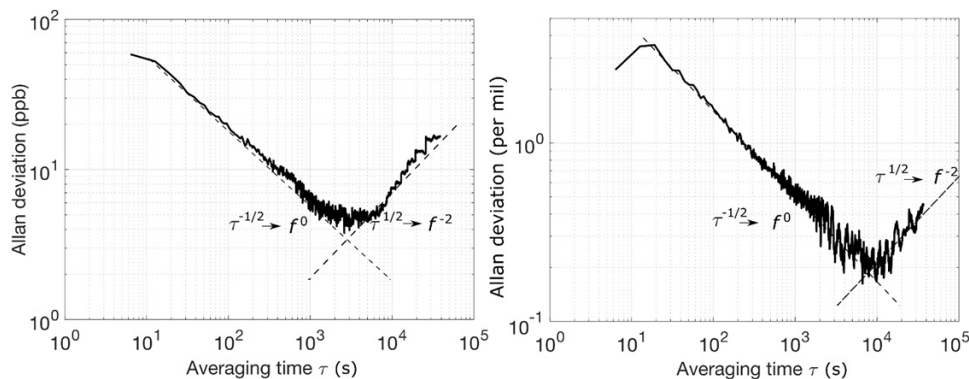
Fig. 2. Allan deviation plots for CO_2 (left) and $\delta^{13}C$ (right) as a function of the integrating time τ, based on a long-term measurement of Standard 1 (CO_2: 350.1 ± 0.50 ppm; $\delta^{13}C$: 3.28 ± 0.164‰). f stands for frequency and the black dashed lines represent slopes of –1/2 and 1/2, which correspond to power spectral densities $S(f) = f^0$ and $S(f)= f^2$, respectively. The Allan deviation follows a slope of –1/2 up to an integration time of 1 hour for CO_2 and of 2 hours for $\delta^{13}C$ and then turns over to a slope of 1/2 which defines a drift.

0.4‰ for $\delta^{13}C$ and 5–6 ppb for CO_2. For the very same analyzer, Wen *et al.* (2013) found the best precision of 0.08‰ at 2000 s, Vogel *et al.* (2013) had a precision of 0.2‰ at 5 min averaging, and Pang *et al.* (2016b) achieved optimum values of 0.08, 0.15, and 0.10‰ at 7600, 1900, and 1900 s for three reference gases. The precision of all studies on Picarro G1101-i shows better precision than the specification provided by the manufacturer (0.3‰).

Data Calibration and Correction

The G1101-i analyzer in this study was manufactured in 2010 and not upgraded during the measurement period to minimize downtime. As an alternative to upgrading, Picarro Inc. recommended later removal of spectral interference caused by CH_4 that can bias $\delta^{13}C$ by 0.4‰ ppm^{-1} (Vogel *et al.*, 2013) as well as water interferences. The latter include water vapor dilution, water vapor pressure broadening, and HDO spectral interference effects (Wen *et al.*, 2013). As we did not use any drying system and therefore measured the humid ambient gas, corrections for the dominating water vapor dilution effect were done according to Hoffnagle (2013); however, the smaller effects due to the water vapor pressure broadening and the HDO spectral interference effects were not corrected and their effects are about 2 ppm %v^{-1} water at 400 ppm of carbon dioxide, and up to 5‰ at ambient humidity (Nara *et al.*, 2012; Rella *et al.*, 2013; Wen *et al.*, 2013). According to Wen *et al.* (2013), even an upgrade of the analyzer would have led to overcorrections. The dependency of $\delta^{13}C$ on the CO_2 mixing ratio is of no concern to this study, as Vogel *et al.* (2013) showed that no dependency could be detected in the range of 303–437 ppm. Background gas concentrations and ratios (e.g., N_2/O_2 ratio and argon content) are known to influence the CRDS technology in general. While their natural variations usually generate negligible effects, large differences between ambient air and synthetic standards, such as the ones used in our study, may be problematic

(Nara *et al.*, 2012; Rella *et al.*, 2013). However, no specific information or corrections are documented for the G1101-i analyzer.

Correction of $\delta^{13}C$

The isotopic analyzer reports the peak height of the near-infrared absorption spectrum for the rovibronic transition of $^{12}C^{16}O_2$ and $^{13}C^{16}O_2$ with arbitrary labeled $C12_{peak\text{-}BookAve}$ and $C13_{peak\text{-}BookAve}$, respectively. The ratio of the peak absorption values and the ratio of isotopic abundances are linear.

$$\delta\left(\frac{^{13}C}{^{12}C}\right) (\text{in permil}) = A\left(\frac{C13_{peak-BookAve}}{C12_{peak-BookAve}}\right) + B \quad (2)$$

A and B are instrument-specific constants and were provided by the manufacturer; they are the linear slope and intercept terms for computing the delta value from the ratio between $C13_{peak\text{-}BookAve}$ and $C12_{peak\text{-}BookAve}$ (Hoffnagle, 2013). The peak height can be affected by the absorption peaks for water, methane and other gases (Nara *et al.*, 2012; Rella *et al.*, 2013).

$\delta^{13}C$ ratios were corrected for methane and water vapor according to Hoffnagle (2013) using Eq. (3):

$$\delta^{13}C_{calculated} = A \times \left(\frac{C13_{peak-BookAve} - 0.003728 \times CH_4}{C12_{peak-BookAve}}\right) + B + \left(-2.98648648 \times H_2O\right) \quad (3)$$

H_2O is the water vapor concentration (in percent) and $(-2.98648648 \times H_2O)$ is the correction for the water interference. CH_4 is the methane concentration (in ppm), measured by the UBA device (Picarro Envirosense 3000i instrument).

Correction of CO₂

To quantify and correct water vapor effects on the CO_2 measurements, we compared the CO_2 mixing ratio for the wet gas stream measured by Picarro G1101-i analyzer ($CO_{2,meas}$) with CO_2 data of the accompanying instrument ($CO_{2,GAW}$). Although similar seasonal cycles were observed in Fig. 3, $CO_{2,meas}$ mixing ratios only showed a good agreement with $CO_{2,GAW}$ in wintertime when water vapor concentrations were low ($0.39 \pm 0.004\%$), while clear differences were observed in the summertime when water vapor concentrations were higher ($1.81 \pm 0.0048\%$). Wen *et al.* (2013) also measured a wet gas stream and compared the same analyzer as in this study with the Los Gatos DLT-100, observing that the mixing ratio measured by Picarro G1101-i was 2.2 ± 1.0 ppm lower than Los Gatos. They suggested that the water vapor dilution effect was partly responsible for this difference.

We corrected the dilution effect using ordinary least squares regression of the CO_2 mixing ratio difference between $CO_{2,GAW}$ and $CO_{2,meas}$. Concurrent with a pump failure and subsequent replacement (end of May/beginning of June 2013), the extent of the dilution effect changed and thus OLS regressions were carried out separately for the period before (Eq. (4)) and after (Eq. (5)) the pump failure, yielding

$$[CO_2]_{calculated} = 6.5[H_2O] - 2.7 + [CO_2]_{meas} \qquad (4)$$

$$[CO_2]_{calculated} = 5.6[H_2O] - 0.85 + [CO_2]_{meas} \qquad (5)$$

where $[H_2O]$ is water vapor concentration in percent, $[CO_2]_{meas}$ is CO_2 mixing ratio measured by our analyzer and $[CO_2]_{calculated}$ is the calculated and corrected mixing ratio. Fig. 4 illustrates the regressions before and after the pump failure. The physical reasons for the change in G1101-i behavior are not known and it seems unlikely that they were caused by the pump failure and replacement alone.

Corrected CO_2 data thus is in accordance with GAW data quality objectives (± 0.1 ppm) (WMO, 2016). However, very small differences between the two analyzers (0.01 ± 0.42 and 0.02 ± 0.06 ppm before and after the pump replacement, respectively) remain and may be due to biases from spectral broadening and interferences (Rella, 2012).

Data Coverage and Selection

The temporal resolution of CRDS raw data should be in the order of seconds. In our case, however, the data periodically included measuring intervals far beyond the normal range (55 s and more). Since long measuring intervals are indicative of a slowed ring-down frequency and potential problems with the instrument (such as laser ageing or deficiencies in the optics, detector or data acquisition system), intervals > 55 s duration were removed from the dataset (personal communication by Dr. Renato Winkler, Picarro Inc.), which amounted to about 4.6% of data. The device returned to normal measuring intervals after restarts or laser readjustments. 1.8% of the data were missing due to the pump defect and replacement in May and June 2013. Another 3.8% of the data were missing due to the calibration procedures and/or power failures in the lab. At the end, this resulted in 89.8% of valid data over the entire measuring period.

The first 29 measurements of each calibration (ca. 3.5 minutes, less than 6% of each calibration) were discarded to ensure that no air sample from the previous measurement was left due to the transient response after valve switching (Vogel *et al.*, 2013). Then, from the remaining data, the average of each calibration was calculated. A smoothing spline was then fitted to all the averages to account for the residual variation in the calibration data and to fill a gap in the calibration measurements (8 months, July 2012–March 2013). This reduced the residual deviation between calibrated standard measurement and the real standard value from $0.05 \pm 0.75‰$ and $0.03 \pm 0.53‰$ (linear interpolation) to $0.0 \pm 0.44‰$ and $0.0 \pm 0.32‰$ (smoothing spline) for
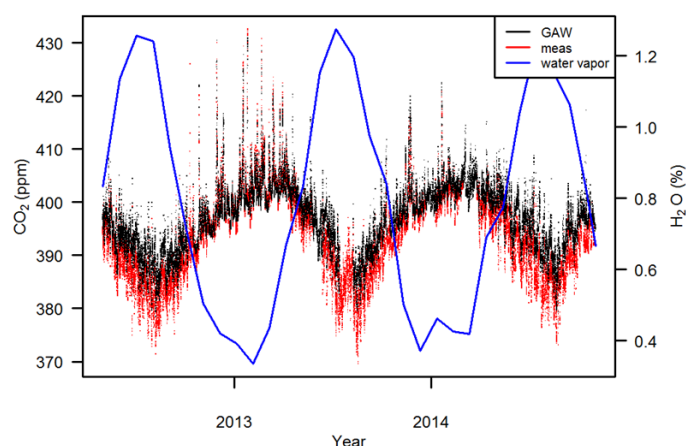

Fig. 3. Comparison of CO_2 mixing ratio measured by Picarro G1101-i (in red) without drying system to CO_2 measured by Picarro Envirosense 3000i (in black) dried by cold traps.
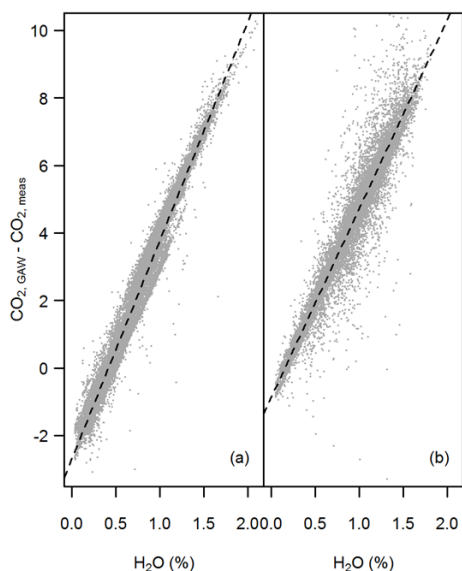
Fig. 4. Scatterplot of water vapor concentrations and difference of GAW and Picarro CO_2 measurements in the two phases before (a) and after (b) the pump replacement. The dashed line is an ordinary least squares regression line (coefficient of determination of linear regressions in (a): R^2 = 0.97, p-value < 0.001 and (b): R^2 = 0.92, p-value < 0.001).

Standards 1 and 2, respectively. Splines were calculated using the sm.spline function from the pspline package in R

(Heckman and Ramsay, 1996). This function fitted a natural polynomial smoothing spline to the calibration values with 25 degree of freedom (out of 108 calibrations). Deviations between spline interpolated calibrations and the real standard values for each calibration are shown in Fig. 5. The smoothed coefficients were used for calibration. The two-point mixing ratio gain and offset calibration strategy of Bowling *et al.* (2003) was used for each measurement cycle as described above. Data were aggregated to 30-min averages by the statistical program *R* (R Core Team, 2016), which together with several packages was used for further analyses. At the end, uncertainty of calibration is estimated to be ±0.56 ppm for CO_2 and ±0.53‰ for $\delta^{13}C$ and combined measurement uncertainty is estimated to be ±0.56 ppm for CO_2 and ±0.56‰ for $\delta^{13}C$.

HYSPLIT Trajectory Model

One common method to establish source/sink-receptor relationships is to combine a calculated trajectory path of an air parcel with measured data at the time when the air parcel arrives at the site and consequently to determine locations of sources and sinks from these observations (Stohl, 1996).

In this work, the HYSPLIT (Hybrid Single-Particle Lagrangian Integrated Trajectory) Model was used to calculate backward trajectories to estimate air mass pathways to the UFS. Trajectories were calculated hourly for 96 h backward ending at UFS for the whole measurement period. The backward trajectory calculation was started at an altitude of 1500 m above ground level (a.g.l.) with respect to the model elevation at the coordinates of UFS, thus 3000 m a.s.l., roughly matching the real site altitude of 2650 m a.s.l. (UFS) and 2670 m a.s.l. (sample inlet).
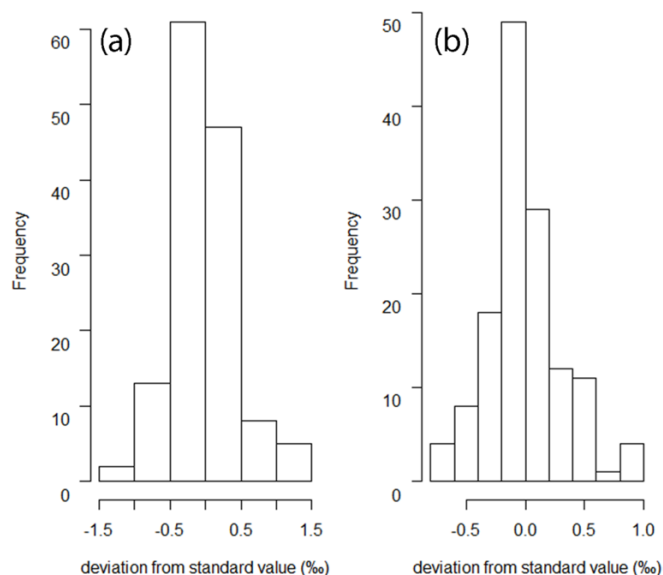

Fig. 5. Histogram of the deviation between spline and true standard value for (a) Standard 1 and (b) Standard 2.

663

The GFS (Global Forecast System) model "Grid 4" forecast weather data with 0.5° resolution was used as an underlying meteorological model. Forecasts from the 18:00 UTC cycle were obtained from the NOAA HAS data portal each day for the next 24 hours and were converted to ARL input model format. In case of the very few gaps (around 1.2%) in the GFS forecast data, forecasts from the previous day(s) were used as a replacement. For each trajectory time step, coordinates, altitude and mixing layer height (from the input model) were extracted. The backward trajectories were further processed by the openair package (Carslaw and Ropkins, 2012) within *R*. Here, clusters were calculated from all trajectories by applying an angle-based distance matrix method with the k-medoids algorithm (Sirois and Bottenheim, 1995). The number of clusters was set to five since for this number at least 10% of the trajectories were represented within each cluster. In order to filter the trajectories concerning their background air characteristics, they were split into two classes: (1) FT (free troposphere) trajectories when the trajectory height was higher than the mixing layer height for all time steps and (2) PBL influenced trajectories when the trajectory was below the calculated mixing layer height for at least one time step.

The potential source contribution function (PSCF) method using the residence time probability (Ashbaugh *et al.*, 1985; Seinfeld and Pandis, 2016) describes the spatial distribution of probable geographical source locations derived by trajectories. PSCF is defined as the probability that an air parcel with atmospheric component concentrations higher than a specific threshold arrives at the receptor site after having been observed to reside in a certain grid cell. The PSCF value (P_{ij}) for a given grid cell is then calculated as $P_{ij} = m_{ij}/n_{ij}$, in which n_{ij} is the total number of trajectory segment endpoints terminating within the grid cell(i,j) over the entire time of measurement and m_{ij} is the number of trajectory segment endpoints terminating within the grid cell(i,j) corresponding to trajectories associated with concentration values at the receptor site greater than a specific threshold (75th percentile of CO_2 and $\delta^{13}C$ in this study).

Robust Extraction of Baseline Signal

In order to calculate the long-term background values, the statistical method REBS (Robust Extraction of Baseline Signal) was applied, which is based on robust local regression (Ruckstuhl *et al.*, 2012). REBS is very flexible to derive the background levels of various trace gases at background measurement sites simultaneously (in our case both CO_2 and $\delta^{13}C$) due to its non-parametric basis. Sturm *et al.* (2013) used REBS for high alpine CO_2 and $\delta^{13}C$ measurements at Jungfraujoch, with results very similar to those obtained from the commonly applied data filtering method by Thoning *et al.* (1989). The background concentration was extracted using local regression (60 day windows) implemented in the rfbaseline function of the IDPmisc package (Locher and Ruckstuhl, 2012) in *R*. Missing data points were interpolated by a simple linear interpolation using the values from the hours before and after. The mean peak-to-peak seasonal amplitude was

calculated from the background curves for an entire 2-year period (2012–2014).

Remote Sensing Data

In order to assess the vegetation properties, information on the vegetation type and activity in summer (June–August) were required. Therefore, we used remotely sensed phenological data based on MODIS Land Cover (LC) data and the Normalized Difference Vegetation Index (NDVI), respectively. The latest LC was issued in 2012 at 0.5° × 0.5° resolution (Friedl *et al.*, 2010; Channan *et al.*, 2014). More information can be found in the Global Land Cover Facility (http://glcf.umd.edu/data/lc/). The LC classes were aggregated to the ones shown and described in Fig. 11(b). NDVI is derived from multiple Advanced Very High Resolution Radiometer (AVHRR) measurements and is an indicator of the greenness of vegetation in each pixel of the satellite image. It ranges from –1.0 to +1.0. NDVI values below zero are excluded from this study because they indicate no vegetation, such as rock, sand or snow. Sparse vegetation such as grassland or cropland results in moderate NDVI values (0.2–0.5) and dense vegetation such as tropical forests results in high NDVI values (0.6–0.9). In this study, we averaged the respective NDVI values for the three months of summer (June to August) in the year 2012. The NDVI data were downloaded from the ECOCAST directory of the NASA Ames Ecological Forecasting Lab, version 3g.v0 (https://ecocast.arc.nasa.gov/data/pub/gimms/3g.v0/) for 2012.

RESULTS AND DISCUSSION

Atmospheric CO_2 and $\delta^{13}C$

Time series of CO_2 mixing ratios and $\delta^{13}C$ recorded from May 1, 2012, to Nov. 2, 2014, are displayed in Fig. 6. This includes both hourly data and fitted background concentrations, using the REBS technique. Fig. 6 shows a clear seasonal variation of hourly mean CO_2 mixing ratios and $\delta^{13}C$ values. CO_2 mixing ratios simultaneously increase as $\delta^{13}C$ values decrease, which is associated with seasonal vegetation activity. The mean peak-to-peak amplitudes are 15.5 ± 0.15 ppm for CO_2 and 1.97 ± 0.53‰ for $\delta^{13}C$. The minimum CO_2 mixing ratios, as well as the maximum $\delta^{13}C$ values, occurred in August due to (preferentially $^{12}CO_2$) CO_2 terrestrial uptake being dominated by the biosphere. The maximum in CO_2 mixing ratios occurred in March and the minimum in $\delta^{13}C$ values in February when respiration is dominating. In contrast, the peak-to-peak amplitudes of CO_2 mixing ratios and $\delta^{13}C$ at the High Altitude Research Station Jungfraujoch (JFJ) on the northern ridge of the Swiss Alps (46°32′53″N, 7°59′2″E, 3580 m a.s.l.) are 11.0 ppm for CO_2 and 0.60‰ for $\delta^{13}C$ (Sturm *et al.*, 2013). These differences in seasonal amplitudes between UFS and JFJ are most likely due to altitude since JFJ is located 930 m higher than UFS. Consequently, air masses at JFJ are much less impacted by PBL and mostly are from the lower free troposphere. Although amplitudes of CO_2 mixing ratios and $\delta^{13}C$ from these two sites were different, the minimum and the maximum of CO_2 mixing ratios and $\delta^{13}C$ were recorded nearly at the same time of the year.
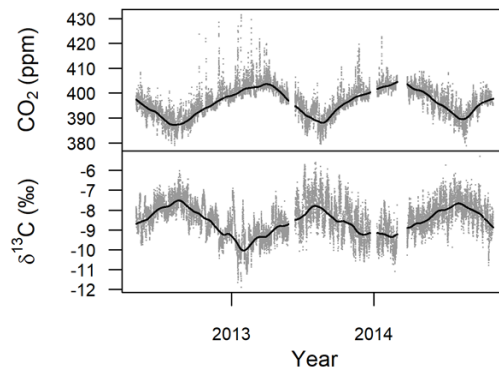
Fig. 6. Time series of hourly mean values of CO_2 and $\delta^{13}C$ for the period May 2012 to November 2014. Gray dots and solid lines represent the measurements and fitted background curves, respectively.

Diurnal Cycles

The mean diurnal cycles of CO_2 and $\delta^{13}C$ for each season are shown in Fig. 7. The CO_2 level started to increase at about 06:00 and reached the maxima around 09:00 to 10:00 during spring, summer, and autumn and at around 13:00 during winter, possibly due to local tourist activity, regional respiration, and regional anthropogenic emission potentially due to traffic. The daily peak-to-peak amplitude is 1.4 ppm in winter and 1.6 ppm in spring and autumn. The maximal diurnal change in CO_2 is found during summer months with a peak-to-peak amplitude of about 2.9 ppm. The strong afternoon drop during summer months is due to upward transport of PBL air from the valley. In summer, the CO_2 of the PBL air in lower levels is depleted due to photosynthetic uptake, indicating the influence of vegetation activity in the lower local and regional area around (below)

the UFS. During summertime, the PBL influence at UFS has been identified for other parameters as well. Namely, the diurnal variation and high standard deviation of formaldehyde (HCHO) mixing ratio (Leuchner *et al.*, 2016) and the dependency of aerosol concentrations from the altitude of the mixing layer (Birmili *et al.*, 2009) could be detected. The mean diurnal cycle of $\delta^{13}C$ is very pronounced in summer with an amplitude of 0.4‰. The respective diurnal amplitudes in spring and autumn are 0.2‰ each, showing similar patterns as in summer. In contrast, winter months do not display any distinct diurnal cycles of $\delta^{13}C$.

For the Swiss site Jungfraujoch (JFJ), similar start of increase and maxima have been observed in spring, summer and autumn. However, amplitudes of diurnal variations in CO_2 mixing ratios and $\delta^{13}C$ were different (Sturm *et al.*, 2013). The diurnal peak-to-peak amplitude of CO_2 at JFJ
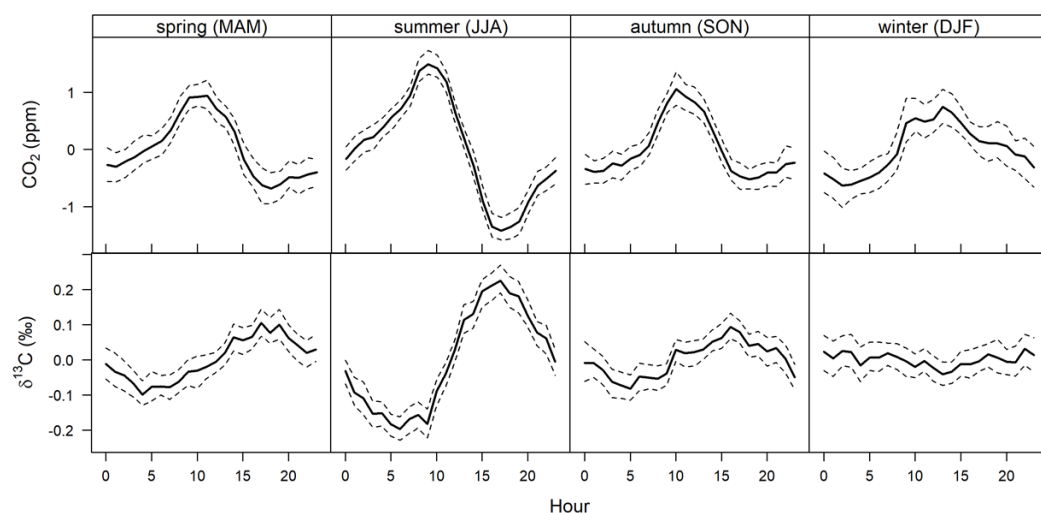

Fig. 7. Diurnal variations of the mean hourly CO_2 mixing ratios and $\delta^{13}C$ (solid line) relative to the respective daily means for the different seasons. Dashed lines show the 95% confidence intervals of the hourly mean calculated by bootstrap re-sampling.

in summer was 2 ppm (0.9 ppm less than at the UFS) and was 1 ppm in the other seasons (0.6 ppm less than at UFS in spring and autumn and 0.4 less in winter). In contrast to UFS, there were almost no diurnal variations of δ^{13}C at JFJ in spring, autumn and winter. In summer, JFJ exhibited a diurnal variation of about 0.3‰ less than at UFS with a comparable minimum in the morning and maximum in the afternoon. The larger amplitudes at UFS are likely due to a lower elevation (i.e., the station being closer to sinks and sources in the valley) and more tourist activity in the vicinity of UFS. Compared to urban sites, which are influenced much more strongly by local biogenic and anthropogenic activities, UFS shows much lower diurnal variability, e.g., by factors of 10 and 34 for δ^{13}C and CO_2, respectively, for a site in Kraków, Poland (Zimnoch *et al.*, 2004).

Back Trajectory Clusters
Characterization of the Clusters

The back trajectory analysis described in the section "HYSPLIT trajectory model" is shown in Fig. 8. Cluster 3 (C3) comprises the fastest and the most frequent (41.7%) flow at UFS and corresponds to a westerly flow from the mid-Atlantic Ocean. Cluster 4 is the second most abundant (19.5%), comprising flow from the northwest. Cluster 2 (14.9%) represents a moderately fast southwesterly flow. Slow-moving air masses coming from the central and west Mediterranean Basin are grouped in Cluster 1, representing 12.1% of the data. Cluster 5 corresponds to northeasterly flows and accounts for the smallest share (11.9%) of trajectories.

Variation of CO_2 Mixing Ratios and δ^{13}C among the Clusters

In order to study whether measured data of CO_2 and its isotopic composition systematically varied with air mass origin, we merged hourly CO_2 mixing ratios and δ^{13}C data

with the respective trajectory information of the same time step (hourly) and grouped them into the five clusters described above (Fig. 8). Afterwards, data were filtered in two steps in order to separate the short-term deviations from the background concentrations and to derive clear information on potential background air masses. The background concentrations derived from the local regression were first subtracted from CO_2 and δ^{13}C values, providing ΔCO_2 and $\Delta\delta^{13}$C. Based on the 96-hour back trajectories of the HYSPLIT Model (see the section "HYSPLIT trajectory model"), the latter data were grouped into air masses in contact with PBL or of completely free troposphere origin. ΔCO_2 and $\Delta\delta^{13}$C by trajectory clusters and seasons are shown in Fig. 9. The highest frequency of air masses contacting the PBL occurred in summer, with 21.3%, while the lowest frequency occurred in winter, with 10.3%. Spring and autumn had contact with the PBL in 14.6% and 12.6% of the cases, respectively.

In summer, CO_2 mixing ratios of clusters from the south significantly differed from the respective median of clusters from the north and west (significant levels of the Student's *t*-test are $p < 0.001$). In wintertime, the two clusters from the north (C4 and C5) showed the most pronounced differences in the measured ΔCO_2 and $\Delta\delta^{13}$C. Clusters 4 and 5 had the highest median ΔCO_2 values and, correspondingly, the lowest values in $\Delta\delta^{13}$C.

Using footprint clustering analysis for ΔCO_2 and $\Delta\delta^{13}$C in wintertime for the JFJ site, Sturm *et al.* (2013) revealed that a cluster representing air masses with surface contact mostly over northern European land masses had the highest median ΔCO_2 value and the second lowest value in $\Delta\delta^{13}$C. Another cluster with high CO_2 mixing ratio had its origin in Eastern Europe. These two clusters according to residence time maps had the same direction as our C4 and C5 clusters, respectively. C4 was always associated with the lowest $\Delta\delta^{13}$C. This can be due to anthropogenic
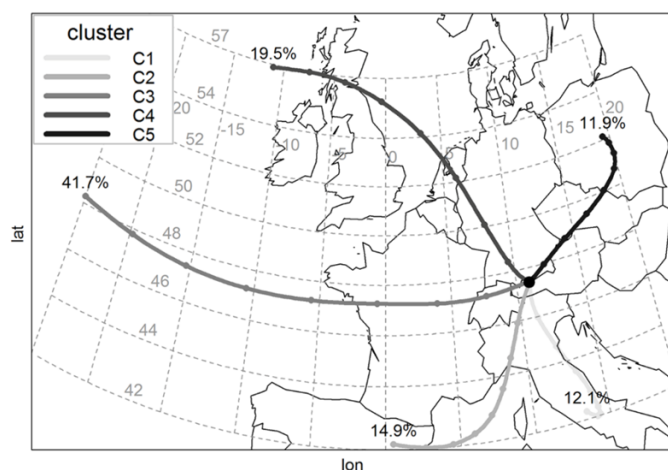

Fig. 8. Clustering of trajectories arriving at UFS in the entire period of May 2012 to November 2014 with their percentages of trajectories.
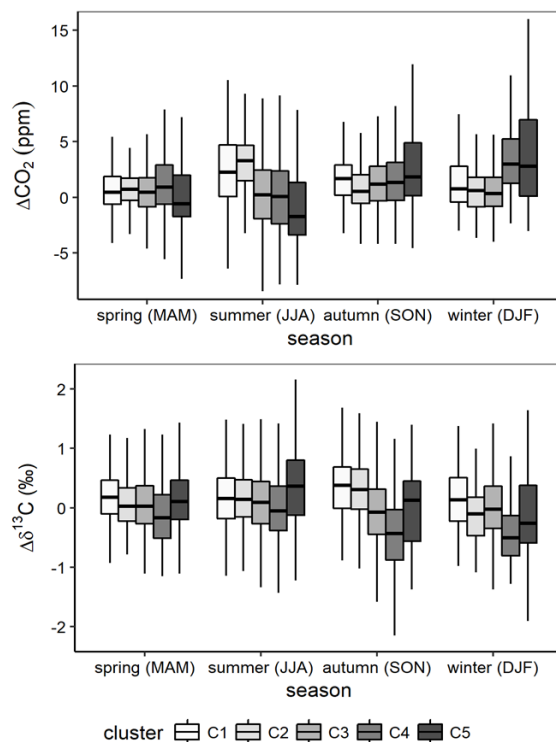
Fig. 9. Boxplots of ΔCO_2 mixing ratio and $\Delta\delta^{13}C$ for all seasons classified for the five clusters of Fig. 8 for the entire period. ΔCO_2 and $\Delta\delta^{13}C$ are filtered for free troposphere air and background concentrations are subtracted.

emissions from this direction (as shown in Fig. 10) being prevalent in all seasons. Cluster 3 had the least differences across seasons, both for ΔCO_2 and $\Delta\delta^{13}C$. In summer, C5 exhibited the highest $\Delta\delta^{13}C$ value and the lowest ΔCO_2 value, respectively.

Case Study: Combination of Trajectory Clusters and PSCF

The potential source contribution function (see the section "HYSPLIT trajectory model") was applied for the detection of geographical areas with an influence on the measured CO_2 concentration. This was done explicitly for air masses causing extremely high CO_2 concentrations (> 75th percentile) in Clusters 4 and 5. PSCF maps (Fig. 10) depict that the air masses from C5 can be traced back to the anthropogenic emissions from coal mining areas in Lusatia and from coal districts in East Germany, while air masses from C4 originate from northwestern Europe, including the high emission regions in the Netherlands and the German Ruhr area.

A comparable PSCF map for $\Delta\delta^{13}C$ (> 75th percentile), equally inferred by trajectories, describes the spatial distribution of probable geographical source locations for $\delta^{13}C$ (i.e., sinks of CO_2) in summer (Fig. 11). The combination of this PSCF map with MODIS land cover (LC) and NDVI map improve our understanding of the

influences of air origin on seasonal variations in CO_2 and $\delta^{13}C$. Fig. 11 clearly illustrates that high values of $\Delta\delta^{13}C$ are influenced by Western, Central, and Southwestern Poland, which according to LC are predominantly croplands. Fig. 11(c) displays that this area is characterized by NDVI values greater than 0.6, indicating dense vegetation in these area with CO_2 uptake.

CONCLUSIONS

We presented a 2.5-year measurement time series of CO_2 mixing ratios and $\delta^{13}C$ at the high altitude GAW station UFS on the northern Alpine ridge. Since the Picarro G1101-i instrument was not upgraded to account for water vapor and methane interferences, comprehensive external data corrections and selections had to be implemented. These corrections would not have been feasible had there not been access to parallel measured carbon dioxide, methane and water vapor. Therefore, from the knowledge obtained with CO_2 measurement devices, adding a reliable drying system on the sample inlet line is strongly recommended.

Clear seasonalities in both the CO_2 mixing ratios and $\delta^{13}C$ were derived with seasonal amplitudes of 15.5 ± 0.15 ppm for CO_2 and of 1.97 ± 0.53‰ for $\delta^{13}C$. Seasonal and diurnal variations of both variables showed similar
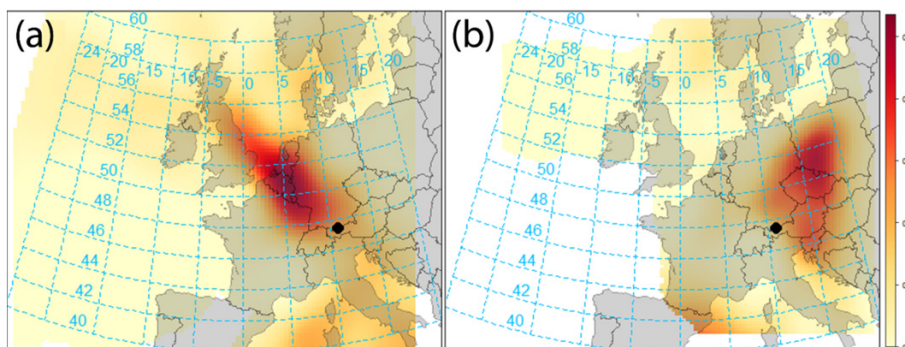
667

Fig. 10. Potential source contribution function plot for ΔCO_2 in wintertime (December to February). (a) PSCF map of Cluster 4 (NW) and (b) PSCF map of Cluster 5 (NE). The position of the site is shown by black circles.
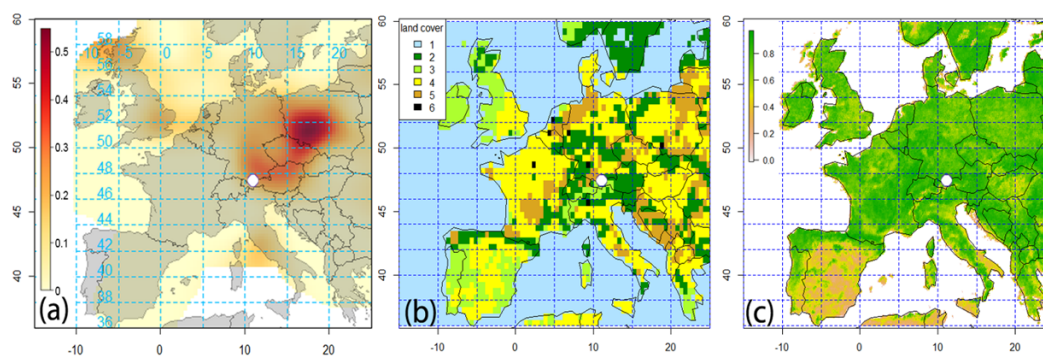

Fig. 11. (a) Potential source contribution function plot for $\Delta\delta^{13}C$ in the summertime (June to August) and (b) MODIS Land Cover for the year 2012. Land cover types on this map are grouped and labeled as follow: 1: water; 2: evergreen, deciduous as well as mixed forests; 3: closed and open shrublands, woody savannas, savannas, grassland; 4: croplands; 5: cropland/natural vegetation mosaic and 6: urban and build-up, (c) NDVI map. The position of the UFS site is shown by white circles.

patterns as at the High Altitude Research Station Jungfraujoch. However, the higher altitude of JFJ led to receiving more frequent free troposphere air masses, and therefore, amplitudes at UFS were generally larger than at JFJ in all seasons. The most pronounced diurnal variabilities were seen in summer at both sites, with an amplitude of 2.9 ppm and 2 ppm for the CO_2 mixing ratio at UFS and JFJ, respectively, and of 0.4‰ and 0.1‰ for the $\delta^{13}C$ at UFS and JFJ, respectively. The smallest diurnal variabilities occurred in winter, when the peak-to-peak amplitude was 1.4 ppm and 1 ppm for the CO_2 at UFS and JFJ and there was no discernible cycle for $\delta^{13}C$.

HYSPLIT classification of the air mass origins at UFS indicated predominant air masses from the west (41.2%), followed by the northwest (19.7%), southwest (14.8%), southeast (12.5%) and northeast (11.8%). The potential source contribution function, using back trajectories as well as atmospheric measurements, provided helpful indications of the origins of air masses potentially influencing a measuring station. So far, this method has been restricted

to the identification of sources in air pollution studies (Begum *et al.*, 2005; Pekney *et al.*, 2006; Kaiser *et al.*, 2007; Pongkiatkul and Oanh, 2007; Zhu *et al.*, 2011), as the probability function in PSCF filters out concentrations below a(n) (arbitrary) threshold. However, in this study, $\delta^{13}C$ measurements and their inverse relationship to CO_2 allowed us to identify atmospheric CO_2 sinks. Among all clusters, high CO_2 mixing ratios in winter (anthropogenic sources) were associated with air masses originating in the Netherlands, the German Ruhr area and Lusatia, whereas high $\delta^{13}C$ values and low CO_2 mixing ratios in summer, representing a terrestrial biosphere sink influence, mostly originated in Poland. For an improved understanding of the contribution of the sources and sinks of carbon dioxide and the exchange of CO_2 between the terrestrial ecosystem and atmosphere, greenhouse gas emission models (e.g., the WRF Greenhouse Gas Model) can be used to simulate high-resolution transport of carbon dioxide.

Sinks and sources' isotopic signatures of continuously measured CO_2 (such as the data presented in this

publication) or records of distinct CO_2 variations (e.g., a sudden enhancement in atmospheric CO_2) could be further identified and quantified using the Keeling plot method (Keeling *et al.*, 1989; Vardag *et al.*, 2016). Access to other related tracers, e.g., carbon monoxide and radon-222 measured at the same site (as is done at UFS), may be a great help in this venture (Hirsch, 2007; Tuzson *et al.*, 2011).

ACKNOWLEDGMENTS

REFERENCES

Allan, D.W. (1966). Statistics of atomic frequency standards. *Proc. IEEE* 54: 221–230.

Ashbaugh, L.L., Malm, W.C. and Sadeh, W.Z. (1985). A residence time probability analysis of sulfur concentrations at grand Canyon National Park. *Atmos. Environ.* 19: 1263–1270.

Begum, B.A., Kim, E., Jeong, C.H., Lee, D.W. and Hopke, P.K. (2005). Evaluation of the potential source contribution function using the 2002 Quebec forest fire episode. *Atmos. Environ.* 39: 3719–3724.

Birmili, W., Ries, L., Sohmer, R., Anastou, A., Sonntag, A., König, K. and Levin, I. (2009). Fine and ultrafine aerosol particles at the GAW station Schneefernerhaus/Zugspitze. *Gefahrstoffe - Reinhalt. Luft* 69: 31–35.

Bowling, D.R., Sargent, S.D., Tanner, B.D. and Ehleringer, J.R. (2003). Tunable diode laser absorption spectroscopy for stable isotope studies of ecosystem–Atmosphere CO_2 exchange. *Agric. For. Meteorol.* 118: 1–19.

Brand, W.A., Assonov, S.S. and Coplen, T.B. (2010). Correction for the ^{17}O interference in $\delta(^{13}C)$ measurements when analyzing CO_2 with stable isotope mass spectrometry (IUPAC Technical Report). *Pure Appl. Chem.* 82: 1719–1733.

Carslaw, D.C. and Ropkins, K. (2012). openair — An R package for air quality data analysis. *Environ. Modell. Software* 27: 52–61.

Channan, S., Collins, K. and Emanuel, W. (2014). Global mosaics of the standard MODIS land cover type data. University of Maryland and the Pacific Northwest National Laboratory, College Park, Maryland, USA.

Chen, H., Winderlich, J., Gerbig, C., Hoefer, A., Rella, C., Crosson, E., Van Pelt, A., Steinbach, J., Kolle, O. and Beck, V. (2010). High-accuracy continuous airborne measurements of greenhouse gases (CO_2 and CH_4) using the cavity ring-down spectroscopy (CRDS) technique. *Atmos. Meas. Tech.* 3: 375–386.

Chen, J., Viatte, C., Hedelius, J.K., Jones, T., Franklin, J.E., Parker, H., Gottlieb, E.W., Wennberg, P.O., Dubey, M.K. and Wofsy, S.C. (2016). Differential column measurements using compact solar-tracking spectrometers. *Atmos. Chem. Phys.* 16: 8479.

Ciais, P., Sabine, C., Bala, G., Bopp, L., Brovkin, V., Canadell, J., Chhabra, A., DeFries, R., Galloway, J., Heimann, M., Jones, C., Le Quéré, C., Myneni, R.B., Piao, S. and Thornton, P. (2013). Carbon and Other Biogeochemical Cycles. In *Climate change 2013: The physical science basis. Contribution of working Group I to the fifth assessment report of the intergovernmental panel on climate change.* Stocker, T.F., Qin, D., Plattner, G.K., Tignor, M., Allen, S.K., Boschung, J., Nauels, A., Xia, Y., Bex, V. and Midgley, P.M. (Eds.). Cambridge University Press, Cambridge, United Kingdom and New York, NY, USA, pp. 465–570.

Cramer, W., Bondeau, A., Woodward, F.I., Prentice, I.C., Betts, R.A., Brovkin, V., Cox, P.., Fisher, V., Foley, J.A., Friend, A.D., Kucharik, C., Lomas, M.R., Ramankutty, N., Sitch, S., Smith, B., White, A. and Young-Molling, C. (2001). Global response of terrestrial ecosystem structure and function to CO_2 and climate change: Results from six dynamic global vegetation models. *Global Change Biol.* 7: 357–373.

Farquhar, G.D., Ehleringer, J.R. and Hubick, K.T. (1989). Carbon isotope discrimination and photosynthesis. *Annu. Rev. Plant Biol.* 40: 503–537.

Ferrarese, S., Apadula, F., Bertiglia, F., Cassardo, C., Ferrero, A., Fialdini, L., Francone, C., Heltai, D., Lanza, A. and Longhetto, A. (2015). Inspection of high–concentration CO_2 events at the Plateau Rosa Alpine station. *Atmos. Pollut. Res.* 6: 415–427.

Fleming, Z.L., Monks, P.S. and Manning, A.J. (2012). Untangling the influence of air-mass history in interpreting observed atmospheric composition. *Atmos. Res.* 104: 1–39.

Friedl, M.A., Sulla-Menashe, D., Tan, B., Schneider, A., Ramankutty, N., Sibley, A. and Huang, X. (2010). MODIS Collection 5 global land cover: Algorithm refinements and characterization of new datasets. *Remote Sens. Environ.* 114: 168–182.

Gantner, L., Hornsteiner, M., Egger, J. and Hartjenstein, G. (2003). The diurnal circulation of zugspitzplatt: Observations and modeling. *Meteorol. Z.* 12: 95–102.

Heckman, N. and Ramsay, J.O. (1996). Spline smoothing with model-based penalties. McGill University, unpublished manuscript.

Henne, S., Brunner, D., Folini, D., Solberg, S., Klausen, J. and Buchmann, B. (2010). Assessment of Parameters describing representativeness of air quality in-situ measurement sites. *Atmos. Chem. Phys.* 10: 3561–3581.

Hirsch, A. (2007). On using radon-222 and CO_2 to calculate regional-scale CO_2 fluxes. *Atmos. Chem. Phys.* 7: 3737–3747.

Hoffnagle, J. (2013). *Relationship between spectroscopic measurements and delta values reported by the G1101i isotopic carbon dioxide analyzers*. Picarro, Inc., Santa Clara, CA.

IPCC (2013). Annex II: Climate system scenario tables (Prather, M., Flato, G., Friedlingstein, P., Jones, C., Lamarque, J.F., Liao, H. andRasch, P. (Eds.)). In *Climate change 2013: The physical science basis. Contribution of working Group I to the fifth assessment report of the intergovernmental panel on climate change*. Stocker, T.F., Qin, D., Plattner, G.K., Tignor, M., Allen, S.K., Boschung, J., Nauels, A., Xia, Y., Bex, V. and Midgley, P.M. (Eds.). Cambridge University Press, Cambridge, United Kingdom and New York, NY, USA, pp. 1395–1446.

IPCC (2014). *Climate change 2014: Synthesis report. Contribution of working group I, II and III to the fifth assessment report of the intergovernmental panel on climate change*. Core Writing Team, R.K. Pachauri and L.A. Meyer (Eds.), IPCC, Geneva, Switzerland, p. 151.

Kaiser, A., Scheifinger, H., Spangl, W., Weiss, A., Gilge, S., Fricke, W., Ries, L., Cemas, D. and Jesenovec, B. (2007). Transport of nitrogen oxides, carbon monoxide and ozone to the Alpine Global Atmosphere Watch stations Jungfraujoch (Switzerland), Zugspitze and Hohenpeissenberg (Germany), Sonnblick (Austria) and Mt. Krvavec (Slovenia). *Atmos. Environ.* 41: 9273–9287.

Keeling, C.D., Bacastow, R.B., Carter, A., Piper, S.C., Whorf, T.P., Heimann, M., Mook, W.G. and Roeloffzen, H. (1989). A three-dimensional model of atmospheric CO2 transport based on observed winds: 1. Analysis of observational data. In *Aspects of climate variability in the pacific and the western Americas*, Peterson D.H. (Ed.), American Geophysical Union, Geophysical Monograph.

Keeling, C.D., Piper, S.C., Whorf, T.P. and Keeling, R.F. (2011). Evolution of natural and anthropogenic fluxes of atmospheric CO2 from 1957 to 2003. *Tellus B* 63: 1–22.

Le Quéré, C., Andrew, R.M., Canadell, J.G., Sitch, S., Korsbakken, J.I., Peters, G.P., Manning, A.C., Boden, T.A., Tans, P.P. and Houghton, R.A. (2016). Global carbon budget 2016. *Earth Syst. Sci. Data* 8: 605–649.

Leuchner, M., Ghasemifard, H., Lüpke, M., Ries, L., Schunk, C. and Menzel, A. (2016). Seasonal and diurnal variation of formaldehyde and its meteorological drivers at the GAW site Zugspitze. *Aerosol Air Qual. Res.* 16: 801–815.

Levin, I., Graul, R. and Trivett, N.B. (1995). Long-term observations of atmospheric CO2 and carbon isotopes at continental sites in Germany. *Tellus B* 47: 23–34.

Locher, R and Ruckstuhl, A. *et al.* (2012). IDPmisc: Utilities of Institute of Data Analyses and Process Design (www.idp.zhaw.ch). R package version 1.1.17. https://CRAN.R-project.org/package=IDPmisc

Miller, J.B., Tans, P.P., White, J.W., Conway, T.J. and Vaughn, B.W. (2003). The atmospheric signal of terrestrial carbon isotopic discrimination and its implication for partitioning carbon fluxes. *Tellus B* 55: 197–206.

Mook, W., Bommerson, J. and Staverman, W. (1974). Carbon isotope fractionation between dissolved bicarbonate and gaseous carbon dioxide. *Earth Planet. Sci. Lett.* 22: 169–176.

Moore, J. and Jacobson, A.D. (2015). Seasonally varying contributions to urban CO2 in the Chicago, Illinois, USA Region: Insights from a high-resolution CO2 concentration and δ13C record. *Elem. Sci. Anth.* 3: 52.

Nara, H., Tanimoto, H., Tohjima, Y., Mukai, H., Nojiri, Y., Katsumata, K. and Ralla, C.W. (2012). Effect of air composition (N2, O2, Ar, and H2O) on CO2 and CH4 measurement by wavelength-scanned cavity ring-down spectroscopy: Calibration and measurement strategy. *Atmos. Meas. Tech.* 5: 2689–2701.

Pandey Deolal, S., Henne, S., Ries, L., Gilge, S., Weers, U., Steinbacher, M., Staehelin, J. and Peter, T. (2014). Analysis of elevated springtime levels of Peroxyacetyl nitrate (PAN) at the high Alpine research sites Jungfraujoch and Zugspitze. *Atmos. Chem. Phys.* 14: 12553–12571.

Pang, J., Wen, X. and Sun, X. (2016a). Mixing ratio and carbon isotopic composition investigation of atmospheric CO2 in Beijing, China. *Sci. Total Environ.* 539: 322–330.

Pang, J., Wen, X., Sun, X. and Hauang, K. (2016b). Intercomparison of two cavity ring-down spectroscopy analyzers for atmospheric 13CO2/12CO2 measurement. *Atmos. Meas. Tech.* 9: 3879–3891.

Pekney, N.J., Davidson, C.I., Zhou, L. and Hopke, P.K. (2006). Application of PSCF and CPF to PMF-modeled sources of PM2.5 in Pittsburgh. *Aerosol Sci. Technol.* 40: 952–961.

Pongkiatkul, P. and Oanh, N.T.K. (2007). Assessment of potential long-range transport of particulate air pollution using trajectory modeling and monitoring data. *Atmos. Res.* 85: 3–17.

R Core Team (2016). R: A language and environment for statistical computing. Vienna: R Foundation for statistical computing; 2013. R foundation for statistical computing.

Ramsay, J.O. and Heckman, N. (1996). *Some theory for L-spline smoothing*. CRM Proceedings and Lecture Notes 18: 371–380.

Rella, C. (2012). Accurate stable carbon isotope ratio measurements in humid gas streams using the Picarro δ13CO2 G2101-i gas analyzer. White Paper of Picarro Inc.

Rella, C.W., Chen, H., Andrews, A.E., Filges, A., Gerbig, C., Hatakka, J., Karion, A., Miles, N.L., Richardson, S.J., Steinbacher, M., Sweeney, C., Wastine, B. and Zellweger, C. (2013). High accuracy measurements of dry mole fractions of carbon dioxide and methane in humid air. *Atmos. Meas. Tech.* 6: 837–860.

Risius, S., Xu, H., Di Lorenzo, F., Xi, H., Siebert, H., Shaw, R. and Bodenschatz, E. (2015). Schneefernerhaus as a mountain research station for clouds and turbulence. *Atmos. Meas. Tech.* 8: 3209–3218.

Ruckstuhl, A.F., Henne, S., Reimann, S., Steinbacher, M., Vollmer, M., O'Doherty, S., Buchmann, B. and Hueglin, C. (2012). Robust extraction of baseline signal of

atmospheric trace species using local regression. *Atmos. Meas. Tech.* 5: 2613–2624.

Seinfeld, J.H. and Pandis, S.N. (2016). *Atmospheric chemistry and physics: From air pollution to climate change*, Third ed. John Wiley & Sons.

Sirois, A. and Bottenheim, J.W. (1995). Use of backward trajectories to interpret the 5-year record of PAN and O_3 ambient air concentrations at Kejimkujik National Park, Nova Scotia. *J. Geophys. Res.* 100: 2867–2881.

Stohl, A. (1996). Trajectory statistics-A new method to establish source-receptor relationships of air pollutants and its application to the transport of particulate sulfate in Europe. *Atmos. Environ.* 30: 579–587.

Sturm, P., Tuzson, B., Henne, S. and Emmenegger, L. (2013). Tracking isotopic signatures of CO_2 at the high altitude site Jungfraujoch with laser spectroscopy: Analytical improvements and representative results. *Atmos. Meas. Tech.* 6: 1659–1671.

Thoning, K., Tans, P. and Komhyr, W. (1989). Atmospheric carbon dioxide at Mauna Loa Observatory: 2. Analysis of the NOAA GMCC data, 1974–1985. *J. Geophys. Res.* 94: 8549–8565.

Tuzson, B., Henne, S., Brunner, D., Steinbacher, M., Mohn, J., Buchmann, B. and Emmenegger, L. (2011). Continuous isotopic composition measurements of tropospheric CO_2 at Jungfraujoch (3580 m a.s.l.), Switzerland: Real-time observation of regional pollution events. *Atmos. Chem. Phys.* 11: 1685–1696.

Vardag, S.N., Hammer, S. and Levin, I. (2016). Evaluation of 4 years of continuous $\delta^{13}C$ (CO_2) data using a moving keeling plot method. *Biogeosciences* 13: 4237–4251.

Vogel, F., Huang, L., Ernst, D., Giroux, L., Racki, S. and Worthy, D. (2013). Evaluation of a cavity ring-down spectrometer for in situ observations of $^{13}CO_2$. *Atmos. Meas. Tech.* 6: 301.

Wen, X.F., Meng, Y., Zhang, X.Y., Sun, X.M. and Lee, X. (2013). Evaluating calibration strategies for isotope ratio infrared spectroscopy for atmospheric $^{13}CO_2/^{12}CO_2$ measurement. *Atmos. Meas. Tech.* 6: 1491–1501.

Werle, P., Mücke, R. and Slemr, F. (1993). The limits of signal averaging in atmospheric trace-gas monitoring by tunable diode-laser absorption spectroscopy (TDLAS). *Appl. Phys. B* 57: 131–139.

WMO (2016). 18th WMO/IAEA meeting on carbon dioxide, other greenhouse gases and related tracers measurement techniques (GGMT-2015), La Jolla, CA, USA, 13-17 September 2015, GAW Report No. 229, World Meteorological Organization, Geneva, Switzerland.

Xia, L., Zhou, L., Tans, P.P., Liu, L., Zhang, G., Wang, H. and Luan, T. (2015). Atmospheric CO_2 and Its $\delta^{13}C$ measurements from flask sampling at Lin'an regional background station in China. *Atmos. Environ.* 117: 220–226.

Xu, J., Lee, X., Xiao, W., Cao, C., Liu, S., Wen, X., Xu, J., Zhang, Z. and Zhao, J. (2017). Interpreting the $^{13}C/^{12}C$ ratio of carbon dioxide in an urban airshed in the Yangtze River Delta, China. *Atmos. Chem. Phys.* 17: 3385–3399.

Yuan, Y., Ries, L., Petermeier, H., Steinbacher, M., Gómez-Peláez, A.J., Leuenberger, M.C., Schumacher, M., Trickl, T., Couret, C. and Meinhardt, F. (2018). Adaptive selection of diurnal minimum variation: A statistical strategy to obtain representative atmospheric CO_2 data and its application to European elevated mountain stations. *Atmos. Meas. Tech.* 11: 1501–1514.

Zellweger, C., Forrer, J., Hofer, P., Nyeki, S., Schwarzenbach, B., Weingartner, E., Ammann, M. and Baltensperger, U. (2003). Partitioning of reactive nitrogen (NO_y) and dependence on meteorological conditions in the lower free troposphere. *Atmos. Chem. Phys.* 3: 779–796.

Zellweger, C., Steinbacher, M. and Buchmann, B. (2011). System and performance audit of surface ozone, methane, carbon dioxide, nitrous oxide and carbon monoxide at the global GAW station Zugspitze-Schneefernerhaus, Germany, June 2011.

Zhou, L., White, J.W., Conway, T.J., Mukai, H., MacClune, K., Zhang, X., Wen, Y. and Li, J. (2006). Long-term record of atmospheric CO_2 and stable isotopic ratios at Waliguan Observatory: Seasonally averaged 1991–2002 source/sink signals, and a comparison of 1998–2002 record to the 11 selected sites in the Northern Hemisphere. *Global Biogeochem. Cycles* 20: GB2001.

Zhu, L., Huang, X., Shi, H., Cai, X. and Song, Y. (2011). Transport pathways and potential sources of PM_{10} in Beijing. *Atmos. Environ.* 45: 594–604.

Zimnoch, M., Florkowski, T., Necki, J.M. and Neubert, R.E. (2004). Diurnal variability of $\delta^{13}C$ and $\delta^{18}O$ of atmospheric CO_2 in the urban atmosphere of Kraków, Poland. *Isot. Environ. Health Stud.* 40: 129–143.

atmosphere

Article

Pollution Events at the High-Altitude Mountain Site Zugspitze-Schneefernerhaus (2670 m a.s.l.), Germany

Homa Ghasemifard [1,*], Felix R. Vogel [2], Ye Yuan [1], Marvin Luepke [1], Jia Chen [3,4], Ludwig Ries [5], Michael Leuchner [6], Christian Schunk [7], Sanam Noreen Vardag [8] and Annette Menzel [1,4]

[1] Professorship of Ecoclimatology, Technische Universität München, 85354 Freising, Germany; yuan@wzw.tum.de (Y.Y.); luepke@wzw.tum.de (M.L.); amenzel@wzw.tum.de (A.M.)
[2] Climate Research Division, Environment and Climate Change Canada, Toronto, ON M3H 5T4, Canada; felix.vogel@canada.ca
[3] Professorship of Environmental Sensing and Modeling, Technische Universität München, 80333 Munich, Germany; jia.chen@tum.de
[4] Institute for Advanced Study, Technische Universität München, 85748 Garching, Germany
[5] German Environment Agency (UBA), 82475 Zugspitze, Germany; ludwig.ries@uba.de
[6] Physical Geography and Climatology, RWTH Aachen University, 52056 Aachen, Germany; michael.leuchner@geo.rwth-aachen.de
[7] Department for Safety and Radiation Protection, Technische Universität München, 85748 Garching, Germany; christian.schunk@tum.de
[8] Heidelberg Center for the Environment, Universität Heidelberg, 69120 Heidelberg, Germany; svardag@iup.uni-heidelberg.de
* Correspondence: homa.ghasemifard@wzw.tum.de; Tel.: +49-(0)-816-171-4743

check for updates

Abstract: Within the CO_2 time series measured at the Environmental Research Station Schneefernerhaus (UFS), Germany, as part of the Global Atmospheric Watch (GAW) program, pollution episodes are traced back to local and regional emissions, identified by $\delta^{13}C(CO_2)$ as well as ratios of CO and CH_4 to CO_2 mixing ratios. Seven episodes of sudden enhancements in the tropospheric CO_2 mixing ratio are identified in the measurements of mixing/isotopic ratios during five winter months from October 2012 to February 2013. The short-term CO_2 variations are closely correlated with changes in CO and CH_4 mixing ratios, achieving mean values of 6.0 ± 0.2 ppb/ppm for CO/CO_2 and 6.0 ± 0.1 ppb/ppm for CH_4/CO_2. The estimated isotopic signature of CO_2 sources (δ_s) ranges between $-35‰$ and $-24‰$, with higher values indicating contributions from coal combustion or wood burning, and lower values being the result of natural gas or gasoline. Moving Keeling plots with site-specific data selection criteria are applied to detect these pollution events. Furthermore, the HYSPLIT trajectory model is utilized to identify the trajectories during periods with CO_2 peak events. Short trajectories are found covering Western and Central Europe, while clean air masses flow from the Atlantic Ocean and the Arctic Ocean.

1. Introduction

Since the beginning of the industrial era, atmospheric greenhouse gas (GHG) concentrations have been rapidly increasing due to fossil fuel burning and deforestation [1]. Carbon dioxide (CO_2) is the most important anthropogenic GHG, and its concentration has increased by more than 45% from the pre-industrial level of 278 ppm (parts per million) to 405 ppm in the year 2017 [2]. Continuous

atmospheric CO_2 measurements significantly contribute to a better understanding of the global carbon cycle and its effect on the earth's climate. The Environmental Research Station Schneefernerhaus (UFS) has been part of the Global Atmospheric Watch (GAW) program of the World Meteorological Organization (WMO). Due to its remote and elevated location, the UFS is relatively less influenced by direct anthropogenic emissions and thus measurements of background concentrations there can be regarded as representative of a larger region [3,4]. Nevertheless, the station is occasionally influenced by local-to-regional emissions due to the air mass transport of polluted boundary layer air and/or local effects. These polluted air masses contain signals from continental sources, as indicated by the high variability in trace gas concentrations on time scales of hours and days [5]. In order to improve the retrieval of atmospheric background CO_2 concentrations from measurements at these remote sites, it is crucial to investigate these pollution-affected periods systematically, as well as to identify their source regions.

In order to study sudden increases and short-term variability in atmospheric trace gases at mountain stations, in situ measurements of trace gases with anthropogenic sources as well as statistical trajectory methods have been frequently applied to define the source, identify its origin, and elucidate and characterize the causes of the variation. For instance, Apadula et al. [6] analyzed atmospheric CO_2 concentrations at three Alpine sites (Plateau Rosa and Monte Cimone in Italy, and Zugspitze in Germany) and identified a short-lived episode of large fluctuations in the CO_2 mixing ratios. This was similarly observed at Plateau Rosa and Zugspitze, but with a delay of 12–18 h, as shown by backward trajectory and cluster analysis. Kaiser et al. [7] detected the potential source of nitrogen oxides (NO_x), carbon monoxide (CO), and ozone (O_3) using trajectory residence time statistics at five Alpine GAW stations (Zugspitze/Hohenpeissenberg (Germany), Sonnblick (Austria), Jungfraujoch (Switzerland), and Mt. Krvavec (Slovenia)). Furthermore, Uglietti et al. [8] investigated the transport of air masses with high CO_2 levels to the Jungfraujoch station (JFJ) using backward Lagrangian particle dispersion model simulations, and employed CO_2 and oxygen (O_2) signatures to classify these air masses. Tuzson et al. [9] focused on the pronounced enhancement in the tropospheric CO_2 at Jungfraujoch in February 2009. During this period, four events were captured in which CO and CO_2 mixing ratios were highly correlated as a proxy for fossil fuel CO_2, as well as the CO_2 mixing ratio and isotopic composition of atmospheric CO_2 $\delta^{13}C$, using the Keeling method. Ferrarese et al. [10] identified two significantly high CO_2 concentration events at four high-altitude European stations in February 2004 using the backward trajectories of the polluted air masses from the European boundary layer as indicated by CO and O_3. Ghasemifard et al. [4] showed that the high CO_2 mixing ratios in winter (from the year 2012 to 2014) at the UFS originated in the German Ruhr area, the Netherlands, and Lusatia (an area bounded by Germany, Poland, and the Czech Republic) based on CO_2 and $\delta^{13}C$ measurements, as well as potential source contribution functions (PSCFs).

$\delta^{13}C$ has been used in numerous studies to gain insight into different aspects of the carbon cycle (e.g., [9,11]). Nevertheless, the isotopic composition of atmospheric CO_2 is related to the atmosphere–biosphere exchange, because the terrestrial ecosystem (photosynthesis/respiration) and air–sea gas exchanges differently discriminate against ^{13}C [12,13]. Therefore, the $\delta^{13}C$ signature is often used to distinguish CO_2 contributions from oceanic, biospheric, and anthropogenic CO_2 emissions [14]. Furthermore, since different CO_2 emitters have different $\delta^{13}C$ signatures, the carbon isotope ratio enables the identification and quantification of CO_2 emitters and their underlying mechanisms at the local to regional levels [15]. Various ranges of $\delta^{13}C$ have been obtained for combustion sources: −44‰ to −37‰ for natural gas combustion, −32‰ to −26‰ for gasoline combustion, −27‰ to −24‰ for coal combustion, and −27‰ to −22‰ for wood combustion [14,16–18].

It is well known that a large amount of global CO, which is produced by the incomplete oxidation of carbon, originates from anthropogenic sources. Moreover, approximately 70% of the total sources of CO in Europe are anthropogenic [19]. Thus, with CO as a tracer, anthropogenic CO_2 emissions from fossil fuel combustion, and therefore CO_2 emissions from regional sources, can be identified (e.g., [9,20–22]). The ratio of atmospheric CO to CO_2 (CO/CO_2) has been utilized to quantify fossil

fuel contribution in relation to CO_2 variations, and to determine the type of combustion and burning efficiency; high ratios indicate poor burning and trace traffic emissions [9,23,24].

Methane (CH_4), the second most essential anthropogenic GHG gas after CO_2, has increased from the pre-industrial level of 722 ppb to the present level of 1859 ppb (2017) due to increased emissions from anthropogenic sources [2]. CH_4 is emitted from a variety of natural and anthropogenic sources and also from ground level sources (e.g., ruminants, natural gas leakages, coal mining, or waste deposits). The source of CH_4 in Western Europe is mainly anthropogenic [25]. Though vehicle emissions are an insignificant source on a global scale [26], they can count for up to 30% of total emissions in areas with high traffic density [27]. Several studies have shown that there exist positive correlations between atmospheric CO_2 and CH_4 mixing ratios mostly in the winter (e.g., [28,29]). Based on the assumption that CO_2 and CH_4 originate from similar sources and sinks, the CH_4 to CO_2 emission ratio (CH_4/CO_2) is utilized to filter observed atmospheric CO_2 data influenced by local sources/sinks [30].

In this study, we performed the analysis from 1 October 2012 to 1 March 2013 at the UFS/Zugspitze. During this period, we captured several consecutive short-term pollution events with a strong increase ($>\sim15$ ppm) in the measured CO_2 concentration. The period was restricted to these five months of autumn/winter in order to minimize the effect of biological activities (such as photosynthesis and respiration) in the interpretation of pollution signals. It was found that employing the in situ measurements of isotopic signatures of CO_2 using $\delta^{13}C(CO_2)$, the emission ratios of CO/CO_2 and CH_4/CO_2, and the backward trajectories from the HYSPLIT (Hybrid single-particle Lagrangian integrated trajectory model) provided essential information for the identification, characterization, and source estimation of pollution events, as shown in the subsequent sections.

2. Material and Methods

2.1. Measurement Site

The high Alpine Environmental Research Station Schneefernerhaus (UFS) is located in the northern Alps at an altitude of 2650 m above see level (a.s.l.) (47° 25′ N, 10° 59′ E), nearly 300 m below the summit of Mount Zugspitze, the highest mountain in Germany, and about 90 km southwest of Munich. The UFS is often above the planetary boundary layer (PBL) and receives well-mixed and/or free tropospheric air masses [31]. Nevertheless, UFS is occasionally influenced by regional emissions such as the transport of PBL air masses due to thermally induced flow systems [5,32–34], although this issue can be addressed by characterizing the measurements based on their air mass histories and origins. Further detailed site information is given in the GAW station information system [35].

2.2. Analyzers and Sampling Systems

In this study, all instruments were operated at the German Environment Agency (Umweltbundesamt, UBA) laboratory and connected to the same air inlet (2670 m a.s.l.); thus, they measured the same air samples.

We measured CO_2 and $\delta^{13}C(CO_2)$ with a Picarro G1101-i analyzer (manufactured in 2010 by Picarro Inc., USA, and measuring at a rate of 0.1 Hz) and calibrated them using two standard gases with high and low concentrations (standard 1:350.1 ± 0.5 ppm CO_2 mixing ratio and −3.3‰ ± 0.2‰ $\delta^{13}C$; standard 2:503.4 ± 0.5 ppm CO_2 mixing ratio and −20.0‰ ± 1.0‰ $\delta^{13}C$) in synthetic air. Details on our air sampling inlet and calibration systems are presented in Ghasemifard et al. [4]. Notably, this analyzer was not upgraded to account for the spectral interferences caused by methane (bias $\delta^{13}C$ by 0.4‰ CH_4 ppm^{-1}) and water vapor (including water vapor dilution, water vapor pressure broadening, and HDO spectral interference effects). Several studies have evaluated and validated the G1101-i analyzer measurements before and after upgrading in comparison with other measurement devices [4,36–40]. As described by Ghasemifard et al. [4], the measured CO_2 and $\delta^{13}C$ were post-corrected, in which parallel measured CO_2, H_2O, and CH_4 were employed.

The UBA performed CH_4 measurements with a Picarro EnviroSense 3000i analyzer (using cavity ring-down spectroscopy) and recorded CO data by an Aero-Laser AL5002 (ultraviolet-fluorescence instrument). Further, the UBA carried out calibration and quality assurance for these atmospheric compounds following GAW quality standards. The UBA station standards for interconnection with the international standard reference were reported on the WMO/NOAA-2004 scale for CO and WMO X2004a scale for CH_4 by National Oceanic and Atmospheric Administration (NOAA), Boulder, Colorado.

For this study, we aggregated the data of CO, CH_4, CO_2, and $\delta^{13}C$ to hourly averages by the statistical program R [41] and employed the R packages Openair [42] and ggplot2 [43] for further analyses.

2.3. Keeling Plot Method

In order to calculate the mean isotopic signature of a source, the Keeling plot method [44,45] links variations in CO_2 and $\delta^{13}C$ by adding CO_2 from that source to the background atmospheric CO_2 mixing ratio and background isotopic ratio [46]. The mass balance of the total CO_2 is

$$C_{tot} = C_{bg} + C_s \tag{1}$$

where C_{tot}, C_{bg}, and C_s respectively refer to the total measured CO_2 mixing ratio, background CO_2 mixing ratio, and source CO_2 mixing ratio. Given the mass balance,

$$\delta_{tot} \cdot C_{tot} = \delta_{bg} \cdot C_{bg} + \delta_s \cdot C_s \tag{2}$$

where δ represents $\delta^{13}C$ of each CO_2 component. Rearranging and combining Equations (1) and (2) yields

$$\delta_{tot} = C_{bg}/C_{tot} \left(\delta_{bg} - \delta_s \right) + \delta_s \tag{3}$$

In the case of a single-source pollution event, a plot of the measured (total) $\delta^{13}C$ versus $1/CO_2$ yields a straight line with a y-intercept of δ_s. It is crucial to observe that Equation (3) of the Keeling method involves two basic prerequisites. Firstly, the background and isotopic signature of the source need to be constant. Secondly, sources and sinks of different isotopic signatures may not co-occur during the observation [15]. The effect of disregarding these criteria is also graphically depicted in Vardag et al. [46]. Note that the background value does not have to be known in order to calculate the mean source signature [15].

As an example, Figure 1a shows one of the events in this study (E7), while Figure 1b displays the corresponding Keeling plot.

In order to calculate the source signature as an intercept, a linear regression needs to be fitted to the data (e.g., Figure 1b). Miller and Tans [47] compared two models for the regression, Model I (ordinary least-squares regression in which only y-errors are taken into account), and Model II (regression fit; e.g., weighted total least squares (WTLS), which accounts for errors on both x and y [48]). Miller and Tans [47] found that Model I is biased for the intercept, even when the values of R^2 are high. Therefore, in this paper, we employed WTLS to fit the linear regression in the Keeling method.

Based on the classical Keeling plot method, Vardag et al. [46] presented a method to accurately determine the source signature for a continuous data set (moving Keeling plot approach) following Equation (3). The advantage of this approach is that the prerequisites of the Keeling approach do not have to be checked individually for the entire data set, which would be very tedious for a continuous long-term data set. This method provides correct results only when a number of criteria are fulfilled. These criteria then automatically discard situations in which sources and sinks occur simultaneously and in which the mean source signature or the background value change. Note that the optimal set of parameters was found by Vardag et al. [46] and validated using a simulated data set in Heidelberg. The

individual filter criteria and the rationale behind the filter criteria are adopted from Vardag et al. [46] and listed in Table 1.
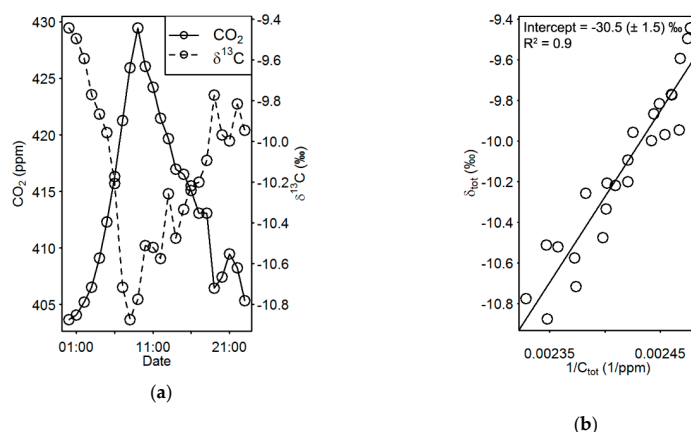

Figure 1. Source signature determination using the Keeling plot. (**a**) The CO_2 mixing ratio (solid line) and $\delta^{13}C$ (dashed line) of event E7, and (**b**) the Keeling plot for the entire event as shown in (**a**). The y-intercept and coefficient of determination R^2 of the fitted linear regressions following Equation (3) are given in (**b**).

Table 1. Filter criteria and rationale based on Vardag et al. [46].

Filter Criteria	Rationale
Monotonous CO_2 increase over 5 h	Reasons for a decrease could be a simultaneously occurring sink or a boundary layer break-up, both hurting the prerequisites of a Keeling plot.
Error of intercept < 2‰	Changes of mean source mix due to change of emission characteristics, background or footprint area show a non-linear behavior in a Keeling plot. Thus, choosing a maximum error of the intercept, δ_S of <2‰, can filter out these situations.

Moreover, there is another criterion in Vardag et al. [46] that is not applicable in this study, namely an increase in the CO_2 mixing ratio by more than 5 ppm. Simultaneously occurring sources and sinks bias the retrieved source signature more strongly the smaller the net CO_2 signal is. Therefore, the criterion is chosen to exclude periods where the photosynthetic sink is similarly strong to the total CO_2 sources. Vardag et al. [46] report that a threshold of 5 ppm is sufficient to eliminate strongly biased source signatures in Heidelberg, a medium-sized city that is strongly influenced by local sinks and sources and located about 20 km southwest of an industrial area (Mannheim/Ludwigshafen) [22]. In contrast, the UFS is a remote mountain site where there is no sudden or direct influence from the photosynthetic sink [4]. Therefore, provided that there is an increase in CO_2, the second criterion (>5 ppm) is redundant. Regarding the applied criteria in Table 1, note that we also tested shorter periods (i.e., 4 and 3 h/data point); however, the number of events detected was the same. Therefore, the initial 5 h period was preferred since a higher number of data points will supposedly yield more reliable results.

Seven events within the study period satisfied the criteria for the moving Keeling approach (see Table 2).

In Section 3.1, the moving Keeling approach is presented in parallel to the classical Keeling plot in order to detect the pollution source signature at the UFS. The moving Keeling plot method works so that, for example, for the determination of the mean source signature at 14:00 h, we use the hourly CO_2

and δ^{13}C measurements from 12:00 h to 16:00 h and fit a regression line. To select episodes for the classical Keeling plots, periods with a CO_2 increase of more than ~15 ppm within timescales of hours and days were selected (see Table 2). In order to provide comparability with the moving Keeling plot analysis we removed the non-monotonously increasing parts of those episodes and considered only the front shoulder of the CO_2 mixing ratios. If we considered the latter selection in the example of Figure 1, the source signature would be −33.8 ± 1.7‰ instead of −30.5 ± 1.5‰, due to the bias caused by the decreasing part of the event.

2.4. Emission Ratio

In order to determine the emission ratios (slope of the regression) and accuracy (coefficient of determination R^2), we examined the relationship between the CO and CO_2, as well as the CH_4 and CO_2 mixing ratios using scatter plots and fitted linear regressions, respectively. However, there are different approaches to determining the emission ratios (CO/CO_2 and CH_4/CO_2). Occasionally the emission ratios are calculated as $\Delta CO/\Delta CO_2$ or $\Delta CH_4/\Delta CO_2$, where Δ denotes the difference of the total concentration to the background concentration (which is individually defined using particular techniques (e.g., [49,50])). In some studies, the emission ratio is calculated as $CO/\Delta CO_2$, whereas sometimes no background is removed (e.g., [51,52]). In this paper, in order to be consistent with the Keeling plot data selection, we calculated emission ratios on the total emission ratios for periods from the minimum (when the CO_2 mixing ratio started to increase) to the maximum (when the highest value of the CO_2 mixing ratio was reached). Table 2 presents the corresponding lengths of these periods for each event.

2.5. HYSPLIT Trajectory Model

We employed the HYSPLIT (hybrid single-particle Lagrangian integrated trajectory) model in order to study air transport during the episodes and characterize the CO_2 source regions [53,54]. The underlying meteorological model was obtained from the Global Forecast System and driven by 3-h forecast weather data at a 0.5° resolution. We calculated hourly backward trajectories for the 96 h before the air masses reached the UFS. The terrain altitude for the trajectory starting point at the UFS is 1312.4 m a.s.l. in the model. Thus, back trajectory calculation was started at an altitude of 1500 m above ground level (a.g.l.), resulting in 2812 m a.s.l., which roughly matches the sample inlet height (2670 m a.s.l.).

2.6. PSCF

Additionally, we utilized the potential source contribution function (PSCF) method [55,56] to plot the spatial distribution of potential geographic source locations. The PSCF calculates the probability ($0 \leq P_{ij} \leq 1$) that a potential source is located at latitude i and longitude j. Therefore, an air parcel passing through that location along the trajectory to the receptor site collects the material and characteristics from the source. The probability for a given cell is defined as $P_{ij} = m_{ij}/n_{ij}$, where n_{ij} is the total number of times that the trajectories pass through the cell (i, j) and m_{ij} is the number of trajectories associated with concentration values at the receptor site greater than a specific threshold. In this study, the threshold was set to be the 90th percentile of the CO_2 mixing ratio and the 24 h measurement before and after each event is included in the 90th percentile calculation.

3. Results and Discussion

Figure 2 shows a high-resolution time series of the CO_2 mixing ratio, corresponding the δ^{13}C values, CO mixing ratio, and CH_4 mixing ratio from October 2012 to February 2013. According to Figure 2, episodes of high CO_2 concentrations are observed during similar periods of CO and CH_4 mixing ratios. These episodes are labeled E1–E7. The mixing ratios of all three trace gases are highly correlated, while δ^{13}C was anti-correlated to the CO_2 mixing ratio. In subsequent sections, we present a detailed investigation of the seven episodes exhibiting high CO_2. Table 2 contains the date, duration

of each episode, and duration of their increasing part (i.e., from the start of the increase to the moment the maximum CO_2 concentration is reached).
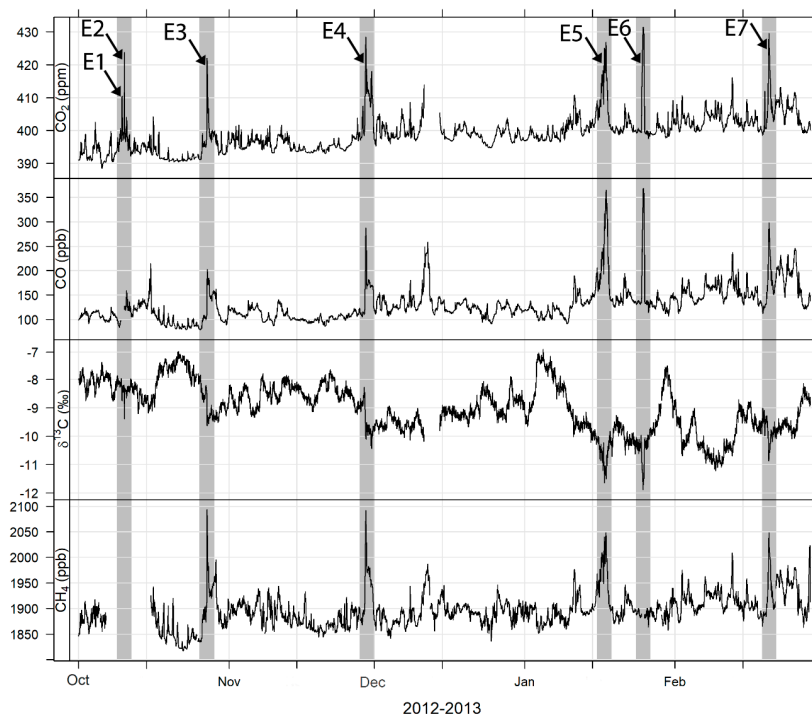

Figure 2. Temporal variation of the mixing ratios of CO_2, CO, and CH_4, as well as the stable carbon isotope ratio of atmospheric CO_2 ($\delta^{13}C$), for five months at the Environmental Research Station Schneefernerhaus (UFS). The arrows point to the studied episodes labeled E1–E7. The shaded areas indicate distinct pollution events (the first event actually contains separate two events, but due to the short period between them the shaded area is shown as a single event).

Table 2. Date and duration of investigated episodes.

Episode	Day	Month-Year	Total Duration (h)	Duration until the Maximum of CO_2 (h)
E1	09	10-2012	9	5
E2	10	10-2012	6	3
E3	27–28	10-2012	25	9
E4	28–30	11-2012	62	9
E5	15–18	01-2013	91	43
E6	25	01-2013	20	10
E7	19–21	02-2013	42	10

3.1. $\delta^{13}C(CO_2)$ and Keeling Plot

Figure 3a shows the resulting isotope signatures for each event using the classical Keeling plot method. It has to be noted again that only the increasing parts of each event are considered for this calculation. The intercept values range between −35‰ and −24‰, and $\delta^{13}C_s$ is most enriched in E1 (−24.2‰ ± 1.2‰) and most depleted in E4 (−34.9‰ ± 0.6‰). For all the events, the $\delta^{13}C$ to the $1/CO_2$ relationship is well described by the WTLS regression with a high coefficient of determination (>0.90);

except for one case (E5, $R^2 = 0.82$). The error bars in Figure 3a are the intercept error, which is listed in Table S1 and calculated by WTLS regression.

The averaged $\delta^{13}C_s$ signatures (Figure 3a) (i.e., −29‰) are in agreement with the signatures (−20‰ to −30‰) determined by Tuzson et al. [9] at the high Alpine research station Jungfraujoch (JFJ) at an altitude of 3580 m a.s.l. This ^{13}C signature represents a typical isotopic combination of anthropogenic and biological sources. The higher values of E1 and E2 (−24.2‰ ± 1.2‰ and −26.3‰ ± 0.9‰) suggest a significant contribution from coal combustion or wood burning, while the low values of E3–E7 (−34.9‰ to −29.6‰) are consistent with contributions from natural gas or gasoline [14,16].

The moving Keeling plot method with the specified data selection criteria (see Section 2.4) was employed to detect pollution events at the UFS automatically. The moving Keeling plot calculated the source signature for each of the five data points (i.e., 5 h), and depending on the length of the event, it generated several values per event; thus, the detected isotopic source signatures are presented as box plots. The whiskers of the boxplots indicate the minimum and maximum values, the lower and upper boundaries of the boxes are 25th- and 75th-percentiles, and the horizontal lines inside the boxes represent medians. The mean difference between the mean value of the classical and moving Keeling plots is 0.0‰ ± 0.5‰. This result confirms the reliability of the applied criteria.
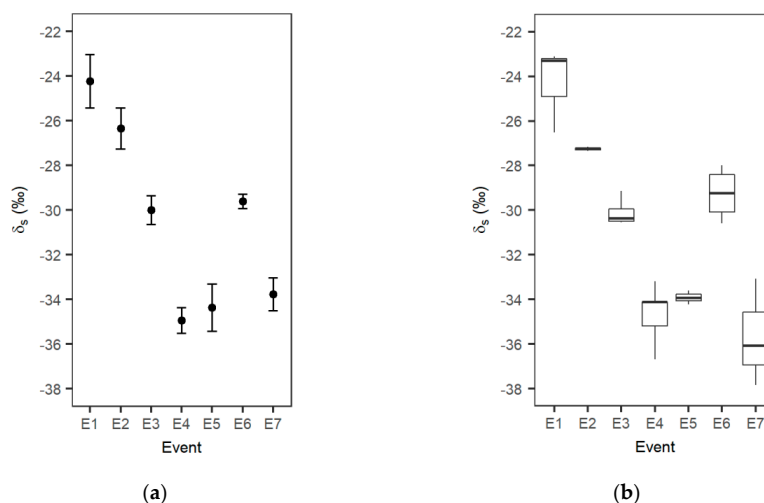

(a)　　　　　　　　　　　　　　　　　**(b)**

Figure 3. Intercepts of Keeling plots (δ_s) during the individual pollution events. (**a**) Results of the classical Keeling plot method. Black circles indicate the intercept and the error bars show the error of the intercept. (**b**) Results of moving the Keeling plot method depicted as box plots. The whiskers of the boxplots indicate the minimum and maximum values, the lower and upper boundaries of the boxes are the 25th- and 75th-percentiles, and the horizontal lines inside boxes represent medians.

3.2. CO/CO$_2$ Emission Ratios

Figure 4 shows a plot of the CO/CO_2 ratios for all individual events except for E1 and E2, for which no CO data were available. The CO/CO_2 ratios range between 3.5 and 8.0 ppb/ppm. High coefficients of determination (see Figure 4) support our hypothesis that a considerable part of the CO_2 contribution must have been due to combustion of fossil fuels (i.e., gasoline or diesel) and that CO and CO_2 were emitted from the same source. Notwithstanding, biogenic CO_2 from below and above ground respiration can be transported to the UFS along with anthropogenic CO_2, which includes a certain bias to CO and fossil fuel CO_2 relations that cannot be excluded.
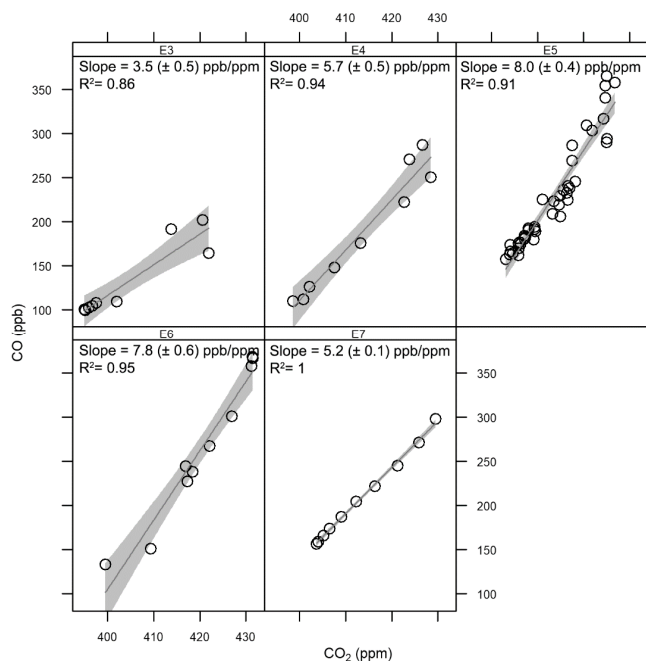
Figure 4. Linear regressions of the hourly mean mixing ratios of CO and CO_2 for the five pollution events E3–E7 (CO data not available for E1 and E2). The slope and coefficient of determination R^2 are given. The shaded areas around the regression lines represent the range in which the true regression line lies at a certain level of confidence (95% in the plot). The slope of the regressions corresponds to CO/CO_2 emission ratios.

While comparing our results with those obtained at other sites in Europe, a wide range of emission ratios from fossil fuel emissions was apparent, providing some idea of what to expect for the large-scale European source mix. Table 3 provides a list of some recent studies on CO/CO_2 emission ratios for local traffic emissions and fossil fuel combustion. The measured CO/CO_2 ratios at the JFJ in February 2009 by Tuzson et al. [9] are of particular interest. The authors studied four distinct pollution events within a month, and the emission ratios ranged from 7.3 to 13.1 ppb/ppm, which are generally higher than ours, except for E5 and E6. The higher values could be due to contributions from biogenic sinks, reducing CO_2 while leaving CO unaffected. However, the technological improvement of vehicles with lower CO emissions could explain the lower ratios when comparing the ratio values with studies from previous years (e.g., [23]). Popa et al. [23] measured CO and CO_2 close to each end of a highway tunnel in Islisberg, Switzerland, in the year 2011. Vollmer et al. [57] measured emissions at another highway tunnel (Gubrist) in the same region in the year 2004. The values of the year 2011 measurement are almost half of those obtained in the year 2004 [23].

Table 3. CO/CO_2 emission ratios for traffic and anthropogenic emissions in Europe.

Reference	CO/CO_2 (ppb/ppm)	Location	Environment	Year
Vollmer at al. (2007) [57]	9.19 ± 3.74	Switzerland	tunnel	2004
Vogel et al. (2010) [22]	13.5 ± 2.5	Germany	city	2002–2009
Tuzson et al. (2011) [9]	9.35 ± 2.66	Switzerland	remote site	2009
Popa et al. (2014) [23]	4.15 ± 0.34	Switzerland	tunnel	2011
Ammoura et al. (2014) [49]	5.68 ± 2.43	France	tunnel	2012
This study	6.02 ± 0.12	Germany	remote site	2012–2013

3.3. CH$_4$/CO$_2$ Emission Ratios

Figure 5 shows the observed CH$_4$/CO$_2$ ratios for four events from October 2012 to March 2013 (no CH$_4$ data are available for E1, E2, and E6). The ratios (regression slope) vary from 4.7 to 7.4 ppb/ppm. It was found that emission ratios at the UFS are lower than at other mountain sites that reported 10 to 20 years ago (e.g., the Schauinsland (1205 m a.s.l.), Germany, with a mean ratio of 7.8 ± 1.0 ppb/ppm [52], and the Kasprowy Wierch (1987 m a.s.l.), Poland, with 10.7 ± 0.3 ppm/ppb [51]). Schmidt et al. [52] list a single diurnal cycle of CH$_4$ and CO$_2$ at the JFJ in December 1988, where the emission ratio was 5.3 ± 0.9 ppb/ppm. Worthy et al. [29] observed a decrease in anthropogenic methane emissions in Europe and Siberia from the year 1988 to 2005, which led to low ratios of CH$_4$/CO$_2$. The CH$_4$/CO$_2$ emission ratios obtained in this study compared well with the results of the highway tunnel measurements (4.6 ± 0.2 ppb/ppm) by Popa et al. [23]; indicating local traffic and transport characteristics of the western European vehicle fleet.
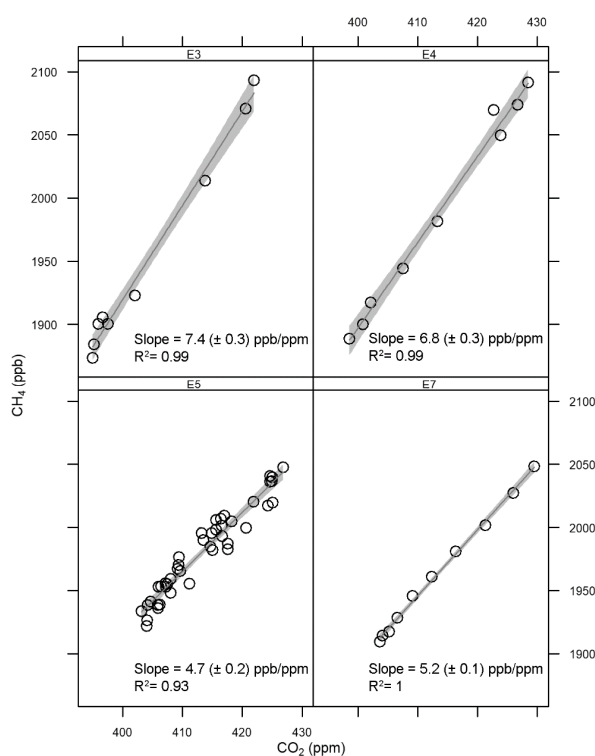

Figure 5. Linear regressions of hourly mean mixing ratios of CH$_4$ and CO$_2$ for four pollution events (CH$_4$ data not available for E1, E2, and E6). The slope and coefficient of determination R^2 are given. The shaded areas around the regressions line represent the range in which the true regression line lies at a certain level of confidence (95% in the plot). The slope of the regressions corresponds to CH$_4$/CO$_2$ emission ratios.

3.4. Backward Trajectories

In order to identify the origin and path followed by the air masses arriving at the UFS during each of the episodes, we merged the hourly output of the HYSPLIT model with the hourly data on atmospheric composition. Figure 6 shows the flow patterns and height of trajectories to the receptor

site for E1 and E2. Trajectories are shown in three plots, which contain hourly trajectories of high CO_2 mixing ratios during the entire events (middle panel), 24 h before the events (left panel), and 24 h after the events (right panel). Trajectories E1 and E2 are combined due to the short time (4 h) between the two events.
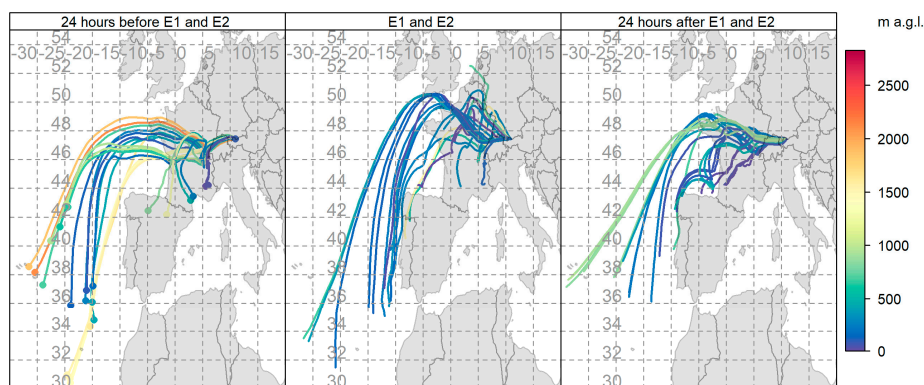

Figure 6. HYSPLIT backward trajectories (1-h interval) of air masses reaching the UFS during pollution events E1 and E2. The three plots are 24 h before the events (left panel), E1 and E2 combined during the events (middle panel), and 24 h after the events (right panel). The color of the trajectories shows the respective height above ground level (m).

CO_2 mixing ratio rapidly increased by 13 ppm in E1 from 397 to 410 ppm, and by 24 ppm in E2 from 399 to 423 ppm, within 5 h and 3 h, respectively. Also, these events were followed by rapid decreases in which the CO_2 mixing ratio dropped to 397 ppm within 4 h in E1, and to 397 ppm within 3 h in E2. Moreover, trajectory analysis for E1 and E2, which occurred only 4 h apart, shows no changes in air mass trajectories for 24 h before, during, or 24 h after the events (see Figure 6). Since almost all trajectories flow from the Atlantic Ocean and are assumed to carry clean air, this suggests that the concentration enhancements were caused by regions nearby. Regarding emissions, residential wood burning (mainly in the villages) in the Alpine area is a conventional heating system and a major contributor to CO_2 enhancement that fits well with the results of the Keeling plot intercept for E1 and E2 (−24.2‰ and −26.3‰, respectively).

In contrast to E1 and E2, the CO_2 mixing ratio increased within 20–91 h and decreased within 9–43 h during the other five events. E3–E7 exhibited short trajectories during the period of the events (CO_2 enhancement) from different directions over Europe in which air masses were transported up to the UFS (see Figure S1 in the Supplementary Materials). Trajectories from the 24 h before E6 showed westerly flow patterns in which clean air from the North Atlantic reached the site. Also, trajectories from 24 h after E3 and E7 showed that air masses reached the site via northerly flows from the Arctic Ocean. The case study in [33] is identical to E6 in this study with high formaldehyde, CO, nitrogen oxide, and nitrogen dioxide mixing ratios co-occurring during the event period. Based on the backward trajectory analysis (calculated with HYSPLIT), the influence of polluted PBL was also observed in Leuchner et al. [33], although the trajectories consider neither local wind fields nor complex topography due to the coarse grid resolution of 0.5° of the input model data.
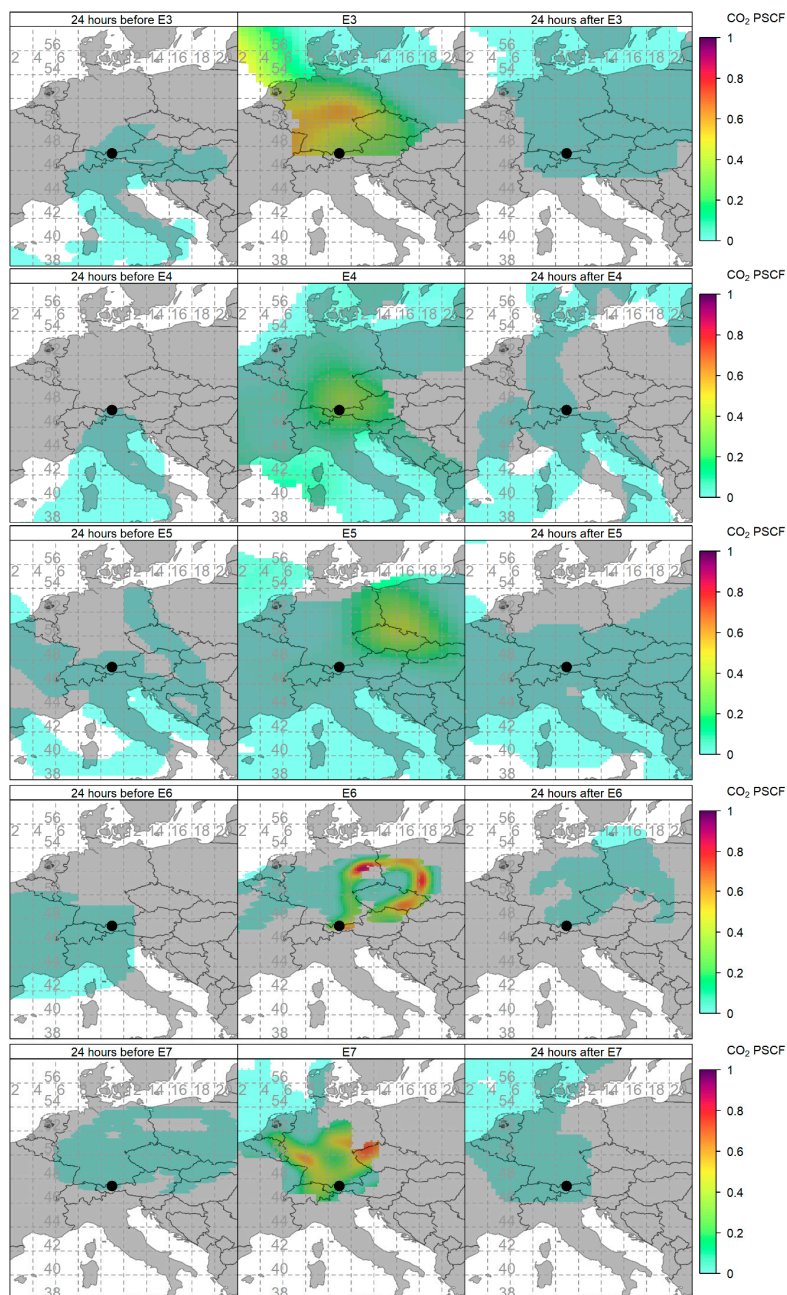
Figure 7. Potential source contribution function (PSCF) plot of CO_2. The color of the maps shows the respective probabilities. For each event (E3 to E7), three plots are shown including 24 h before the event, during the event, and 24 h after the event (left, center, and right, respectively). Blue to purple colors ($0 \leq P_{ij} \leq 1$) identify regions from which elevated CO_2 potentially originated. Black circles show the position of the UFS study site.

In order to detect the area that most influenced the CO_2 mixing ratio, we applied the PSCF to the individual events (except E1 and E2). Figure 7 separately shows the spatial distribution of probable source locations of E3–E7 for 24 h before the events (left panel), during individual events (middle panel), and 24 h after the events (right panel). The coordinates of each map are from 38° to 58° for the latitude with a horizontal resolution of 0.6°. All detected potential sources are located in Germany or at the borders of Germany. This is not unexpected as, according to the European Environment Agency [58], total greenhouse gas emissions per capita in Europe are highest in Germany, where they are mostly associated with energy supply, energy use, and transportation. For more insight, a map of emissions regarding anthropogenic activities is depicted in Figure S2, which was extracted from the EDGAR Ver.432 database relevant to the year 2012. As shown above, E3 and E6 have very similar $\delta^{13}C_s$ and, interestingly for these two events, the PSCF maps depict almost the same source area. Though $\delta^{13}C_s$ in E4, E5, and E7 are comparable, the detected regions are not quite the same. The detected regions of E4, E5, and E7 partially overlap. However, the detected regions of E7 in the west and east of Germany are very similar to the region detected by Ghasemifard et al. [4]. They showed a PSCF map of wintertime over two and a half years (2012–2014), capturing the CO_2 mixing ratio for two specific directions—northwest and northeast of the UFS—where the highest CO_2 mixing ratios were measured and most likely linked to coal mining districts in East Germany and industrial regions in northwestern Europe, including the Netherlands and the German Ruhr area. Sturm et al. [59] simulated the isotope signatures of CO_2 at the JFJ using a backward Lagrangian model. They showed that short-term variabilities may depend on the origin of the air mass. This suggests that there is a close relationship between atmospheric composition and dominant transported air masses.

4. Conclusions

In this paper, seven events of high CO_2 concentration that occurred within five months at the Environmental Research Station Schneefernerhaus (UFS) were investigated. In order to identify and detect pollution events via continuous measurements of CO_2 and its stable carbon isotope, selected criteria were adopted for a moving Keeling plot method based on the UFS specifications. Regarding the characterization of the detected events, a combination of four types of information—namely, the $\delta^{13}C_s$ signature determined by Keeling plots, CO/CO_2 correlation, CH_4/CO_2 correlation, and back trajectory analysis using the HYSPLIT mode—was employed. We were able to explain the observed short-term variation in atmospheric CO_2 mixing ratios by anthropogenic emissions. A summary of the results of the Keeling approaches and emission ratios is provided in Table S1 (Supplementary Materials). The $\delta^{13}C_s$ signatures for the most enriched events (E1 and E2) indicated a significant contribution from coal combustion or wood burning, as well as for the other events that exhibited more depleted contributions from natural gas or gasoline. Based on the ratios between CO, CH_4, and CO_2, it was found that the variation in the atmospheric CO_2 mixing ratios was due to the anthropogenic emissions related to road-transport and traffic, which agrees well with $\delta^{13}C$ source signature values. The CO/CO_2 emission ratio obtained in this research is less than those obtained in previous studies, which is likely due to the technological improvement of vehicles. Though the study period in the cold season minimized the bias of biological activities, it cannot be entirely excluded that biogenic CO_2 sources influenced the emission ratios. Back trajectory analysis established source-receptor relationships and revealed that the observed variations in the atmospheric CO_2 at the UFS were caused by transport of air masses from Central Europe and Germany (E3–E7), as well as by local influences for two events (E1 and E2).

Even high mountain stations can occasionally measure high CO_2 mixing ratios when air masses convey air pollution to these mountain sites. Our analysis revealed that atmospheric trace gas measurements are a vital tool to monitor and quantify air masses that are contaminated by anthropogenic pollution episodes. Measurement of the atmospheric stable isotope ratio $^{13}C/^{12}C$ and CO_2 mixing ratio at high-altitude mountain sites, as well as information about the characteristics of the measurement site, are well suited to the moving Keeling plot for the automatic detection of pollution events. Additional detailed analysis of Foehn episodes, summerly convective upwind systems, and atmospheric circulation

using high-resolution meteorological modeling would provide further insights into the investigations of these kinds of events. Besides the potential to clearly explain the differences from free tropospheric conditions, this pollution analysis is an indispensable tool for source contribution, and thus for detection of pollution emissions in the areas surrounding measuring stations.

Supplementary Materials: The following are available online at http://www.mdpi.com/2073-4433/10/6/330/s1. Figure S1: "96-h HYSPLIT backward trajectories (one-hour interval) of air masses reaching UFS during pollution events (E3–E7). For each event, three plots are shown including 24 h before the event (left panel), during the individual event (middle panel), and 24 h after the event (right panel). The color of the trajectories shows the respective height above ground level (m)." Figure S2: "CO_2 emission field from anthropogenic sources in 20102. Source: EDGAR V432 emission inventory database (see web site: https://edgar.jrc.ec.europa.eu/overview.php?v=432_GHG)." Table S1: "Summary table of results including the source signatures from the classical and moving Keeling plot and emission ratios of CO/CO_2 and CH_4/CO_2. na are missing values due to missing CO and CH_4 data."

References

1. IPCC. *Contribution of Working Groups I, II and III to the Fifth Assessment Report of the Intergovernmental Panel on Climate Change*; IPCC: Geneva, Switzerland, 2014; p. 151.

2. World Meteorological Organization (WMO). *Greenhouse Gas Bulletin: The State of Greenhouse Gases in the Atmosphere Based on Global Observations through 2017*; WMO: Geneva, Switzerland, 2018.

3. Yuan, Y.; Ries, L.; Petermeier, H.; Steinbacher, M.; Gómez-Peláez, A.J.; Leuenberger, M.C.; Schumacher, M.; Trickl, T.; Couret, C.; Meinhardt, F. Adaptive selection of diurnal minimum variation: A statistical strategy to obtain representative atmospheric CO_2 data and its application to European elevated mountain stations. *Atmos. Meas. Tech.* **2018**, *11*, 1501–1514. [CrossRef]

4. Ghasemifard, H.; Yuan, Y.; Luepke, M.; Schunk, C.; Chen, J.; Ries, L.; Leuchner, M.; Menzel, A. Atmospheric CO_2 and $\delta^{13}C$ Measurements from 2012 to 2014 at the Environmental Research Station Schneefernerhaus, Germany: Technical Corrections, Temporal Variations and Trajectory Clustering. *Aerosol Air Qual. Res.* **2019**, *19*, 657–670. [CrossRef]

5. Yuan, Y.; Ries, L.; Petermeier, H.; Trickl, T.; Leuchner, M.; Couret, C.; Sohmer, R.; Meinhardt, F.; Menzel, A. On the diurnal, weekly, seasonal cycles and annual trends in atmospheric CO_2 at Mount Zugspitze, Germany during 1981–2016. *Atmos. Chem. Phys.* **2019**, *19*, 999–1012. [CrossRef]

6. Apadula, F.; Gotti, A.; Pigini, A.; Longhetto, A.; Rocchetti, F.; Cassardo, C.; Ferrarese, S.; Forza, R. Localization of source and sink regions of carbon dioxide through the method of the synoptic air trajectory statistics. *Atmos. Environ.* **2003**, *37*, 3757–3770. [CrossRef]

7. Kaiser, A.; Scheifinger, H.; Spangl, W.; Weiss, A.; Gilge, S.; Fricke, W.; Ries, L.; Cemas, D.; Jesenovec, B. Transport of nitrogen oxides, carbon monoxide and ozone to the alpine global atmosphere watch stations Jungfraujoch (Switzerland), Zugspitze and Hohenpeißenberg (Germany), Sonnblick (Austria) and Mt. Krvavec (Slovenia). *Atmos. Environ.* **2007**, *41*, 9273–9287. [CrossRef]

8. Uglietti, C.; Leuenberger, M.; Brunner, D. European source and sink areas of CO_2 retrieved from Lagrangian transport model interpretation of combined O_2 and CO_2 measurements at the high alpine research station Jungfraujoch. *Atmos. Chem. Phys.* **2011**, *11*, 8017–8036. [CrossRef]

9.	Tuzson, B.; Henne, S.; Brunner, D.; Steinbacher, M.; Mohn, J.; Buchmann, B.; Emmenegger, L. Continuous isotopic composition measurements of tropospheric CO_2 at Jungfraujoch (3580 m a.s.l.), Switzerland: Real-time observation of regional pollution events. *Atmos. Chem. Phys.* **2011**, *11*, 1685–1696. [CrossRef]

10.	Ferrarese, S.; Apadula, F.; Bertiglia, F.; Cassardo, C.; Ferrero, A.; Fialdini, L.; Francone, C.; Heltai, D.; Lanza, A.; Longhetto, A. Inspection of high–concentration CO_2 events at the Plateau Rosa Alpine station. *Atmos. Pollut. Res.* **2015**, *6*, 415–427. [CrossRef]

11.	Levin, I.; Graul, R.; Trivett, N.B. Long-term observations of atmospheric CO_2 and carbon isotopes at continental sites in Germany. *Tellus B* **1995**, *47*, 23–34. [CrossRef]

12.	Farquhar, G.D.; Ehleringer, J.R.; Hubick, K.T. Carbon isotope discrimination and photosynthesis. *Annu. Rev. Plant Phys.* **1989**, *40*, 503–537. [CrossRef]

13.	Mook, W.; Bommerson, J.; Staverman, W. Carbon isotope fractionation between dissolved bicarbonate and gaseous carbon dioxide. *Earth Planet Sci. Lett.* **1974**, *22*, 169–176. [CrossRef]

14.	Ciais, P.; Tans, P.P.; White, J.W.; Trolier, M.; Francey, R.J.; Berry, J.A.; Randall, D.R.; Sellers, P.J.; Collatz, J.G.; Schimel, D.S. Partitioning of ocean and land uptake of CO_2 as inferred by $\delta^{13}C$ measurements from the NOAA Climate Monitoring and Diagnostics Laboratory Global Air Sampling Network. *J. Geophys. Res. Atm.* **1995**, *100*, 5051–5070. [CrossRef]

15.	Pataki, D.E.; Ehleringer, J.R.; Flanagan, L.B.; Yakir, D.; Bowling, D.R.; Still, C.J.; Buchmann, N.; Kaplan, J.O.; Berry, J.A. The application and interpretation of Keeling plots in terrestrial carbon cycle research. *Global Biogeochem. Cycles* **2003**, *17*. [CrossRef]

16.	Pang, J.; Wen, X.; Sun, X. Mixing ratio and carbon isotopic composition investigation of atmospheric CO_2 in Beijing, China. *Sci. Total Environ.* **2016**, *539*, 322–330. [CrossRef] [PubMed]

17.	Pataki, D.E.; Xu, T.; Luo, Y.Q.; Ehleringer, J. Inferring biogenic and anthropogenic carbon dioxide sources across an urban to rural gradient. *Oecologia* **2007**, *152*, 307–322. [CrossRef]

18.	Wada, R.; Pearce, J.K.; Nakayama, T.; Matsumi, Y.; Hiyama, T.; Inoue, G.; Shibata, T. Observation of carbon and oxygen isotopic compositions of CO_2 at an urban site in Nagoya using Mid-IR laser absorption spectroscopy. *Atmos. Environ.* **2011**, *45*, 1168–1174. [CrossRef]

19.	Pfister, G.; Petron, G.; Emmons, L.K.; Gille, J.C.; Edwards, D.P.; Lamarque, J.-F.; Attie, J.-L.; Granier, C.; Novelli, P.C. Evaluation of CO simulations and the analysis of the CO budget for Europe. *J. Geophys. Res. Atm.* **2004**, *109*. [CrossRef]

20.	Levin, I.; Karstens, U. Inferring high-resolution fossil fuel CO_2 records at continental sites from combined $^{14}CO_2$ and CO observations. *Tellus B* **2007**, *59*, 245–250. [CrossRef]

21.	Vardag, S.N.; Gerbig, C.; Janssens-Maenhout, G.; Levin, I. Estimation of continuous anthropogenic CO_2: Model-based evaluation of CO_2, CO, $\delta^{13}C(CO_2)$ and $\Delta^{14}C(CO_2)$ tracer methods. *Atmos. Chem. Phys.* **2015**, *15*, 12705–12729. [CrossRef]

22.	Vogel, F.; Hammer, S.; Steinhof, A.; Kromer, B.; Levin, I. Implication of weekly and diurnal ^{14}C calibration on hourly estimates of CO-based fossil fuel CO_2 ata moderately polluted site in southwestern Germany. *Tellus B* **2010**, *62*, 512–520. [CrossRef]

23.	Popa, M.E.; Vollmer, M.K.; Jordan, A.; Brand, W.A.; Pathirana, S.L.; Rothe, M.; Röckmann, T. Vehicle emissions of greenhouse gases and related tracers from a tunnel study: CO: CO_2, N_2O: CO_2, CH_4: CO_2, O_2: CO_2 ratios, and the stable isotopes ^{13}C and ^{18}O in CO_2 and CO. *Atmos. Chem. Phys.* **2014**, *14*, 2105–2123. [CrossRef]

24.	Schmidt, A.; Rella, C.W.; Göckede, M.; Hanson, C.; Yang, Z.; Law, B.E. Removing traffic emissions from CO_2 time series measured at a tall tower using mobile measurements and transport modeling. *Atmos. Environ.* **2014**, *97*, 94–108. [CrossRef]

25.	Thom, M.; Bösinger, R.; Schmidt, M.; Levin, I. The regional budget of atmospheric methane of a highly populated area. *Chemosphere* **1993**, *26*, 143–160. [CrossRef]

26.	Nam, E.K.; Jensen, T.E.; Wallington, T.J. Methane emissions from vehicles. *Environ. Sci. Technol.* **2004**, *38*, 2005–2010. [CrossRef] [PubMed]

27.	Nakagawa, F.; Tsunogai, U.; Komatsu, D.D.; Yamada, K.; Yoshida, N.; Moriizumi, J.; Nagamine, K.; Iida, T.; Ikebe, Y. Automobile exhaust as a source of ^{13}C-and D-enriched atmospheric methane in urban areas. *Org. Geochem.* **2005**, *36*, 727–738. [CrossRef]

28.	Tohjima, Y.; Kubo, M.; Minejima, C.; Mukai, H.; Tanimoto, H.; Ganshin, A.; Maksyutov, S.; Katsumata, K.; Machida, T.; Kita, K. Temporal changes in the emissions of CH_4 and CO from China estimated from CH_4/CO_2 and CO/CO_2 correlations observed at Hateruma Island. *Atmos. Chem. Phys.* **2014**, *14*, 1663–1677. [CrossRef]

29.   Worthy, D.E.; Chan, E.; Ishizawa, M.; Chan, D.; Poss, C.; Dlugokencky, E.J.; Maksyutov, S.; Levin, I. Decreasing anthropogenic methane emissions in Europe and Siberia inferred from continuous carbon dioxide and methane observations at Alert, Canada. *J. Geophys. Res.* **2009**, *114*. [CrossRef]

30.   Fang, S.-X.; Luan, T.; Zhang, G.; Wu, Y.-L.; Yu, D.-J. The determination of regional CO_2 mole fractions at the Longfengshan WMO/GAW station: A comparison of four data filtering approaches. *Atmos. Environ.* **2015**, *116*, 36–43. [CrossRef]

31.   Henne, S.; Brunner, D.; Folini, D.; Solberg, S.; Klausen, J.; Buchmann, B. Assessment of parameters describing representativeness of air quality in-situ measurement sites. *Atmos. Chem. Phys.* **2010**, *10*, 3561–3581. [CrossRef]

32.   Gantner, L.; Hornsteiner, M.; Egger, J.; Hartjenstein, G. The diurnal circulation of Zugspitzplatt: Observations and modeling. *Meteorol. Z.* **2003**, *12*, 95–102. [CrossRef]

33.   Leuchner, M.; Ghasemifard, H.; Lüpke, M.; Ries, L.; Schunk, C.; Menzel, A. Seasonal and diurnal variation of formaldehyde and its meteorological drivers at the GAW site Zugspitze. *Aerosol Air Qual. Res.* **2016**, *16*, 801–815. [CrossRef]

34.   Zellweger, C.; Forrer, J.; Hofer, P.; Nyeki, S.; Schwarzenbach, B.; Weingartner, E.; Ammann, M.; Baltensperger, U. Partitioning of reactive nitrogen (NO_y) and dependence on meteorological conditions in the lower free troposphere. *Atmos. Chem. Phys.* **2003**, *3*, 779–796. [CrossRef]

35.   GAWSIS. Station Information System. Available online: https://gawsis.meteoswiss.ch/GAWSIS/ (accessed on 17 June 2019).

36.   Nara, H.; Tanimoto, H.; Tohjima, Y.; Mukai, H.; Nojiri, Y.; Katsumata, K.; Rella, C.W. Effect of air composition (N_2, O_2, Ar, and H_2O) on CO_2 and CH_4 measurement by wavelength-scanned cavity ring-down spectroscopy: Calibration and measurement strategy. *Atmos. Meas. Tech.* **2012**, *5*, 2689–2701. [CrossRef]

37.   Pang, J.; Wen, X.; Sun, X.; Huang, K. Intercomparison of two cavity ring-down spectroscopy analyzers for atmospheric $^{13}CO_2/^{12}CO_2$ measurement. *Atmos. Meas. Tech.* **2016**, *9*, 3879–3891. [CrossRef]

38.   Rella, C.W.; Chen, H.; Andrews, A.E.; Filges, A.; Gerbig, C.; Hatakka, J.; Karion, A.; Miles, N.L.; Richardson, S.J.; Steinbacher, M.; et al. High accuracy measurements of dry mole fractions of carbon dioxide and methane in humid air. *Atmos. Meas. Tech.* **2013**, *6*, 837–860. [CrossRef]

39.   Vogel, F.R.; Huang, L.; Ernst, D.; Giroux, L.; Racki, S.; Worthy, D.E. Evaluation of a cavity ring-down spectrometer for in situ observations of $^{13}CO_2$. *Atmos. Meas. Tech.* **2013**, *6*, 301–308. [CrossRef]

40.   Wen, X.-F.; Meng, Y.; Zhang, X.-Y.; Sun, X.-M.; Lee, X. Evaluating calibration strategies for isotope ratio infrared spectroscopy for atmospheric $^{13}CO_2/^{12}CO_2$ measurement. *Atmos. Meas. Tech.* **2013**, *6*, 1491–1501. [CrossRef]

41.   Team, R. *RStudio: Integrated Development for R*; R Studio Inc.: Boston, MA, USA, 2016; Available online: http://www.rstudio.com/ (accessed on 7 March 2019).

42.   Carslaw, D.C.; Ropkins, K. Openair—An R package for air quality data analysis. *Environ. Modell. Softw.* **2012**, *27*, 52–61. [CrossRef]

43.   Wickham, H. *GGPLOT2: Elegant Graphics for Data Analysis*; Springer: New York, NY, USA, 2010.

44.   Keeling, C.D. The concentration and isotopic abundances of atmospheric carbon dioxide in rural areas. *Geochim. Cosmochim. Acta* **1958**, *13*, 322–334. [CrossRef]

45.   Keeling, C.D. The concentration and isotopic abundances of carbon dioxide in rural and marine air. *Geochim. Cosmochim. Acta* **1961**, *24*, 277–298. [CrossRef]

46.   Vardag, S.N.; Hammer, S.; Levin, I. Evaluation of 4 years of continuous $^{13}C(CO_2)$ data using a moving Keeling plot method. *Biogeosciences* **2016**, *13*, 4237–4251. [CrossRef]

47.   Miller, J.B.; Tans, P.P. Calculating isotopic fractionation from atmospheric measurements at various scales. *Tellus B* **2003**, *55*, 207–214. [CrossRef]

48.   Krystek, M.; Anton, M. A weighted total least-squares algorithm for fitting a straight line. *Meas. Sci. Tech.* **2007**, *18*, 3438. [CrossRef]

49.   Ammoura, L.; Xueref-Remy, I.; Gros, V.; Baudic, A.; Bonsang, B.; Petit, J.-E.; Perrussel, O.; Bonnaire, N.; Sciare, J.; Chevallier, F. Atmospheric measurements of ratios between CO_2 and co-emitted species from traffic: A tunnel study in the Paris megacity. *Atmos. Chem. Phys.* **2014**, *14*, 12871–12882. [CrossRef]

50.   Xueref-Remy, I.; Messager, C.; Filippi, D.; Pastel, M.; Nedelec, P.; Ramonet, M.; Paris, J.D.; Ciais, P. Variability and budget of CO_2 in Europe: Analysis of the CAATER airborne campaigns—Part 1: Observed variability. *Atmos. Chem. Phys.* **2011**, *11*, 5655–5672. [CrossRef]

51. Necki, J.; Schmidt, M.; Rozanski, K.; Zimnoch, M.; Korus, A.; Lasa, J.; Graul, R.; Levin, I. Six-year record of atmospheric carbon dioxide and methane at a high-altitude mountain site in Poland. *Tellus B* **2003**, *55*, 94–104. [CrossRef]

52. Schmidt, M.; Graul, R.; Sartorius, H.; Levin, I. Carbon dioxide and methane in continental Europe: A climatology, and ^{222}Radon-based emission estimates. *Tellus B* **1996**, *48*, 457–473. [CrossRef]

53. Draxler, R.R.; Hess, G.D. An overview of the HYSPLIT_4 modelling system for trajectories, dispersion and deposition. *Aust. Met. Mag.* **1998**, *47*, 295–308.

54. Stohl, A. Trajectory statistics—A new method to establish source-receptor relationships of air pollutants and its application to the transport of particulate sulfate in Europe. *Atmos. Environ.* **1996**, *30*, 579–587. [CrossRef]

55. Ashbaugh, L.L.; Malm, W.C.; Sadeh, W.Z. A residence time probability analysis of sulfur concentrations at Grand Canyon National Park. *Atmos. Environ.* **1985**, *19*, 1263–1270. [CrossRef]

56. Seinfeld, J.H.; Pandis, S.N. *Atmospheric Chemistry and Physics: From Air Pollution to Climate Change*, 3rd ed.; John Wiley & Sons: Hoboken, NJ, USA, 2016.

57. Vollmer, M.K.; Juergens, N.; Steinbacher, M.; Reimann, S.; Weilenmann, M.; Buchmann, B. Road vehicle emissions of molecular hydrogen (H_2) from a tunnel study. *Atmos. Environ.* **2007**, *41*, 8355–8369. [CrossRef]

58. European Environment Agency. *Greenhouse Gas Emission Trends and Projections in Europe 2012*; European Environment Agency: Copenhagen, Denmark, 2012.

59. Sturm, P.; Tuzson, B.; Henne, S.; Emmenegger, L. Tracking isotope signatire of CO_2 at the high altitude site Jungfraujoch with laser spectroscopy: Analytical improvements and respective results. *Atmos. Meas. Tech.* **2013**, *6*, 1659–1671. [CrossRef]